Politechnika Wrocławska

FIELD of SCIENCE: Engineering and Technology

DISCIPLINE of SCIENCE: Materials Engineering

DOCTORAL DISSERTATION

Photocatalytic TiO_2 Coatings Deposited by Low-Pressure Cold Gas Spraying Using Amorphous Powders Obtained by Sol-Gel Method

Mrs. Wioletta Seremak, MSc., Eng.

Supervisor/Supervisors:

PhD DSc. Marek Jasiorski, Assoc. Prof. of WUST

Assistant supervisor:

PhD DSc Eng. Marcin Winnicki, Assoc. Prof. of WUST

Keywords: TiO_2, low pressure cold spray, advanced oxidation processes, photocatalysis

WROCŁAW 2025

Acknowledgements

First and foremost, I extend my deepest gratitude to my supervisors prof. Marek Jasiorski, prof. Marcin Winnicki, and prof. Agnieszka Baszczuk (who felt like the 3rd supervisor) for their support, patience - which extended far beyond the scope of their roles - and the invaluable opportunity to discuss ideas and results throughout this journey. Their guidance has been instrumental in helping me acquire new skills and knowledge, without which the completion of this dissertation would not have been possible.

Endless gratitude goes to my fiancé, Dawid, for his boundless love, support, food and entertainment-both when I needed it most and when I least expected it. A special thank you for always being there きのこーちゃん.

I am profoundly grateful to my family for their encouragement and for reminding me to balance the demands of research with cherished moments spent with loved ones.

I owe special thanks to my fiancé's father, Don Marco, for his enduring encouragement and empathy throughout this endeavour.

To my labmates—Dr Borak, Bartek, Ania, Jola, Ania, Natalia, Mr Kowalik, and the rest of the sol-gel team—thank you for sharing in the frustrations of failed syntheses, the camaraderie of preparing for (and teaching) mechanics exams, for the unforgetful PhD integrations and for the countless stories, assistance, and kindness that made this journey memorable.

To prof. Maciej Matyka from the University of Wrocław for the encouragement, optimism and discussions.

And last but not least, I would like to express my gratitude to the Scientists with whom I collaborated or who gave me access to their equipment and shared with their knowledge: the researchers from the Wrocław University of Science and Technology, from the K58 and K60 Department and researchers from the Wroclaw University of Economics and Business, Department of Chemical Technology.

Abstract

Drinkable water scarcity poses a growing global threat and is gaining even more attention due to constant industrialisation and population growth. In response, advanced water treatment methods have emerged, with photocatalysis attracting significant interest due to its capability for the complete mineralisation of persistent organic pollutants using light energy, which is unattainable with conventional methods.

Titanium dioxide (TiO_2) is the most often chosen material for photocatalytic applications due to its low cost, wide availability, chemical stability, and non-toxicity. Yet, despite four decades of research, photocatalytic systems remain underutilised in industrial applications. This gap stems from a disproportionate focus on photocatalytic materials modification while neglecting their applicational aspects, among which the form of the photocatalyst largely determines the feasibility of its operation on an industrial scale. Concerning the latter, immobilised photocatalysts are more often chosen, sacrificing their specific surface area and reducing efficiency due to thermal degradation. The low-pressure cold spray (LPCS) process, a kinetic-driven deposition technique, addresses this by retaining material properties through low-temperature processing. However, depositing oxide powders like TiO_2 via LPCS is challenging due to their inherent brittleness. A promising solution involves using agglomerated TiO_2 particles, which deform via agglomerate flattening and break-up during deposition. Another underexplored aspect is photocatalyst longevity. Scarce data on aged photocatalyst behaviour hinders predictions of property degradation over operational cycles, despite the economic and environmental benefits of reusability.

In this thesis, the combination of sol–gel synthesis with the LPCS technique for the fabrication of photocatalytic TiO_2 coatings is researched. The sol–gel method produces amorphous, self-agglomerated TiO_2 powder, enabling LPCS deposition. This synergistic approach ensures homogeneity, scalability, and functional retention. To enable the deposition of the oxide powder via LPCS, the sol-gel-derived TiO_2 powder is amorphous and self-agglomerated. The photocatalytic performance of the resulting coatings is evaluated via

methylene blue (MB) model pollutant degradation under UV light. Additionally, to study the ageing of a photocatalyst, two experiments are carried out: (1) continuous long-term ageing in a humid chamber to simulate structural degradation and (2) multi-cycle decomposition tests to evaluate photocatalytic stability. Furthermore, the powder synthesis is modified to determine the influence of powder agglomeration on the LPCS deposition process and the properties of the resulting coating.

Results demonstrate that LPCS-immobilised TiO_2 coating material partially crystallises into the anatase phase and degrades methylene blue effectively under UV light. Long-term ageing negatively affects the adsorption properties of the photocatalyst, decreasing its effectiveness. The multi-cycle decomposition test shows that a more crystalline photocatalyst yields more repetitive rates of MB decomposition reactions. Additionally, the regeneration of the photocatalyst between the consecutive tests enables maintaining its initial effectiveness. What is more, the TiO_2 coatings have low cohesion, and their adhesion mechanism is determined by the coatings' degree of crystallinity. Two types of adhesion mechanisms are proposed: predominantly amorphous coatings rely on chemical bonding, while coatings with a higher number of crystalline grains adhere via mechanical bonding. Ageing tests show that chemically bonded coatings strengthen over time due to the increase in the number of bonds established, whereas mechanically bonded interfaces weaken due to reduced surface contact. Despite the ageing-weakening, the mechanically bonded coatings have superior adhesion. Lastly, the synthesis of the TiO_2 is altered by increasing the pH and varying the solvent (between isopropanol, methanol and acetone), which affects the self-agglomeration of the powders and directly influences their deposition efficiency. As a result, coating adhesion is affected, while higher pH increases dye adsorption, causing the photocatalyst fouling and decomposition rate to decrease.

The results show the possibility of photocatalyst production via non-standard methods, like sol-gel and LPCS, and discuss photocatalyst longevity and adhesion mechanisms while identifying key challenges: enhancing coating cohesion and extending light absorption into the visible spectrum.

Streszczenie

Niedobór wody pitnej stanowi globalny problem, potęgowany poprzez postępującą industrializację i wzrost liczby ludności na świecie. W odpowiedzi na globalny kryzys wodny rozwijane są nowoczesne metody uzdatniania wody. Na szczególną uwagę zasługują procesy fotokatalityczne, które w porównaniu do konwencjonalnych metod pozwalają na całkowitą mineralizację trwałych zanieczyszczeń organicznych. Najczęściej wybieranym fotokatalizatorem jest dwutlenek tytanu (TiO_2) ze względu na niski koszt, powszechną dostępność, nietoksyczność oraz trwałość chemiczną. Badania nad TiO_2 z ostatnich czterdziestu lat skupiają się głównie na zapewnieniu funkcjonalności poprzez modyfikację materiału, zaniedbując inne cechy użytkowe, przez co rzadko dotyczą przemysłowego zastosowania TiO_2. W kontekście fotokatalizatorów, charakterystyka użytkowa obejmuje przede wszystkim formę fotokatalizatora. Unieruchomienie materiału aktywnego fotokatalitycznie upraszcza jego użytkowanie jednocześnie, zmniejszając jego powierzchnię czynną, co prowadzi do obniżonej wydajności, a sam proces deponowania - nierzadko degradacji termicznej materiału. Pośród metod o niższym reżimie temperaturowym, zapewniających zachowanie pierwotnych właściwości fotokatalizatora, można wyróżnić niskociśnieniowe natryskiwanie na zimno (LPCS). Proces ten wykorzystuje energię kinetyczną do osadzenia materiałów proszkowych na podłożu. Niestety, deponowanie nieodkształcalnych, kruchych proszków tlenkowych, jak TiO_2, obniża efektywność osadzania. Lepszą wydajność procesu uzyskuje się poprzez użycie zaglomerowanego proszku TiO_2, który podczas natrysku ulega rozpadowi na mniejsze cząstki w efekcie uderzenia o powierzchnię. Innym często zaniedbywanym zagadnieniem dotyczącym fotokatalizatorów jest ich trwałość. Brak danych o zachowaniu się materiału w trakcie eksploatacji utrudnia prognozowanie zmian właściwości i ogranicza możliwość wielokrotnego użycia, co ma kluczowe znaczenie ekonomiczne i środowiskowe.

Niniejsza praca doktoraska bada połączenie procesu syntezy zol–żel z techniką LPCS w celu wytworzenia fotokatalitycznych powłok TiO_2. Metoda zol-żel jest wykorzystana do wytworzenia amorficznego i zaglomerowanego materiału proszkowego TiO_2, z kolei proces

LPCS został użyty do osadzenia materiału fotokatalitycznego. To połączenie metod (technik) pozwala uzyskać jednorodne, skalowalne powłoki TiO_2 zachowując pierwotne właściwości proszków. Właściwości fotokatalityczne oceniano za pomocą rozkładu modelowego zanieczyszczenia – barwnika błękitu metylenowego w obecności promieniowania UV. Co więcej, aby zbadać wpływ warunków eksploatacyjnych na fotokatalizator, zastosowano dwa typy eksperymentów: (1) długotrwałe starzenie struktury w komorze wilgotnościowej oraz (2) wielocyklowy test rozkładu, oceniający stabilność efektywności podczas kolejnych użyć. Ponadto, modyfikowano syntezę proszków przez zmianę pH i rozpuszczalnika (izopropanol, metanol, aceton), co umożliwiło kontrolę stopnia aglomeracji i jej wpływu na wydajność procesu LPCS.

Otrzymane powłoki TiO_2 skutecznie degradowały MB w zakresie światła UV. Proces deponowania przyczynił się do częściowego wykrystalizowania amorficznej formy do fazy anatazu. Długoterminowe starzenie obniżyło adsorpcję fotokatalizatora i w efekcie szybkość rozkładu barwnika, natomiast test wielocyklowy wykazał, że powłoki o wyższej krystaliczności cechują się większą powtarzalnością szybkości reakcji rozkładu, a regeneracja fotokatalizatora pomiędzy cyklami pozwala utrzymać jego początkową aktywność. Co więcej, wszystkie powłoki charakteryzują się niską kohezją, z kolei mechanizm ich adhezji zależy od stopnia krystaliczności materiału. Zaproponowano dwa typy adhezji: chemiczne (w powłokach amorficznych) i mechaniczne (w krystalicznych). Starzenie powłok umocniło adhezję wynikającą z wiązań chemicznych poprzez zwiększenie ich liczby, jednocześnie osłabiło mechaniczne zakotwiczone powłoki z powodu zmniejszenia powierzchni styku. Pomimo tego, po starzeniu krystaliczne powłoki zachowywały dwukrotnie wyższą adhezję od amorficznych. Modyfikacje syntezy zol-żel TiO_2 polegającą na podwyższeniu pH i zamianie rozpuszczalnika (pomiędzy izopropanolem, metanolem i acetonem) wpływa na aglomerację proszków i na ich efektywność osadzania. W wyniku czego, adhezja powłok również uległa zmianie, natomiast różnice w morfologii proszków, właściwościach powłok oraz ich stopnia krystaliczności ma wpływ na efektywność fotokatalizatora.

Przedstawione wyniki potwierdzają, że odpowiedni dobór parametrów procesów zol–żel i LPCS pozwala uzyskanie pożądanych cech użytkowych TiO_2, zachowując ich funkcjonalność. Praca wnosi istotny wkład w rozwój skalowalnych metod wytwarzania fotokatalizatorów, opisuje mechanizmy adhezji i trwałość materiału pod wpływem starzenia oraz wskazuje kierunki dalszych badań: poprawę kohezji powłok i rozszerzenie ich aktywności na zakres widzialny.

List of publications and presentations

1. Seremak W., Baszczuk A., Jasiorski M., Gibas A., Winnicki M., Photocatalytic Activity Enhancement of Low-pressure Cold-Sprayed TiO_2 Coatings Induced by Long-term Water Vapor Exposure; Journal of Thermal Spray Technology, 2021, https://doi.org/10.1007/s11666-021-01244-5
2. Kielan-Grabowska Z., Bącela J., Zięty A., Seremak W., Gawlik-Maj M., Kawala B., Borak B., Detyna J., Sarul M., Improvement of Properties of Stainless Steel Orthodontic Archwire Using TiO2:Ag Coating, Symmetry, 2021, https://doi.org/10.3390/sym13091734
3. Seremak W., Jasiorski M., Baszczuk A., Winnicki M., Preliminary Study on Low-Pressure Cold Spray Process Parameters: Effect on Mechanical and Photocatalytic Properties of TiO_2 Coatings, Journal of Thermal Spray Technology, 2023, https://doi.org/10.1007/s11666-023-01615-0
4. Seremak W., Jasiorski M., Baszczuk A., Winnicki M., Durability Assessment of Low-pressure Cold-Sprayed TiO_2 Photocatalytic Coatings: photocatalytic and Mechanical Stability, Surface & Coatings Technology, 2025, https://doi.org/10.1016/j.surfcoat.2025.131740

Oral presentations and posters at international conferences

1. Approach to design photocatalytic TiO_2 coatings – effects of low-pressure cold spray parameters on coatings characteristics (poster), Les Rencontres Internationales de la Projection Thermique, 10RIPT 2022, 1-3.06.2022, Jülich, Germany (poster).
2. Approach to design photocatalytic TiO_2 coatings – effects of low-pressure cold spray parameters on coatings characteristics, 6th International thermal spraying and hardfacing conference - ITSHC, 22 - 23.09.2022, Wroclaw, Poland (oral).
3. TiO_2 Powder Modification for Low-Pressure Cold Spraying of the Photocatalytic Coatings: solvent influence in sol-gel process, Les Rencontres Internationales de la Projection Thermique: 11 RIPT Conference, 5- 7.06.2024, Jülich, Germany (poster).

4. Investigating Long-Term Performance of Low-Pressure Cold-Sprayed TiO_2 Photocatalytic Coatings, Les Rencontres Internationales de la Projection Thermique: 11 RIPT Conference, 5- 7.06.2024, Jülich, Germany (oral).
5. Influence of the organic solvent in sol-gel synthesis of TiO_2 powder on the Low-Pressure Cold Spray photocatalytic coatings properties, the 22nd international Sol-Gel conference, 1-6.09.2024, Berlin, Germany (oral).

Table of contents

List of abbreviations and symbols

Abbreviations	Description
μ	friction coefficient
λ_C	cut-off filter value
Φ	diameter
ACE	acetone
AD	aerosol deposition
A_{pa}	integrated area of the amorphous component
AOPs	advanced oxidation processes
APCVD	atmospheric pressure chemical vapour deposition
BSE	backscattered electrons
C	concentration of the contaminant molecule in solution at any given time during degradation (mg/L)
C_0	initial concentration
C_x	remaining concentration
CB	conduction band
C_{pa}	integrated area of the crystalline component
C_M	substance concentration
CVD	chemical vapour deposition
CS	cold-spray
D	degradation efficiency
D-gun spraying	Detonation gun spraying

DOC	degree of crystallinity
e	electron
E_c	lowest energy level in the conduction band
E_g	band gap value
E_v	highest energy level in the valence band
$F(R)$	absorption coefficient
FP	feedstock powder
F_N	normal force
h	hole
$h\nu$	photon energy
HPCS	high-pressure cold spraying
HVOF spraying	high-velocity oxy-fuel spraying
IPOH	isopropanol
K	equilibrium constant for the adsorption of the substrate onto the catalyst
k_r	limiting rate constant of reaction at maximum coverage under the given experimental conditions
L-H	Langmuir-Hinshelwood
L_{c1}	cohesive failure/strength
L_{c2}	adhesive failure/strength
LPCS	Low-pressure cold spraying
Lt	tracing length

MB	methylene blue
MOH	methanol
n	the reaction order, typically in the range of $0 \leq n \leq 2$
P25	P25 Degussa
P_d	penetration depth
PECVD	plasma-enhanced chemical vapour deposition
PSD	particle size distribution
PVD	physical vapour deposition
pzc	the point of zero charge
$Q3(x_0)$	cumulative volumetric distribution
$q3(x_m)$	fractional volumetric distribution
r	the rate of the reaction
R	reflectance
Ra	roughness average
Rz	average maximum height of the profile
RTIC	room temperature impact consolidation
s	standard deviation
SE	secondary electrons
SEM	scanning electron microscopy

SSA	specific surface area
Span	particle size distribution width
TiO_2	titanium dioxide
TiO_2-0	initial titanium dioxide powder
TS	thermal spray
TTIP	titanium (IV) isopropoxide
UV	ultraviolet
VB	valence band
x	mean value
x_n	volume median diameters
XRD	X-ray diffraction

1 Motivation

Water scarcity is becoming a significant issue for many of the world's largest populations. In 2016, around a billion people in urban areas experienced water scarcity. By 2050, this number is expected to increase to two billion people struggling with their health and well-being due to limited access to clean water [1]. At the same time, society's expectations for industrialisation and urbanisation are constantly increasing, which contributes to further environmental pollution as industrial activities are among the main sources of water environment contamination [2]. Pollutant discharge into waterways, agricultural and urban runoff, wastewater, and lastly, oil and chemical spills (mainly caused by accidents during transportation and storage of the substances) are the main causes of aquatic environment contamination [3]. Given the circumstances, it is crucial to base water remediation technologies on processes that are efficient, sustainable, and environmentally friendly [4].

Numerous methods were studied by researchers as a potential solution to the water pollution problem. However, despite attempts, the complete treatment of polluted water in a single operation is still unattainable for conventional remediation methods [5]. There is also the problem of pollutant complexity and diversity which often limits the possible treatment methods to those targeting specific pollutant species, limiting the applicability of the system. As a result an efficient technique, characterized by low energy consumption, as well as the ability to decompose a wide variety of different contaminants without secondary waste, is yet to be designed [6]. One of the potential methods is photocatalysis, which is a chemical treatment method that derives from advanced oxidation processes (AOPs). The photocatalytic process utilizes semiconductors, also called photocatalysts, that can catalyse chemical reactions by harnessing light energy, allowing for quick decomposition rates with low energy consumption [7]. The working principle of the photocatalytic process is based on the generation of free radicals. The process starts with the activation of the semiconductor with light irradiation. Due to this interaction, the charge carriers are generated in the volume of the semiconductor and migrate to the surface of the photocatalyst. Their presence is followed by the interaction with the adjacent molecules and the production of free radicals.

The appearance of free radicals initiates chain reactions, which eventually result in the decomposition of pollutants into CO_2 and H_2O [8]. The free-radicals-based remediation process enables the decomposition of highly stable and non-biodegradable organic compounds [9], microorganisms, and bacteria, as well as the reduction of metal ions [8]. While the chemistry of photocatalysis is well established, its practical implementation is influenced not only by the properties of the photocatalyst material itself but also by the physical form in which it is applied. From an applicational point of view, the material's structural configuration plays a pivotal role in determining the feasibility, efficiency, and eventual scalability or commercialisation of photocatalytic systems. The interplay between these material characteristics and real-world operational demands is therefore central to bridging the gap between laboratory success and industrial viability [10,11].

Among the various materials investigated for photocatalytic applications, titanium dioxide (TiO_2) stands out as a benchmark due to its high chemical stability, nontoxicity, availability, and cost-effectiveness [12]. Additionally, TiO_2 can adopt four forms: (1) amorphous, (2) brookite, (3) anatase, and (4) rutile. The amorphous phase is superior in terms of the surface area [13]. Brookite is the least utilised due to its phase metastability [14]. Anatase is known for its high reactivity, while the rutile is the most stable phase of all mentioned [15]. Both, the phase and physical form of the TiO_2 can be controlled through the proper production method of the material, emphasising the relevance of the way the material is obtained [15]. Over the past few years, TiO_2 popularity increased, among others, due to the appearance of a TiO_2-based, commercially available material – P25 Degussa. The commercially available product is sold in submicron powdered form, comprising two crystalline phases: anatase and rutile, which increases its photocatalytic activity [16]. Its standardized and well-characterized properties have provided a reference point for researchers in the field of photocatalytic materials [11].

Despite this reliable reference material and decades of research, the translation of photocatalysis into commercially viable water-treatment systems remains limited [11]. The primary obstacle to the development of these systems is the highly crystalline form of

the photocatalysts. The high crystallinity of TiO_2 simultaneously ensures better photocatalytic activity than the amorphous structure [17] and limits its commercial application only to slurry reactors. Reconciling maximum efficiency with its high surface area is impossible in other reactor types, making the slurry reactors the best possible option [8]. However, due to the supplementary steps and long process duration required to recover the photocatalyst, those reactors are avoided [10]. A good alternative to slurry reactors are fixed-bed reactors, the use of which is less intricate and time-consuming [18]. Yet, when the powder is immobilized onto surfaces, its active surface area is restricted, diminishing the effectiveness of the photocatalyst [19]. Moreover, the crystalline nature of the photocatalyst restricts processing to expensive, high-temperature techniques. The photocatalysts are oxide materials which makes them tough, brittle, and unlike to adhere to the substrate material unless harsh conditions, such as high-temperature, are employed, which simultaneously can trigger unintended material transformation, suppressing the photocatalyst performance even further [20,21]. These considerations underscore the critical importance of selecting a deposition method that both immobilises the photocatalyst on the substrate and enables the active surface area to be tailored while preserving the catalyst's inherent properties.

Overcoming this barrier proved to be possible using the kinetic-based method like cold-spray (CS). Unlike typical deposition processes, CS does not rely on the temperature nor require the melting of the feedstock powder (FP). Instead, it employs solid-state deformation of the FP and/or base surface to build up the coating material [22]. The first successful attempts to CS the TiO_2 coatings were achieved thanks to the agglomeration of the FP, which enabled its deformation and led to coating buildup [23]. In the published literature, the agglomeration of the TiO_2 powder is the result of either chemical modification of commercially available powder or a tailored synthesis process [24]. Among the latter, sol-gel synthesis of the TiO_2 provides the opportunity to acquire agglomerated powder, control the form of the TiO_2, and incorporate additional elements to modify the properties of the photocatalyst [25]. What is more, the sol-gel-derived, amorphous TiO_2 powder incorporated in the cold spray process goes through partial crystallisation. The cold-sprayed material partially transitions into anatase, however,

the amount of heat used in the process is insufficient to transform it into the rutile phase. The amorphous agglomerated powder created a few ten-micrometres thick, two-phase coatings, making it a perfect alternative to typical heat-relying processes [26].

However, the lifetime of the photocatalyst does not end with its successful fabrication and single use, but with its long-term operation and eventual recycling. Despite the significance, the long-term ageing behaviour of immobilised photocatalysts remains underrepresented in the literature. Understanding how performance, surface chemistry and adhesion evolve over repeated use and exposure to real-world conditions is essential for predicting operational lifetime and maintenance cycles, yet systematic studies of photocatalyst degradation under realistic environmental stressors are scarce, leaving the subject unaddressed.

Despite the success in cold spraying thick TiO_2 coatings, many of their properties are yet to be evaluated. The above-mentioned issues are yet to be addressed. This thesis aims to study the properties of the photocatalytic CS coatings. In particular:

- to investigate the relationship between the LPCS process parameters and the resulting TiO_2 coatings' photocatalytic and mechanical properties;
- to identify the physicochemical properties of TiO_2 coatings that enhance the efficiency of organic pollutant degradation;
- to evaluate the possibility of the acquired TiO_2 coatings' potential reuse, through long-term exposure to the working conditions and examination of the changes in the photocatalytic and mechanical properties;
- to determine the influence of the powder agglomeration properties on the LPCS process through the sol-gel synthesis modification.

2 Introduction

2.1 Overview of the photocatalytic process and TiO_2 photocatalysts

The increasing industrialisation and population growth render clean water scarcity a critical threat in the coming years. To reduce water demand new, more efficient wastewater treatment methods need to be developed [1,2]. Consequently, researchers have turned to advanced oxidation processes (AOPs), which offer greater effectiveness than conventional water reclamation techniques as they allow complete pollution degradation. Among AOPs, the photocatalytic process has gained the most attention – not only for water remediation but also for broader environmental applications (as it is effective in both aqueous and gaseous media) [6,7]. Photocatalysis, being a light-activated process, enables the design of solar-driven water treatment systems and facilitates the mineralisation, or reduction of large quantities of pollutants, including organic molecules, toxic substances, harmful gases, and heavy metal ions [7].

The photocatalytic effect of the materials can be explained based on the energy band theory of solids [27]. Unlike, conductors in which the valence band (VB) overlaps with the conduction band (CB), in semiconductors there is a small gap between the valence and conduction bands, named the forbidden band. The forbidden band contains no electron states and its width defines the minimum energy required to excite the electrons into the CB. Typically, a semiconductor comprises a low-energy VB and a high-energy CB, whereas the energy difference between the VB and CB is called the band gap (E_g). The band gap energy can be characterised by three parameters: the highest energy level in the valence band (E_v), the lowest energy level in the conduction band (E_c), and the band gap value itself ($E_g=E_v-E_c$), the relative position of the values are presented in Fig. 2.1.1. These three parameters – (i) E_g, (ii) E_v, and (iii) E_c), along with the semiconductor's charge dynamics, largely dictate its photocatalytic process [46]. In practice, light irradiation provides the energy for excitation of a semiconductor, which transfers the electrons from VB to CB, hence the term "photocatalysts" for these semiconducting materials.

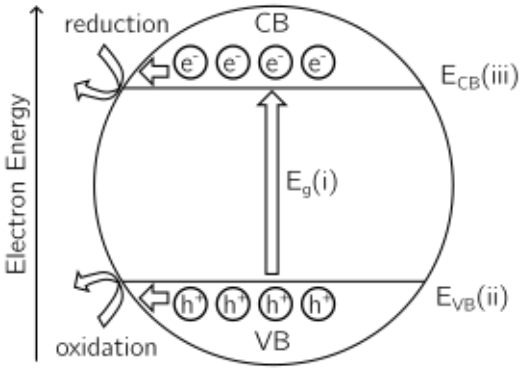

Fig. 2.1.1 the key quantities that govern the photocatalytic process of a semiconductor photocatalyst. Adapted from [28].

The photocatalytic reaction mechanism involves several key phenomena (Fig. 2.1.2) [29]:

1. Irradiation with light of energy equal to, or greater than the band gap energy of a semiconductor excites electrons, transferring them from the valence band (VB) to the conduction band (CB) and leaving behind holes in the valence band;
2. The generated charge carriers (electrons and holes) may recombine, releasing heat, or migrate to the photocatalyst surface;
3. At the surface, these charge carriers can either recombine, or interact with adsorbed organic substances and initiate chemical reactions; the nature of the reaction depends on the charge carrier type: holes (h^+) typically drive oxidation reactions either directly, through interaction with pollutant molecules, or indirectly via the formation of surface-bound hydroxyl radicals. Conversely, electrons (e^-) are generally involved in reduction reactions, often through oxygen reduction processes that generate free radicals;
4. Subsequently, these free radicals interact with pollutant molecules, leading to their decomposition and complete mineralisation.

Generally, the photocatalytic process can be categorised into two types depending on the catalyst's phase. When the catalyst is dissolved in the same phase as the reactants, homogeneous photocatalysis occurs; whereas, when reactions take place at an interface – such as a solid-liquid or solid-gas interface – heterogeneous photocatalysis takes place. Heterogeneous photocatalysis is generally preferred because it is technically easier to separate the semiconductor from the treated media, enabling its reuse [30].

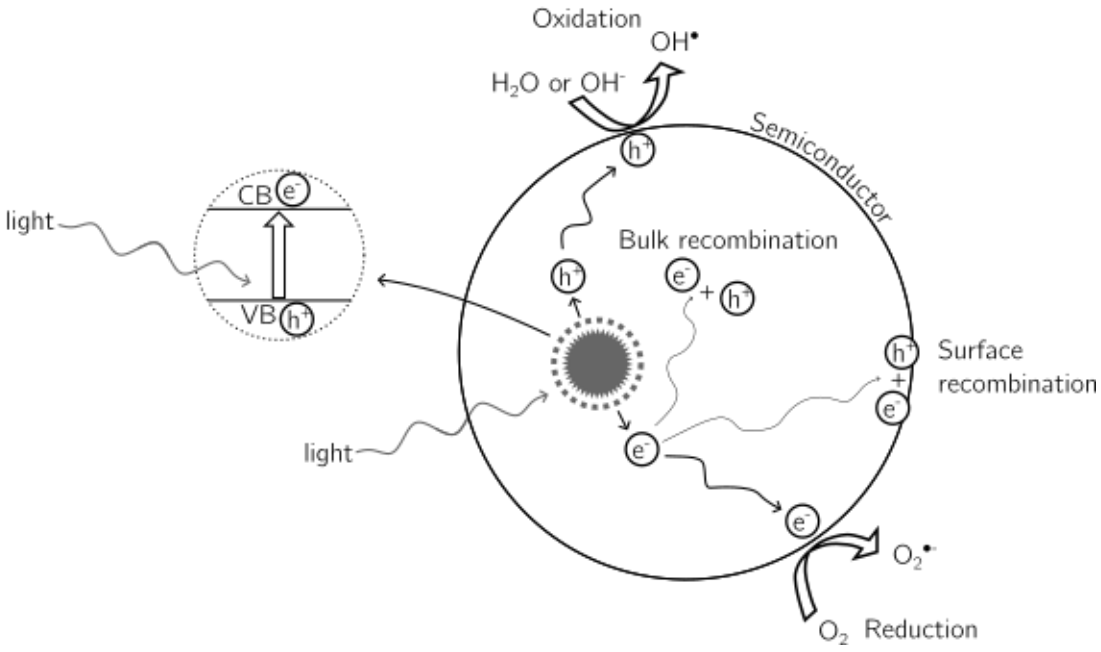

Fig. 2.1.2 Mechanism of the photocatalytic activity on the surface of the semiconductor under the irradiation of light. Adapted from [29].•

The efficiency of heterogeneous photocatalytic degradation is influenced by a range of factors, which can be divided into two groups: process-specific and photocatalyst-specific. The first group comprises external parameters that are not inherent to the photocatalyst, but the process itself, such as the light source, pH, temperature, pollutant properties and concentration, photocatalyst loading, and mass transfer/mixing conditions. These factors underscore the importance of optimising the overall photocatalytic process design [31] and are further discussed in Section 2.5.1 on standardised testing for ceramic semiconductors. The second group consists of parameters, such as band gap energy, crystallinity, phase composition, surface area (and porosity), and morphology, highlighting the need for careful photocatalyst selection and the potential for property modification [32].

2.1.1 Key properties of photocatalysts

The characteristics of photocatalysts include chemical and physical features. The chemical composition of a photocatalyst determines two fundamental properties: the elemental composition and the chemical state and its structure. Elemental composition depends on synthesis routes and intentional or unintentional doping, and can drastically affect both photocatalytic efficiency and material cost [9]. Similarly, the chemical state and structure, in

particular the oxidation state of the active metal, directly influence the charge-carrier generation and recombination processes of the photocatalyst [33].

Physical properties of the photocatalysts concern the optical absorption properties, crystallographic order of the material and material morphology. The optical absorption properties are determined by the band-gap energy and band-edge positions, defining the spectral range in which the photocatalyst activation occurs. Simultaneously, these properties define the charge-carrier dynamics (the mobility and lifetime of the generated charge carriers), which condition the probability of these carriers reaching the surface and performing the photocatalytic reaction. Crystallographic ordering defines the relations between atoms of the material through short-, medium- and long-range arrangements, affecting the mentioned optical properties, as well as the material stability over time. Lastly, the morphology of the material governs its specific surface area: bulk materials are characterised by a low surface area, whereas nanoparticles or other nanostructures maximise it. A high surface area increases the density of active sites available for photocatalytic reactions making it a more efficient process [33].

Among the available photocatalysts, titanium dioxide (TiO_2) has attracted significant attention due to its non-toxicity, chemical stability, abundance, and cost-effectiveness. Its major limitation TiO_2 is a relatively wide band gap energy, which confines its activity to the ultraviolet (UV) spectrum. Due to these properties, it is readily taken up and applied in photocatalytic applications. In the following Section, the properties of TiO_2 that contribute to its photocatalytic performance, including its crystal structure, phase composition, and surface characteristics, are discussed in detail [34].

2.1.2 TiO_2 photocatalyst properties, availability and applications

Titanium dioxide has a long history of application: as pigments, sensors, and catalysts. Relatively recently it has attracted significant interest in the scientific community due to its photocatalytic properties discovered in the early 1980s. These properties have broadened its applications to include photocatalysis, self-cleaning surfaces, and energy production [35].

TiO_2 can exist in both amorphous and crystalline forms. The crystalline forms of TiO_2 are generally classified into three polymorphs: anatase, brookite, and rutile. All crystalline TiO_2 phases are constructed from TiO_6 octahedra, where each titanium cation is six-fold coordinated to oxygen anions. The distinct TiO_2 polymorphs differ in the distortion of these octahedral units and in the manner in which they share edges or corners. Furthermore, the configuration of the octahedra is processing-condition dependent; anatase and brookite are generally considered metastable phases, whereas rutile is thermodynamically stable. Anatase predominantly consists of corner-sharing TiO_6 units, rutile is formed from edge-sharing TiO_6 units, and brookite exhibits a combination of both types of connections [32,36]. The chosen properties of each crystallographic form are summarised in Table 2.1.1. All TiO_2 phases are characterized by similar band gap values, activated by the light of the UV range. Moreover, due to the tetragonal arrangement of crystalline units in anatase and rutile, their optical properties are direction-dependent. Rutile exhibits enhanced light absorption at specific crystallographic orientations, while anatase, with longer crystallographic distances, shows less directional bias. Notably, upon light activation and independently from the phase structure, TiO_2 exhibits a low water contact angle, which facilitates its self-cleaning effect [37].

The literature concerning TiO_2 photocatalysis predominantly focuses on the rutile and anatase phases, as brookite is challenging to produce in pure form [38]. Based on current research, the anatase structure is claimed to possess the best photocatalytic properties among the three polymorphs, which is mainly attributed to the properties of its charge carriers. These charge carriers are characterised by longer lifetimes and lower effective masses compared to those in rutile, enhancing charge migration and reducing recombination [39,40].

In contrast to crystalline structures, amorphous TiO_2 lacks a periodic atomic arrangement, as its TiO_6 units are randomly linked, with some titanium atoms being under- or over-coordinated. Consequently, the distorted TiO_6 units form staggered chains rather than 3-D structures. As proposed in [17], resulting from this, high oxygen vacancy concentrations in amorphous TiO_2 enable creating a hole conduction channel, making it a better conductor than its crystalline counterparts. Moreover, amorphous TiO_2 is thermodynamically metastable and

can be converted to crystalline phases such as anatase or rutile through heat treatment [41]. Its optical properties closely resemble those of anatase, due to similar electronic structures, and unlike crystalline phases, amorphous TiO_2 is isotropic, meaning its efficiency does not depend on the angle of incident light. Additionally, the random arrangement of octahedra increases the high specific surface area of the amorphous TiO_2 structure, which enhances pollutant adsorption in the photocatalytic process [17].

Table 2.1.1 the TiO_2 crystallographic arrangements and their chosen properties, the presented band gap values are experimental (optical) [42].

Polymorph	Amorphous* [17]	Anatase	Brookite	Rutile
Unit cell	No periodic arrangement	Tetragonal	Orthorhombic	Tetragonal
Space group	-	$I4_1/amd$	P_{cab}	$P4_2/mnm$
Density (g/cm^3)	-	3.83	3.17	4.24
Band gap energy (eV)	-	3.20	3.27	3.00

*the properties of the amorphous TiO_2 are dependent on their production process

However, TiO_2 also has inherent drawbacks. In all crystallographic arrangements, TiO_2 is characterised by a relatively wide band gap, which restricts its activity to the UV region, limiting its applicability and efficiency as a self-sustainable photocatalyst. Furthermore, the overall efficiency of the photocatalytic process is often hampered by the ineffective conversion of photons into free radicals and limited pollutant adsorption on the catalyst surface [10]. As a result, one of the most critical objectives in photocatalytic research is the modification of TiO_2 to overcome these limitations and render the photocatalytic process more effective. Key modifications include extrinsic and intrinsic strategies. The extrinsic modification methods consist of:

1) Heterojunctions construction: Coupling TiO_2 with another semiconductor can lead to the physical separation of photogenerated charge carriers, diminishing recombination rates and enhancing photocatalytic performance [35];

2) Noble metal addition: the inclusion of noble metal nanoparticles can enhance the light-harvesting properties of TiO_2 in the visible/near-infrared wavelengths by promoting free electron generation [43];

On the other hand, the intrinsic methods include:

1) Crystal plane engineering: the photocatalytic activity of materials is strongly influenced by their exposed crystallographic facets (crystal planes). By synthesising hierarchical structures dominated by high-energy facets, such as the (001) plane in anatase TiO_2, surface reactivity and charge separation are enhanced, significantly increasing the photocatalytic performance [44];
2) Ion doping: the introduction of metal or non-metal ions, or co-doping strategies, can create defect sites in the TiO_2 lattice that reduce charge recombination. The effect depends significantly on the dopant type and concentration; cation doping may sometimes create recombination centres, whereas anion doping tends to facilitate better light absorption [32]. Co-doping can synergistically reduce the band gap while decreasing charge recombination [37];

In addition, the limited adsorption of pollutants can be improved by increasing the specific surface area of the photocatalyst. The morphology of TiO_2 can be tailored either by utilising appropriate production methods or through post-processing techniques [43]. Among the most well-known modifications there are: 0D quantum dots, 1D nanomaterials such as nanorods and nanotubes, 2D ultrathin atomic layers, and 3D structures. These architectures differently condition key properties such as specific surface area, adsorption capacity, and charge-carrier recombination dynamics, thereby influencing the photocatalyst's effective surface area and overall photocatalytic efficiency. As a result, the choice of morphology must be well-considered, as 0D, 1D, 2D, and 3D structures condition these properties divergently, necessitating alignment with the foreseen application's physicochemical demands [7].

Among the commercially available photocatalysts, Degussa (Evonik) P25 is the most widely used. P25 is a TiO_2 photocatalyst, typically sold as a powder consisting of major anatase and minor rutile phases, which contributes to its enhanced photocatalytic activity. Although it is

readily available and cost-efficient on a large scale, its UV-only activation and powder form limit its application in water remediation processes. Consequently, P25 is often used as a reference material for the development of modified photocatalysts or for self-cleaning applications [45]. The self-cleaning technologies are applied on large, flat surfaces (such as walls, glass, and pavements) and leverage the photocatalytic and photocatalytically induced hydrophilic properties of TiO_2 to provide anti-bacterial, anti-fogging, and wear-resistant features, as well as improved thermal management in buildings. Representative products include self-cleaning ceramics produced by Japan TOTO (Hydrotech™ technology), Activ™ self-cleaning anti-fog glass from Pilkington, and pavement materials such as TioCem® and TX Active® [37,46]

Despite the success of commercially available TiO_2 and the sustained interest in photocatalysis for water remediation, availability of the commercial systems is extremely limited and predominantly involves slurry (powder-based) reactors [47]. While the conducted research has focused on material customisation and development, the design and evaluation of complete photocatalytic systems have been neglected. The main unresolved challenges relate to system efficiency and ease of handling [11]:

- Existing slurry systems are often unoptimized, resulting in low energy efficiency, slow reaction kinetics, and issues such as catalyst fouling or photoaggregation;
- Systems based on immobilised TiO_2 offer improved handling but may suffer from reduced catalyst surface area, reduced illuminated catalyst area per unit volume of water treated, and higher rates of photon scattering;

Advances in materials science and reactor engineering may yield opportunities to enhance photocatalytic water treatment performance. In particular, niche applications that utilise customised TiO_2 materials, combined with immobilisation techniques that preserve the catalyst's intrinsic properties, while providing photocatalyst durability could establish a new foundation for commercial applications [11].

2.2 Overview of TiO_2 deposition methods

Depositing oxide materials requires the selection of a process capable of immobilising brittle, typically crystalline, oxide particles which is a challenging task. Critical factors such as equipment and component costs, as well as the scalability of the method, influence both the feasibility of the chosen technique and the accessibility of the final product. At the same time, the deposition process must be evaluated for its effect on the properties of the immobilised photocatalyst [48].

Available deposition techniques differ in several key aspects, including processing temperature, reaction environment, the phase from which the oxide material is deposited (e.g., vapour, solution, melt, or solid), and the nature of the support material used for immobilisation. These parameters collectively determine the resulting photocatalyst characteristics. Important outcomes include the phase structure, adsorption capacity, specific surface area, and bond strength with the substrate – all of which constrain the photocatalyst's practical usability [49].

One of the main challenges is achieving a balance between preserving the inherent photocatalytic properties of the original material and providing sufficient bonding and mechanical stability to ensure safe operation. This difficulty often arises from the use of thermal energy to promote adhesion between the deposited material and its support; however, excessive heat can degrade the functional properties of the photocatalyst itself [48].

The selected deposition methods are summarised below and systematised according to the state of matter (solid, liquid, gas, or plasma) utilised during deposition, to clarify their distinct influences on the resultant material properties.

2.2.1 The vapour-phase deposition processes

Chemical vapour deposition (CVD) allows for the deposition of thin oxide coatings from the gaseous phase. In this process, precursors are vaporised and transported into a heated reactor using a carrier or source gas. Elevated temperatures trigger the oxidation of the precursor, forming solid phase particles. Chemical reactions occur on or near the hot

substrate surface, resulting in the formation of a thin film. CVD is typically used for surface functionalisation, as it offers superior control over the coating microstructure and can enhance the specific surface area using a wide range of materials [49]. Among the various CVD methods, atmospheric pressure chemical vapour deposition (APCVD) is a one-step process that offers precise control over the size and crystallinity of the deposited material. Since the reaction chamber operates at approximately one atmosphere, the process is more cost-effective due to the elimination of vacuum systems [50,51]. It is also possible to lower the CVD deposition by choosing such a process as the plasma-enhanced chemical vapour deposition (PECVD) [52]. This method operates at lower temperatures, thanks to plasma-driven reactions [53].

Another process enabling the deposition from the vapour is the physical vapour deposition (PVD). The PVD deposition process resembles closely the CVD technique, depositing thin, dense films by vaporising the source material and transporting it to the substrate in a vacuum or low-pressure environment. The condensation of the vapour, via nucleation and growth, results in the formation of a coating, enabling the deposition of elements, alloys, and compounds [54]. Among the most often used processes, is a sputter deposition technique. In this process, the coating material is ejected from a target by bombardment with high-energy plasma, and the resulting atoms form the coating upon condensation. This method is primarily used to produce oxide and nitride coatings with high conductivity or wear resistance [54,55]. Another well-established method is the thermal evaporation. To create a coating the target material is thermally evaporated in a vacuum and subsequently condensed on a substrate [54].

The overview of the chosen methods' characteristics as well as advantages and limitations are presented in Table 2.2.1. These vapour-phase deposition techniques inherently rely on elevated temperatures to achieve homogeneous, crystalline TiO_2 coatings, while allowing to create a strong bonding between the support and the coatings. Relying on the high-temperature range for deposition makes it unlikely to produce amorphous materials and can lead to the brittleness of the coating. The thickness of the coatings is also limited, due to inherent deposition characteristics. Additionally, the methods are challenging to scale, as with

the increase of the samples the equipment also needs to be scaled, increasing the cost of the process [56].

Table 2.2.1 the overview of the CVD and PVD techniques.

Method	Characteristics	Limitations	Advantages
Atmospheric pressure (APCVD) [50,51,53]	Thickness: < 1 µm Process temp.: 500-1000°C	• Not compatible with the heat-sensitive substrates • Possibility of airborne impurities	• Cost-effective process (lack of a vacuum chamber) • Thickness and morphology adjustment
Plasma enhanced (PECVD) [53,57]	Thickness: < 1 µm Process temp.: <500°C	• Additional cost for equipment (plasma generators) • Not scalable method • Often thermal post-processing is needed	• Relatively low-temperature process • Possible to coat complex geometries
Sputter deposition [54,58–60]	Thickness: < 5 µm Process temp.: 100-1000°C	• Limited size due to the vacuum conditions • High cost of the equipment	• Able to coat complex components • High purity of the coating • Wide range of coating compositions
Thermal evaporation [54]	Thickness: < 1 µm Process temp.: 150-750°C	• Limited to planar surfaces • Difficult to obtain nanoporous coatings	• High purity of the coating • Wide range of coating compositions

2.2.2 The melt-state deposition processes

The thermal spray (TS) methods require the preparation of the feedstock powder, which over time has evolved from a dry powder form to suspension and even liquid feedstock for many processes. However, since most suspension-based thermal spray techniques (except for suspension plasma spraying) are still under development, only the powder-fed processes will be discussed in this Section. One of the most often chosen TS techniques is plasma spraying, which utilises a partially ionised conductive gas (plasma) to melt and propel the powdered material onto the substrate, where rapid solidification forms a dense coating. Owing to the wide range of compatible materials and the ability to tailor the coating properties [61].

Detonation gun spraying (D-gun spraying) involves controlled explosions of oxygen-fuel gas mixtures within a tubular barrel, generating high-pressure shock waves that accelerate

powder particles to hypersonic velocities [62]. Compared to plasma spraying, particle heating is more moderate in D-gun spraying, but the particles attain higher kinetic energy [63]. The layer-by-layer deposition characteristic of D-gun spraying allows precise control over coating thickness. This method produces dense, well-bonded coatings with compressive residual stress, resulting in higher wear resistance than those obtained by plasma spraying [62].

High-velocity oxy-fuel spraying (HVOF) shares similarities with D-gun spraying. In HVOF, a combination of oxygen and fuel gases or liquid hydrocarbon is combusted in a chamber to create a highly pressurised mixture, which is then expelled through a converging-diverging nozzle to form a supersonic jet. Although the entrained particles are accelerated, their temperature is lower than in the aforementioned processes due to gas expansion. Moreover, HVOF is a continuous process. The high kinetic energy of the particles produces a hammering effect on the deposited surface, yielding coatings with very low porosity (near theoretical density) [63]. However, the adhesion strength of HVOF coatings may be lower than that of D-gun sprayed coatings [62].

The summarisation of the melt-state techniques' characteristics is presented in Table 2.2.2.

Table 2.2.2 the overview of the chosen thermal spray techniques.

Method	Characteristics	Limitations	Advantages
Plasma spray [58,64–66]	Thickness: 50-5000 µm Gas temp.: 8000-14000°C	• Difficulty in coating complex components • Difficulty in obtaining a nanoporous coating • High residual stress, high porosity of the material	• High deposition rate • Wide range of coating compositions
High velocity oxy fuel (HVOF) [58,65,66]	Thickness: 50-5000 µm Gas temp.: 1600-3100°C	• Lower deposition efficiency than in APS • Residual stress in the material • Difficulty in coating complex components	• Dense, coatings with good adhesion • Lower porosity level than in APS
Detonation gun spraying (D-Gun) [64,66–68]	Thickness: 50-5000 µm Gas temp.: 2000-3900°C	• Lower specific surface area of the coating • Spraying powders in the liquid state • Not scalable method	• Dense, coatings with good adhesion • Coating is heat-hardened • Lower porosity level than in APS

Presented thermal spraying processes employ elevated temperatures which allows to produce dense, strongly bonded coatings. Additionally, the use of a directed spraying apparatus (spraying guns) enables selective deposition on specific surface regions and linear control over coating thickness, offering versatility in component design. However, high-temperature-induced limitations persist: the inherent high thermal input often compromises the original microstructure and chemical composition of the feedstock powder, whilst process-induced porosity remains difficult to regulate, adversely affecting the mechanical integrity of the coatings [69].

2.2.3 The liquid-state deposition processes

The spin coating method is often combined with the sol-gel method (described in Section 2.4.2). The sol-gel process is a synthesis method that allows the production of nanomaterials in bulk, powder or film form. When paired with spin coatings, the sol-gel process is used to produce a sol (a colloidal suspension of very fine particles in a continuous liquid medium). The spin coating deposition process uses a small volume of sol, which is applied onto a flat substrate. Afterwards, the substrate is rotated at a controlled speed. The centrifugal force spreads the sol uniformly over the surface, and a subsequent heat treatment stabilises the coating [70].

Electrochemical deposition utilises a standard cathode-anode system to deposit coatings. In this process, dissolved metal ions from an electrolyte are reduced onto a conductive substrate (serving as the cathode). The operating conditions determine the microstructure, grain size, and mechanical strength of the deposited layer [71].

The coating methods summarised in Table 2.2.3 enable the production of distinct coating types. The liquid-stated deposition methods enable the immobilisation of materials that are incompatible with high-temperature processes. This creates an opportunity for material modification, as the deposition temperatures are low and allow retaining the material initial properties, unlike in vapour- and melt-state methods. Spin coating facilitates rapid, uniform deposition on planar substrates, accommodating diverse materials. However, the thickness of

the method is limited, as well as the control over the coating morphology. In contrast, electrochemical deposition allows precise control over coating morphology, enabling porous or nanostructured architectures, but with a similar thickness limit. Both methods allow for forming uniform thin coatings, however, their utility for thick is restricted [56].

Table 2.2.3 the overview of the spin-coating and electrochemical deposition techniques.

Method	Characteristics	Limitations	Advantages
Spin coating [56]	Thickness < 1 µm Room deposition temperature	• Needs drying/baking process to stabilise • Not scalable • Layering not possible (above two)	• Easy material modification • Low cost • Uniform thickness
Electrochemical deposition [71–73]	Thickness: <2 µm Process temp.: <65°C	• Limited thickness • Moderate coating adhesion • Needed post-treatment • Applied on conductive substrates	• Customizable pore sizes, porous structures, and compositions • Uniform • Scalable process

2.2.4 The solid-state deposition processes

The solid-state deposition methods discussed here represent a subset of TS processes. While sharing similarities with conventional TS (such as feedstock material propulsion) these techniques differ fundamentally by utilising kinetic energy rather than thermal energy to drive particle deformation and bonding. By accelerating powdered feedstock to supersonic velocities, the impact-induced plastic deformation enables coating formation. This approach may appear contradictory for oxide feedstock powders, which typically lack ductility. However, optimising feedstock parameters properties allows dense, strongly-bonded oxide coatings [74].

High-pressure cold spraying (HPCS) is the most often chosen TS method that relies primarily on kinetic, rather than thermal, energy. In HPCS, inert gas is accelerated through a converging-diverging nozzle, entraining the powder particles which then deform plastically upon impact to form a bond with a substrate. Compared to other TS processes, HPCS has the greatest potential to preserve the initial properties of the deposited material [64]. However, due to the dynamic nature of the process, phase changes are common [66].

Low-pressure cold spray (LPCS) is a low-pressure variant of the cold spray technique. This process takes place under ambient conditions and relies on the kinetic energy of particles. The particles are accelerated through a converging-diverging nozzle and directed towards the substrate. LPCS is commercially used for depositing materials that deform easily upon impact, and its portability allows for on-site repairs. New applications become feasible when LPCS is combined with a bottom-up approach for powder preparation that involves assembling material from smaller units such as atoms, molecules, and smaller particles to obtain the desired product [75] and enables the deposition of oxide powders [76].

Aerosol deposition (AD) is another kinetic spray process that uses the kinetic energy of accelerated particles to facilitate deposition; however, the process is conducted in a vacuum. The substrate is placed inside a vacuum chamber, and due to the pressure difference, the atomised particles are drawn into the chamber and directed towards the substrate through the converging-diverging nozzle [58].

Table 2.2.4 summarises the features of the kinetic deposition techniques discussed above.

Table 2.2.4 the overview of the chosen kinetic spray techniques.

Method	Characteristics	Limitations	Advantages
High-pressure cold spray (HPCS) [63,65,66]	Thickness: <1 cm* Gas temp.: 500-1000°C	• Deposition can cause substrate erosion on non-metallic substrates	• Wide range of coating compositions • Possible thick coatings • Scalable process
Low-pressure cold spray (LPCS) [58,66,77,78]	Thickness: <1 cm* Process temp.: 200-650°C	• The high porosity of the material • Constrained by deformable materials	• Scalable process, on-site process • Characterised by the lowest cost out of TS
Aerosol deposition (AD) [58,59,79]	Thickness 0.5-50 µm; Room deposition temperature	• Not scalable process; • Deposition only on planar surfaces; • Low deposition efficiency (<1%); • Lower specific surface area of the coating	• High-density coatings (porosity can be determined); • Possible selective coating of the surface; • Uniform

Low-pressure and high-pressure cold spray (LPCS/HPCS) are classified as additive manufacturing techniques owing to their capacity to fabricate free-standing structures [80]. However, in coating applications, the maximum feasible thickness is conventionally limited to 1 cm, beyond which the deposited material transitions from a functional surface layer to a bulk component, redefining its classification.

High-pressure cold spraying (HPCS) offers the greatest material versatility; however, its high particle velocities can induce phase transformations and microstructural changes, and the process is challenging to scale due to specific deposition conditions, like the use of protective gases. In contrast, low-pressure cold spraying (LPCS) preserves the feedstock's original properties and is readily scalable, but its lower impact energy restricts deposition to ductile materials and can result in reduced adhesion. Aerosol deposition (AD) produces exceptionally dense and strongly bonded coatings, yet suffers from low deposition efficiency and is limited to relatively thin films [66,81].

Low-pressure cold spraying (LPCS) stands out as the most accessible and functions independently of controlled environments, requiring no inert gases or vacuum conditions, producing coatings layer-by-layer without high-temperature or vacuum equipment. Furthermore, scaling LPCS for larger surfaces requires only a proportionate increase in the deposition process time rather than an entirely new furnace or vacuum systems purchase, making it cost-effective for large-area coatings. Unlike vapour- or thermal-phase methods, LPCS preserves the original physical and chemical characteristics of feedstock powders (retaining phase, morphology and functionality) because no melting or oxidation occurs during impact bonding. Compared to liquid-phase methods it allows thickness customisation and deposition on other than flat surfaces. The LPCS low material versatility can be overcome by utilising custom feedstock powders. Consequently, the LPCS kinetic method, coupled with tailored powder engineering provides a readily available, highly adaptable coating solution that preserves the functional performance of the original feedstock material [66,69]. Thus, this method is chosen to be used for the TiO_2 immobilisation in this thesis. In the following Sections, the bonding mechanism of kinetic deposition methods and the LPCS operation mechanism are described.

2.3 Kinetic spraying processes for oxide feedstock powder deposition

Initially, the kinetic spray process was designed for depositing metallic feedstock powder onto metallic substrates. Unlike other thermal spray processes, kinetic spray relies on the kinetic energy of solid particles and their subsequent deformation rather than on heat and melting. A solid-state material deposition is achieved using a specially designed converging-diverging nozzle – de Laval nozzle (Fig. 2.3.1), that accelerates particles to velocities exceeding 300 m/s. The feedstock particles are entrained by the working gas, which gains speed in the nozzle and directs them towards the substrate. Deposition occurs when these high-velocity particles deform upon impact, forming metallurgical and mechanical bonds at their interfaces. This approach mitigates many of the uncontrolled material alterations associated with high-temperature processes [82].

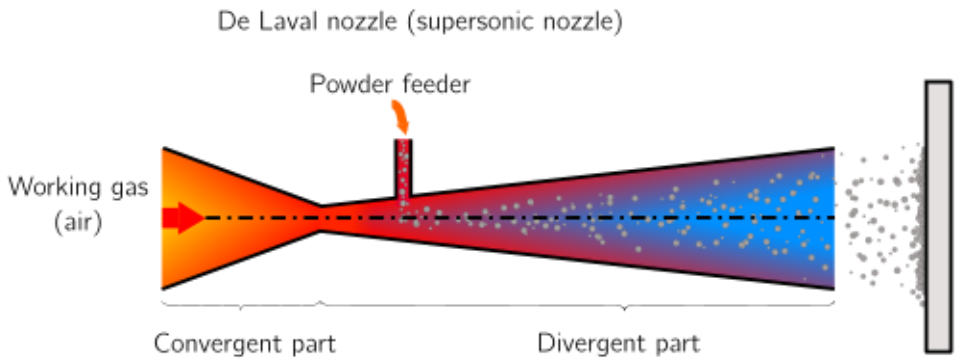

Fig. 2.3.1 Schematic representation of the de Laval nozzle used in the kinetic spray process, where the powder is fed through downstream injection.

Feedstock powder can be introduced in the kinetic spray process in two ways: upstream and downstream injection. In upstream injection, particles are picked up by pressurised working gas before entering the converging-diverging section of the nozzle. In the converging part, the pressure is higher than ambient, so the particles must be forcefully injected into the gas stream, necessitating a high-pressure powder feeder system. In downstream injection, particles are introduced after the nozzle's converging-diverging section; as the pressure in the nozzle decreases towards the exit, the powder feeder operates at lower pressures, thereby facilitating particle entrainment [83].

In cold spray, the primary objective is to accelerate particles to a velocity equal to or exceeding their critical velocity – a material-dependent threshold required for successful deposition. Particle velocity is influenced by the working gas (e.g., air, nitrogen, helium, argon, or their mixtures), gas nature (inert or weakly reactive gas), its pressure and temperature, the geometry of the de Laval nozzle, and the particles shape and size [84]. As the working gas expands through the divergent section, it gains supersonic speeds while its temperature drops due to expansion, further accelerating particles. The highest particle temperature, after exiting the nozzle, is reached upon impact with the substrate and mainly depends upon inertial force, kinetic and thermal energy (particle velocity and temperature) [85].

The selection of the working gas is crucial in kinetic spray processing. Inert gases such as helium and nitrogen are preferred due to their lower molecular weight, which allows for higher particle velocities and more efficient deposition. At the same time, their higher cost, significantly increases process expenses, driving interest in more economical alternatives such as air or gas mixtures [83].

Due to the high velocity of the flow, shock waves inevitably form at the nozzle exit and in front of the substrate, when the process is carried out in the ambient environment. As the jet exits the nozzle it must adjust to downstream conditions (ambient pressure) or disturbances (i.e. substrate) on its way. As a result of the pressure difference between the jet and the ambient environment, the jet expands rapidly generating shock waves called nozzle exit shock. Fortunately, these shock waves (formed at the nozzle exit) primarily affect small and lightweight particles [86]. Another shock wave is formed in front of the substrate due to the sudden deceleration of the supersonic jet upon impact and due to this it is called the substrate bow shock. This rebound jet produces infinitesimal pressure waves that travel upstream at the speed of sound. However, the continuous jet flow prevents these waves from propagating freely, causing them to coalesce a short distance from the substrate, forming a shockwave. Although the resulting shock wave is extremely thin – approximately the mean free path of the gas molecules; its coalescence creates an enclosed region, known as the bow shock, which has a more significant effect on particle behaviour in kinetic spray [87].

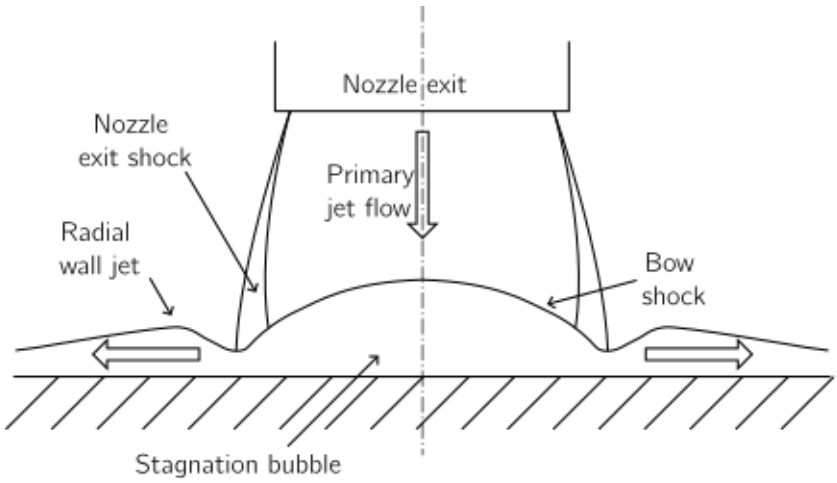

Fig. 2.3.2 Schematic diagram of the supersonic impingement zone at the exit of the de Laval nozzle [87].

For successful deposition, particle velocity must meet or exceed the critical velocity. Since this critical velocity is inversely proportional to particle size, smaller particles require higher velocities. This poses a challenge for depositing fine particles, as those with insufficient velocity may be deflected by the bow shock or filtered out entirely. Conversely, if particle velocity is too low, larger particles may cause substrate erosion or hammering rather than deposition [87]. Particle velocity can be adjusted by modifying the working gas pressure, type and temperature, powder feed rate, powder properties itself (discussed in the next Section 0), and the stand-off distance, as well as the nozzle geometry (which will affect the formation of shock waves in front of the nozzle) [88].

The complexity of the deposition process means that the precise bonding mechanisms are not yet fully understood, largely due to the lack of in situ techniques capable of real-time observation of single-particle impacts (well-established theories are discussed in the following paragraphs) [89]. In general, material deposition in kinetic spray results from the consecutive impacts of micron-sized solid particles causing the particles to interlock into the substrate and forming a first coating layer, which is followed by the metallurgical bonding (chemical interaction between the particle and a substrate) over a significant fraction of the particle-particle interfaces [90]. The kinetic energy gained by the particles determines the type of bonding and the bond strength (if no further processes are applied) [89]. Once the initial coating layer is established on the substrate, further material build-up occurs as subsequent

particles deform and realign. The repeated impingement of particles generates high contact pressure, which reduces voids, densifies the material, and facilitates chemical reactions between particles [91]. Brittle particles may deform through cracking or simply fracturing upon the impact, however, only the former mechanism enables the effective coating build-up [81].

2.3.1 Deposition mechanisms in kinetic spraying methods

The properties of the feedstock powder, particularly its ductility – governed by the chemical bonding of the atoms comprising the material – determine the deposition mechanism in kinetic spraying. This mechanism varies significantly between deformable and brittle feedstock powders [92]. Both scenarios are discussed in the subsequent Sections.

2.3.1.1 Deposition of deformable particles

The key theories concerning the deposition mechanisms in kinetic spray are established based on the single-particle impact, approaches typically involving metallic particles on metallic substrates [88]. The initial stage (also referred to as the incubation time) involves particles rebounding and eroding the substrate to activate its surface [93]. Ductile, metallic particle deposition in kinetic spraying is achieved when particles reach or exceed the critical velocity value, allowing them to pass through the bow shock and impact the substrate with sufficient energy. Afterwards, due to high pressures generated at the substrate-particle interface or particle-particle interface, the material is subjected to high strain rate deformation processes facilitating the local adiabatic shear instability [94]. As a result of this instant, intense deformation the unmelted jet is formed [90].

Several hypotheses have been proposed to explain particle bonding in kinetic spray [90]. Firstly, the metallurgical bonding is believed to occur in ductile particles when surface oxides are removed and cleaned by the unmelted jet. At the atomic level, metallurgical bonding refers to chemical interactions, which are possible only after the surfaces are cleaned and oxide-free. The formation of such bonding is indicated by the intermetallic formation [90,95]. Secondly, mechanical interlocking, results from the jetted particle/substrate interactions which undergo "mixing" at the interface, ultimately increasing the interfacial area and promoting particle

substrate interlocking [90,96]. Subsequent research has led to the following conclusions regarding bonding mechanisms [89]:

- The interfacial melting and inter-diffusion play minor roles in the kinetic spray bonding mechanism.
- The mechanical interlocking of particle-substrate interfaces is the primary bonding mechanism.;
- High contact pressures contribute to the adhesion of jet-cleaned interface;
- The adiabatic shear instability and interfacial flow ultimately facilitate the creation of the 'surface-scrubbing' jets which clean contacting surfaces strengthening the bonding;
- Interfacial "mixing", observable as roll-ups, vortices and rivet-like interlocks, enhances the bond strength.

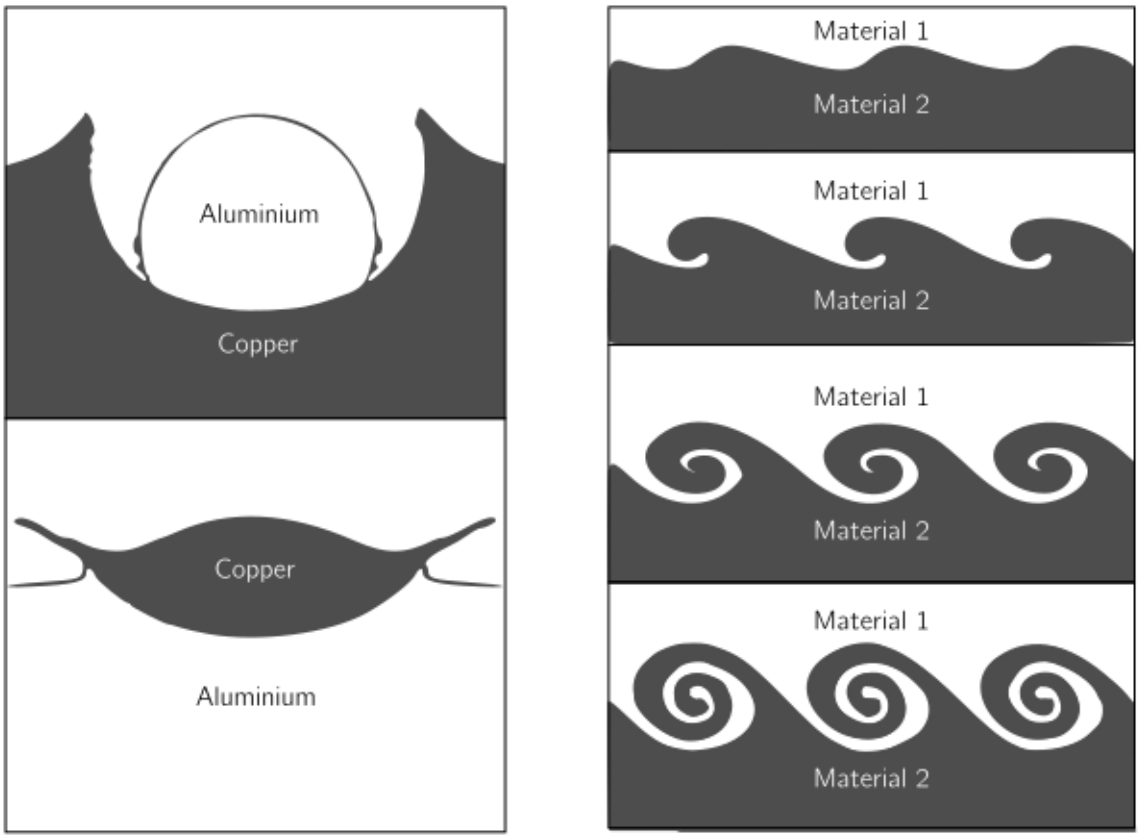

Fig. 2.3.3 On the left, shapes of feed-powder particles and substrate craters 50 ns after initial contact for (a) an aluminium particle at 400 m/s and (b) a copper particle at 500 m/s. On the right, a schematic of the instability-driven evolution of the particle/substrate interface illustrates the formation of interfacial roll-ups and vortices. Adapted from [96].

Extensive research has been undertaken to identify factors affecting deposition efficiency in kinetic spray. The key variables include:

- Particle velocity: determined through such process parameters as working gas temperature or pressure. However, it is also affected by the particle size and their shape. The particle velocity attained is inversely correlated with their size (within the particle size range optimal for kinetic spraying) [61,97];
- Materials density: the material density affects the velocity attained by the particles, which diminishes with increasing density, ultimately influencing yielded stress when the material impinges onto the substrate [94];
- Substrate material and state: a softer substrate material is more prone to jet formation, which facilitates both metallic and mechanical bonding. Additionally, increasing the roughness of the substrate is known to facilitate better particle anchoring. However, surface processing, such as grit-blasting of soft substrates might cause the surface particle-strengthening of the material, restricting the jet formation and lowering the strength of the bonding [90].

2.3.1.2 Deposition of non-deformable, brittle particles

Ceramic material deposition, due to the inherently harder and more rigid structure, cannot rely solely on the shear deformation mechanisms observed in ductile, metallic materials. Although the concept of using a high-velocity kinetic process with brittle ceramic powders may seem contradictory, even fine ceramic powders can exhibit plastic-like deformation under extreme pressures at the impact zone [76]. In contrast to ductile materials, the deposition mechanism for ceramics involves both plastic and inelastic deformation, with the plasticity observed in ceramics originating from different underlying mechanisms [92].

The deposition process of brittle particles follows the same behaviour as that of ductile particles up to the point of the jet creation in the interface. Similarly, to ductile material, the deposition process of brittle particles in a kinetic spray is still under investigation and currently there are several main theories which still are being investigated [92]. One theory,

known as room temperature impact consolidation (RTIC), is based on the hypothesis that new activated surfaces are created which allow the bonding between particles to happen. Upon collision, cracks appear in the crystalline particle and due to instantly rising pressure the particles are finely crushed, which yields new active surfaces (Fig. 2.3.4). Those surfaces bond under high pressures and inertial forces, facilitating a brittle-to-ductile transition [77]. For the process to take place small particles need to be applied (<5 μm), which for some processes operating in ambient conditions poses a challenge, since such small particles cannot pass through the bow shock [98]. The successful deposition of the small, brittle particles in the ambient-conditioned kinetic processes is achieved through the agglomeration of particles. The creation of larger, clustered particles has proven effective for deposition in the presence of the bow shock [99].

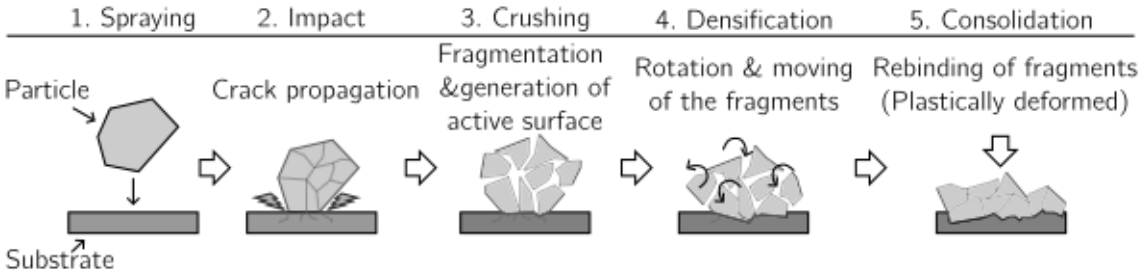

Fig. 2.3.4 the scheme of one of the brittle particle deposition mechanisms: the room temperature impact consolidation (RTIC) [77].

Another deposition mechanism is based on the facilitation of the brittle particle mechanical interlocking process. The anchoring process is often achieved by utilising a malleable substrate, such as aluminium, which promotes shear instability and leads to material jet formation in the interface. While enhanced interface surface area provides mechanical interlocking of the particles [100–102], the brittleness of the particles limits the coating build-up, allowing to deposit only thin coatings. This limitation can be resolved when instead of using single particles the agglomerates are used as a feedstock powder. Using the agglomerates allows the material to build up through their fragmentation and densification upon impact [23,102]. Other approaches include creating a rough and rigid interfacial layer via high-temperature thermal spray processes (e.g. plasma spraying) to serve as a geometric trap for brittle nanoparticles [103]. What is more, recent studies have suggested that chemical bonding may

contribute to the adhesion of brittle particles. When the oxide layer on the substrate material is thin, it may fracture upon impact, increasing the chance of chemical interactions between the newly exposed, oxide-free substrate and the deposited particles [104,105].

Research on ceramic feedstock powder deposition reveals three primary modes of particle behaviour on impact: rebounding, bonding, and fragmentation. The rebounding particles have the lowest velocity on impact and are the result of the back-striking elastic forces between the impacting particle and the substrate. Particles tend to retain their initial shape, aside from the small fragments that adhere to the substrate. Bonding particles are characterized by the middle range of velocities (lower than fragmenting particles) and, upon impact develop cracks in the top part, which do not extend to the surface, allowing them to flatten and bond. The particle deformation stems from the spread of the area of shear localization into the particle, as a result of the enhanced contact area between the particle and substrate. Particle fragmentation concerns the fastest particles and usually produces more than two separate parts. Prior to fragmentation, the particle undergoes deformation, following the same mechanism as observed for bounded particles, except that the cracks reach the outer surface and result in fragmentation. The particle size is crucial; larger ceramic particles are more likely to rebound or fracture without significant deformation [81].

The primary difference between brittle and ductile particle deposition lies in their deformability. Brittle particles are characterised by a low strain to failure (poor capacity to change shape under stress) causing them to fracture upon impact during kinetic deposition (due to their inability to undergo significant plastic deformation). The ductile particles, on the other hand, can absorb impact energy through plastic deformation, facilitated by localized shear instabilities that generate heat, leading to thermal softening and further deformation [92].

As briefly mentioned before, in ambient kinetic spray processes, the bow shock forms in front of the nozzle, complicating particle-substrate interactions [76]. As a result, in those ambient-atmosphere processes to reach the substrate, larger particles need to be used, which is possible through the brittle powder agglomeration. Such agglomerates should be about 15 μm in diameter to pass through the bow shock and should be porous to easily allow the flattening

of the particle upon impact. Additionally, to make the flattening process even more effective the crystal lattices of the individual nanoparticles should be arranged so that they continue seamlessly from one particle to the next, promoting a uniform, coherent structure [76,92]. For finer particles, a brittle-to-ductile transformation may occur, with the primary deformation mechanism attributed to localised inelastic deformation along slip systems and shear localisation at their intersections [81].

In summary, the deposition mechanism for ceramic feedstock powders in kinetic spray can be described as follows:

- The main bonding mechanism largely depends on the deposition conditions: a protective atmosphere might facilitate chemical bonding by limiting oxide formation on the substrate [104], while ambient conditions favour bonding through substrate deformation and particle interlocking [106]. Additionally, in some cases it is possible to achieve chemical bonding, even on an oxidized substrate, however, the particles need to have enough energy to break through the oxide layer enabling bonding of clean interfaces [105];
- Finer particles are required (compared to ductile materials) in order to enable deformation through the localized inelastic deformation and shear localization, avoiding fragmentation of the particles and enabling the build-up process [81];
- Unlike ductile materials, where the plastic deformation is localized at the particle-substrate interface, in brittle particles highly deformed areas spread as shear cones towards the particle centre, making the strain distribution much less localized [81].

2.3.2 Low-pressure cold spray process parameters

The low-pressure cold spray (LPCS) process operates at lower working gas pressures (<1 MPa). The working gas (typically compressed air, though protective gas or gas mixtures may also be used) is heated before passing through the nozzle. Due to the lower pressure and velocity, particles attain reduced kinetic energy upon impact. To improve powder flowability, the feedstock powder is typically introduced into the diverging section of

the nozzle, preventing backflow. Additionally, an external carrier gas may be employed to enhance powder entrainment. Simultaneously, the heated working gas passes through the nozzle, accelerating the supplied particles and aiming them at the substrate [76]. The reduced amount of energy supplied to the particles in LPCS grants the opportunity to largely retain the initial powder properties which are often lost due to the contact with heated carrier gas or heat generated via adiabatic shear instabilities when the particles deform upon impact, like in HPCS [76,107].

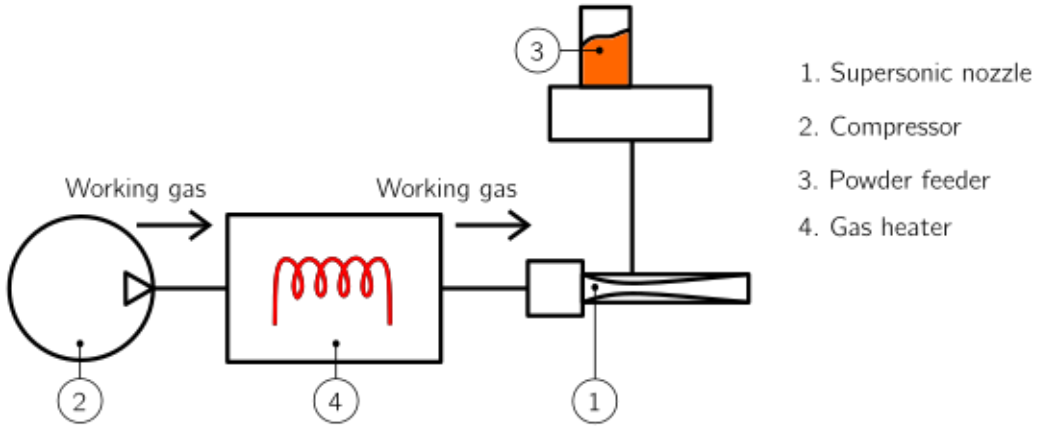

Fig. 2.3.5 Schematic diagram of a low-pressure cold spray (LPCS) setup. Adapted from [108].

The low-pressure cold spray (LPCS) process is among the simplest thermal spray techniques in terms of equipment configuration. Consequently, the number of process parameters requiring optimisation is relatively limited. The most critical parameters influencing deposition efficiency and coating properties include working gas type, pressure and temperature, stand-off distance, spray angle, traverse speed, scanning step, and number of layers or nozzle geometry. The properties of the feedstock powder, which also significantly affect deposition, will be discussed separately in the next Section.

The working gas pressure and temperature directly affect the stream acceleration process and as a result the particle acceleration and their velocity upon impact. of these two parameters, temperature has a more significant influence on the particles' velocity and hence on the deposition efficiency. The rise of the temperature consistently increases the particles' velocity, whereas an increase in gas pressure also contributes to velocity gain, though its effect is less pronounced. This suggests that while pressure optimisation is beneficial up to a certain

point, further increases have a marginal effect [109,110]. Additionally, the molecular weight of the gas affects its acceleration capabilities; lower molecular weight gases (e.g., helium) enable higher acceleration, thereby enhancing particle deposition efficiency [110].

The stand-off distance, which is the dimension between the end of the nozzle and the substrate, has an immense influence on the deposition efficiency, primarily due to its effect on the bow shock formation. At large stand-off distances (>120 mm), the bow shock disappears, however, the working gas velocity decreases below the particles' velocity, leading to particle deceleration and kinetic energy reduction, ultimately lowering the deposition efficiency. In the middle ranges of the stand-off distance (50-120 mm), bow shock can appear, however, it has limited influence over the particles and the stream allowing gas velocity to remain higher than particle velocity, further accelerating the particles prior to impact. At small ranges (10-50 mm), similarly to the middle range stand-off distance, particles are accelerated by the working gas, however, bow shock effects are more pronounced, gradually intensifying as the distance decreases, ultimately reducing deposition efficiency [87]. As a result, a moderate stand-off distance is generally recommended for LPCS, though the optimal range should be determined experimentally based on nozzle design and working gas properties [111]. Moreover, increasing stand-off distance often results in higher surface roughness, as more particles experience rebound or fragmentation, leading to a less compact and uniform coating [112].

The spraying angle directly affects particle impact energy. The most effective conditions for deposition in cold spray occurs when the nozzle is perpendicular to the substrate material; creating the highest amount of energy. Angled spraying introduces tangential momentum, leading to non-uniform deformation of particles upon impact, which may weaken coating adhesion strength [80,113]. Recent studies on deformable metallic particles (e.g., aluminium) have reported variations in adhesion performance at non-perpendicular angles, with certain cases demonstrating enhanced bonding at 60° [113], nevertheless, the 90° deposition strategy is still a default setting used.

The traverse speed, which defines the linear movement rate of the spray gun, directly influences coating properties such as roughness, porosity, and microhardness. A lower traverse speed results in higher particle density per unit area, facilitating inter-particle bonding and higher deposition efficiency. Additionally, a lower traverse speed increases substrate temperature, facilitating mechanical interlocking, which enhances coating adhesion. As a result, porosity is minimised, while roughness and microhardness are more pronounced [113]. At moderate traverse speeds, deposition efficiency continues to increase gradually due to reduced erosion and fewer particle-to-particle collisions. This leads to a more uniform particle distribution on the surface, reducing surface roughness, although porosity slightly increases, and microhardness decreases. At high traverse speeds, deposition efficiency drops significantly. The faster gun pass results in insufficient coating build-up, as fewer particles reach the substrate. Additionally, the substrate temperature is lower, reducing the effectiveness of mechanical interlocking. Consequently, coatings are thinner, with reduced adhesion strength [114].

The scanning step determines the overlap between adjacent spray passes, affecting coating thickness, uniformity, and roughness. The optimal scanning step is typically set to half the width of a single spray track, ensuring a flat, even coating. However, deliberate modifications to this parameter can be used to tailor surface roughness and coating thickness [108]. Reducing the scanning step improves surface smoothness and enhances deposition efficiency and coating thickness [115].

The number of layers (passes) influences coating roughness, porosity, and cohesion strength and thickness. Rather than smoothing the surface, additional layers amplify surface undulations, increasing surface roughness [116]. The most pronounced effect is observed in cohesion strength, depending on the amount of passes the porosity of the coating may change, due to weakly bonded particles and pores which serve as the initiators of the cracks, lowering the cohesion. Applying multiple thin layers prevents excessive porosity formation and mitigates cohesion loss. The residual stress and bond strength remain largely unaffected by the number of layers [117].

Finally, material properties, such as feedstock powder characteristics, play a critical role in kinetic deposition processes. These aspects will be discussed in greater detail in the following Section.

2.4 Fabrication of the oxide feedstock powder for the cold-spray process

The size range of particles used in cold spraying has evolved significantly, spanning from nanoscale up to 150 μm [118]. With the advancement of cold spray technology, the powder manufacturing industry needed to adapt to refine the particle size fractions, as the larger particles are difficult to accelerate. Nowadays, the most frequently requested particle size fractions are typically within the ranges of 5–25, 15–45, 63–90 and 75–150 μm diameter. This refinement has been achieved through particle size reduction techniques, such as crushing, ball milling, and jet milling, as well as particle enlargement methods, including sintering, fusion, and agglomeration. While these advancements have significantly improved the deposition efficiency for ductile materials, the deposition of brittle particles remains a challenge. Further research is required to facilitate the commercialisation of brittle particle deposition via kinetic spraying [119].

2.4.1 Critical powder properties and the powder production methods

Several key requirements must be met by powders intended for kinetic deposition:

- Flowability: Ensuring a stable and continuous powder-feeding process is critical for process efficiency. The flow rate should not exceed 50g/60s, as excessive flow resistance can lead to particle agglomeration and blockages within the converging-diverging (de Laval) nozzle [119];
- Deformation Characteristics: Ideally, feedstock powders should exhibit a low melting point and high deformability. However, brittle particles inherently have high melting points and limited plasticity, making them less adaptable to cold spray deposition [119];
- Size Reduction & Agglomeration: To mitigate brittleness, it is possible to reduce particle size significantly (down to the nanometre scale) and subsequently agglomerate them into larger structures. This approach minimises cracking upon impact and facilitates the brittle-

to-ductile transition, attributed to localised inelastic deformation occurring along slip systems and shear localisation at their intersections [81];

- Porous Agglomerates: the formation of porous agglomerates is recommended to improve material build-up, as these structures enhance particle flattening upon impact [92];
- Particle Morphology: Irregularly shaped particles are preferred, as the shape of the particle significantly affects the velocity of the particle. The decrease in particle shape sphericity leads to an increase in their velocity and ultimately reduces the coating's porosity (by improving packing density and inter-particle adhesion) [66,85].

The development and optimisation of commercially available powders for kinetic deposition have been ongoing for several years. Initial studies on brittle particle deposition revealed that, rather than forming a coating, the substrate is being eroded. This phenomenon led to early research on powder agglomeration, aimed at enhancing deposition efficiency. There are three primary approaches to modifying feedstock powders for kinetic deposition:

- Bottom-Up Synthesis: Powders are engineered from scratch, which allows for precise control over properties such as crystallinity, morphology, and particle size distribution. This method is widely regarded as the most versatile and effective strategy [120–122];
- Post-Synthesis Modification: Existing commercial powders are modified through binder addition, improving particle cohesion during deposition [123];
- Hybrid Approaches: Brittle powders are mixed with malleable particles to enhance deformability and facilitate better deposition [124,125].

Among these methods, the bottom-up synthesis offers the most diverse choice, enabling the customization of the crystallinity of the powder, and the size and morphology of the particles, which can be afterwards agglomerated into larger structures [26]. One of the most effective techniques within this category is the sol-gel method, which not only provides morphological control but also enables doping to enhance functional properties [126].

2.4.2 Sol-gel synthesis of the TiO_2 powder

The sol-gel process is one of the most widely used synthesis methods for producing oxide materials. Materials derived through this route exhibit high homogeneity due to the ability of the process to form solid-state materials from chemically uniform precursors [126]. The general idea of the process is to transition from the liquid precursors to a sol (a stable suspension of colloidal solid particles in a liquid phase) and ultimately to a solid network structure, i.e. gel (a porous three-dimensional inter-connected solid network). The sol-gel process starts from the hydrolysis of metal alkoxide precursors or metal salts, leading to a sol. Afterwards, the hydroxyl groups, react through the condensation process and give rise to the oxide network, a gel [127]. Before the gelation process ends, the obtained sol is subjected to the ageing process, during which the ceramic product's final form is determined. Both the synthesis conditions and subsequent steps after ageing influence the final shape and properties of the material. Depending on the requirements, the sol-gel method enables the fabrication of ceramics in various forms, including powders, coatings, fibres, membranes, monolithic ceramics/glasses, and aerogels with customised properties [128].

The sol-gel process starts with precursors containing a central metal element surrounded by non-metallic ligands. Depending on the type of metal precursor, the sol-gel process is based either on the metal-organic precursors or inorganic precursors. The synthesis involving the metal-organic precursors uses alkoxide precursors such as titanium ethoxide, titanium isopropoxide, or titanium butoxide, whereas inorganic-salts-based synthesis relies on such precursors like titanium tetrachloride or titanium trichloride [128]. The type of precursor (metal alkoxide or inorganic salt) significantly affects the process, particularly the hydrolysis rate. In the case of hydrolysis of alkoxides, the rate of the hydrolysis can be determined (for example by tailoring the pH of the system) thereby enabling process control and the formation of a three-dimensional network via condensation. In contrast, in synthesis based on inorganic salt as a precursor, hydrolysis occurs rapidly, leading to a range of species forming simultaneously, making process control difficult. Such a process results in the generation of large precipitates that afterwards are broken apart into smaller aggregates.

Additionally, using the inorganic salt precursors may introduce residual contaminants from the precursor, such as sulfates, chlorides, or nitrates, and may require high temperatures for reaction completion [129]. Consequently, alkoxides are preferred when precise control and product homogeneity are essential [130], while water-based synthesis is more suitable for large-scale production due to its cost-effectiveness [126]. Henceforth only the titanium alkoxide precursors will be discussed since these precursors are used for obtaining the TiO_2 feedstock powder in the experimental part of this thesis.

Sol-gel method is a bottom-up synthesis method that enables the fabrication of homogeneous, functional nanomaterials through a sequence of controlled hydrolysis, condensation, and phase transition steps. Titanium alkoxide precursors are highly reactive due to the presence of highly electronegative -OR groups that stabilise the central Ti in its highest oxidation state. Upon contact with water, alkoxide groups are replaced by hydroxyl groups. This reaction is accompanied by polycondensation, leading to the formation of an oxide network (Fig. 2.4.1) [131].

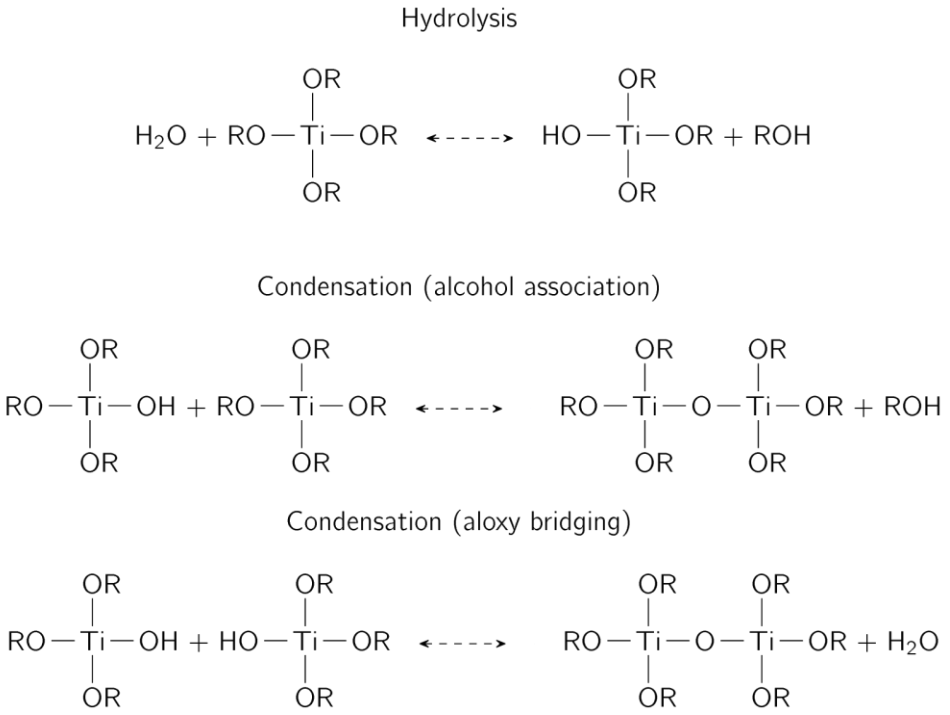

Fig. 2.4.1 Schematic representation of the chemical reactions present in a sol-gel process (using the Ti metal-organic precursors). Based on the [131].

Tetravalent metals, such as Ti (IV), depending on the pH, which can be determined by using a catalyst will form different complexes in the sol-gel process:

- in acidic pH aquo-hydroxo complexes ($M-(OH_2)$ or $M-OH$);
- in basic pH oxo-hydroxo complexes ($M=O$ or $M-OH$) [131].

Adjusting the pH to favour specific complexes enables precise control over the gel network structure, facilitating the formation of either cross-linked and branched polymeric chains or discrete spherical particles with minimal cross-linking [132]. This structural difference arises from the varying reactivities of aquo-hydroxo and oxo-hydroxo complexes. In acidic conditions due to the presence of aquo-hydroxo complexes reactions occur at the ends of chains. Under acidic conditions, excess H^+ ions protonate oxygen atoms bonded to metal centres, stabilizing these sites and directing condensation reactions predominantly to the ends of growing chains. While, in basic environments, the condensation happens across the entire structure (regardless of the location). In basic conditions the deprotonation enhances the nucleophilicity of these sites, permitting condensation reactions throughout the entire network (not just at chain ends) [131,133]. Additionally, complexes created via hydrolysis in acidic conditions are soluble which results in forming sol particles, that through the gelation process become a 3D network. The oxo-hydroxo complexes are insoluble and their presence often leads to the formation of polymeric structures or precipitates [131,133].

The molar ratio of water to titanium significantly influences the sol stability, as well as the size and morphology of created particles. Depending on the water and catalyst content, hydrolysis may proceed to completion (fully replacing -OR groups) or stop at a partially hydrolysed state [134]. When water is limited or present in stoichiometric proportions relative to titanium, hydrolysis and condensation can be controlled, yielding stable sols. Conversely, excess water promotes rapid hydrolysis and condensation, resulting in fast nucleation and particle growth. This rapid reaction also facilitates obtaining amorphous structures, as the material lacks sufficient time for long-range ordering [129,135].

In sol-gel synthesis, solvents play a crucial role in maintaining homogeneous reaction conditions by dissolving precursors and dispersing active components throughout

the solution. Each solvent can be characterised by properties such as boiling point, chain length, coordination behaviour, and polarity. Additionally, solvents are classified as protic if they can exchange protons and aprotic if they cannot. They may also be described as Brønsted acids when they donate a proton, in the case of proton acceptance the solvent is classified as Brønsted base [136]. These characteristics influence hydrolysis and condensation rates. Depending on the chosen solvent characteristics the hydrolysis and condensation have different rates [137]. Notably, alkoxide precursors do not mix with water, creating a two-phase mixture that prevents even hydrolysis. To overcome this, solvents like alcohols are added, as they dissolve both the alkoxide and water. This allows hydrolysis to occur uniformly throughout the solution, avoiding clumping and ensuring controlled reactions. It should be noted that the chosen alcohol is not only actively taking part in the synthesis, but also, is the intermediate product of the hydrolysis and condensation processes, which means it influences the synthesis process throughout its entire duration. Additionally, if an alcohol solvent containing alkoxy groups, differing from those in the precursor is introduced into the sol-gel process, at least partial substitution of these alkoxy groups occurs [131,138]. The created complexes' structure can be described in terms of either monomeric or oligomeric character. Monomeric structures will facilitate higher rates of reaction, in opposition to oligomeric structures in which the reactions are hampered due to their steric complexity. Therefore, one of the ways to determine the synthesised particle size is to tailor the alcohol solvent composition to the precursor structure: the synthesis with the larger portion of monomeric molecules will enable the production of the large, aggregated particles, while oligomeric molecules advantage will result in obtaining the monodispersed, fine particles [137]. The sol-gel synthesis can also be carried out using other types of solvents than alcohol, for example, ketones, which contrary to the protic, alcoholic solvents are aprotic. They differ primarily in the amount of hydroxyl groups they provide in the system. Protic solvents provide an external source of hydroxyl groups and are able to form hydrogen bonds and stabilize hydroxylated intermediates, increasing the concentration of hydroxyl groups in the system even more. Aprotic solvents, on the contrary, neither provide the additional amount of the hydroxyl group nor do they form stable bonds with them, which creates drastically different

synthesis conditions. As a result in the presence of an aprotic solvent, the condensation process proceeds faster and ultimately results in smaller, denser structures due to the rapid cross-linking process [139,140]. Additionally, the amount of hydroxyl groups from the solvent affects also the photocatalytic properties of acquired materials. The amount of hydroxyl groups present at the surface of the photocatalyst can provide a higher capacity of oxygen absorption which ultimately enhances the ROS generation process, facilitating a more efficient photocatalytic process [141]. Lastly, solvent, apart from taking an active part in the synthesis process, also affects the synthesis outcome when it evaporates (e.g. when the gel/sol is dried). As a consequence, it can affect such properties as morphology and crystallization process [142].

Typically, after the sol is obtained, to ensure its homogeneity and the strength of the particles the ageing of the sol takes place. In precipitation-based synthesis, ageing involves continuous sol mixing for a predetermined period [129]. The time of ageing affects the crystallinity of the material, following the rule: the longer the ageing time, the higher the structure order. This time also determines the particle size and the strength of the agglomerates, both of which increase with extended ageing time [143].

2.5 Tests for photocatalytic process evaluation (for coating photocatalysts)

Efforts to adapt the photocatalytic process within the water treatment sector are driven by a range of different reasons. The environmental concerns (water pollution and scarcity) and social demands for green technologies (which would make them more efficient and safer) are the main concerns that this new technology aims to address. At its core, the idea is promising: the main material used for photocatalysts – TiO_2 is affordable and widely available, what is more, the very process is sustainable and environmentally benign. This propelled quite a dynamic development of the photocatalytic materials, while unfortunately the practical aspects of their application were overlooked. Causing the commercialisation and spread of this technology yet to be achieved. The delay in the new technology delivery is one aspect of the problem, however, there is also another side to it, caused by the non-standardized methodology used by the researchers when testing and developing the photocatalysts. Although usually omitted, standardised evaluation of the material properties is crucial and can be carried out through standard ISO testing, making it possible to compare materials of different origins [11].

2.5.1 ISO standards for ceramic semiconductors

When it comes to ISO testing of photocatalytic semiconductor materials, one can approach the subject from various perspectives: select the operation environment (aqueous or gas phase), define specific properties of the material (self-cleaning, decomposition efficiency, or antimicrobial), or focus on creating the reactor in compliance with the standards (Fig. 2.5.1). So far, the researchers who wanted to conduct the standard test of the photocatalytic material in an aqueous environment had three norms to choose from: *Generation of active oxygen species* (ISO 10676:2010), *Dissolved oxygen consumption in a phenol solution* (ISO 19722:2017), and *Degradation of methylene blue* (ISO 10678:2010) and among them, the latter is the most commonly utilised.

In the beginning, the ISO 10678:2010 norm (Degradation of methylene blue) states its scope and limitations; it's a method for the determination of the immobilised photocatalyst surface' activity by the degradation of the methylene blue (MB) dye molecule in aqueous solution in

presence of the artificial UV light. The norm is not applicable for the photocatalyst properties evaluation in the visible light spectra. This is because using visible light irradiation causes direct photobleaching of the dye, which occurs simultaneously with its photocatalytic degradation. Consequently, this overlap makes it impossible to accurately assess the effectiveness of the photocatalyst [144].

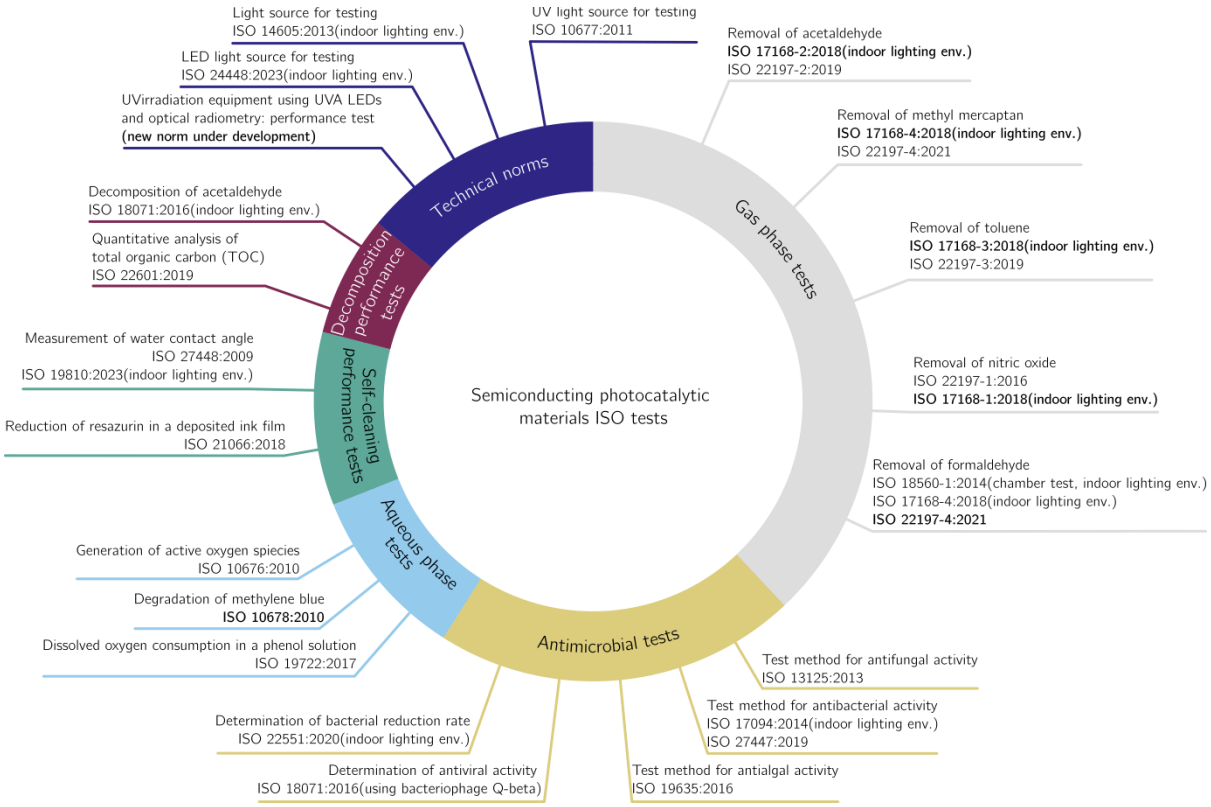

Fig. 2.5.1 Current state of the ISO norms concerning semiconducting photocatalytic materials. Norms highlighted in bold are either under development or in the process of the standard update. The illustration is based on the information gathered from [145].

The general apparatus needed to conduct the evaluation experiment is presented in Table 2.5.1, the model pollutant used in the experiment is the methylene blue (MB) dye. The needed equipment includes apparatus that enables mounting of the photocatalyst (reactors), the lamp that activates the photocatalyst (UV-radiation light source), the instrument that enables the characterisation of the mentioned lamp (UV radiometer – a sensor) and the device that monitors the degree of the photocatalytic decomposition through the dye solution absorption changes (UV/vis-spectrophotometer), along with the measurement cells which serve as the container for the dye solution when measured [144].

Table 2.5.1 Chosen apparatus and their properties specified in ISO 10678:2010 standard.

Element	Property
Reactors	Two testing cylinders fixed on the sample surface by a suitable glue or two testing cells, each consisting of a vessel with a sample holder.
UV-radiation light source	An emitter in the wavelength range between λ = <320, 400> nm (UV-A) with a UV-radiation intensity of E = 10 ± 0. W/m^2.
UV radiometer (sensor)	Calibrated to closely match the characteristics of the UV-radiation light source to measure its intensity.
UV/vis-spectrophotometer	Calibrated in the measuring range between λ = <600, 700> nm, for the determination of methylene blue solution concentration.
Measurement cells	Made of glass/plastics, with an optical length of 10 mm and a transmittance > 80 % (600 nm to 700 nm).

The ISO 10678:2010 standard experimental procedure starts with the preparation of the photocatalyst by exposing it to UVA irradiation for a period of time (between 24 and 72 hours). After cleaning, the conditioning of the photocatalyst takes place in the sealed reactor. The sample is submerged in the 35-ml solution of the MB dye (C_M = 20 ± 1 µmol/L), and it lasts for 12 hours in the darkness to achieve the adsorption-desorption equilibrium. After this period of time, if the concentration of the solution decreases by half (reaching a lower concentration than the test dye solution), the conditioning must be repeated with a freshly prepared solution; otherwise, 35 ml of the MB dye test solution (C_M = 10 ± 0.5 µmol/L) is added to the reactor replacing the conditioning solution. Once again, the reactor is sealed, but this time with the UV transparent glass pane. Then the reactor is irradiated with the UVA light for 3 hours; every 20 minutes it is supposed to be stirred, and its temperature should be equal to 23 ± 2°C. The height of the MB dye solution column is advised to be in the range of 2.0-5.0 cm (depending on the chosen reactor diameter). The degree of photobleaching is evaluated via a UV-vis spectrometer, either directly or by sampling and returning the solution after the measurement at 664 nm. The standard assumes the molar absorptivity of the dye to be 7.4×10^4 $M^{-1}cm^{-1}$ (at 664 nm), which allows for converting the substance absorption into

the solution concentration without the need to perform a standard curve for the methylene blue dye [144].

The standard's popularity undoubtedly stems from the simplicity of the used equipment, availability of used materials (MB dye dissolved in water), and simple assessment methodology. At the same time, the very same simplicity raises several concerns. That being said, the standard on its own is unlikely to produce reliable values of photocatalyst efficiency, which arises from a multitude of flawed assumptions and imprecisely defined equipment characteristics [146].

The first incorrect supposition is the premise that every MB dye is of the same purity, when in fact their purity varies and depends on their quality. Simultaneously, the quality of the dye influences its molar absorptivity, which determines values collected by the UV-vis spectrometer and results in their high variance [147,148]. According to the standard, the reaction solution is defined by its concentration. However, as mentioned, the quality of the dye can affect the molar absorption of the dye, leading to variations in the solution concentration. Furthermore, it also appears that the photocatalyst photonic efficiency depends on the initial MB concentration, which further emphasises the necessity of developing means to standardise and control the properties of the reaction solution [148]. This issue can be addressed by preparing the solution to a defined absorbance rather than a concentration, which, based on the standard, should amount to 0.74 [149].

The second inadequately defined aspect is the irradiation light source. Apart from given irradiance and limiting its light spectrum to UVA, there are no more guidelines to follow. This can lead to large differences between the laboratories which would purchase the irradiation source from different sources, and make it impossible to compare obtained results [148]. The solution to this problem would be to more precisely specify the source of irradiation, for example by limiting the irradiation bandwidth and stating its emission peak [149].

A further parameter, which was poorly considered in the standard, but at the same time has a significant influence on the process, is the pH of the dye solution. It is a fundamental principle that opposite charges attract each other, and such an instance takes place when

the pH solution value reaches above the point of zero charge (pzc) of the semiconductor (for the TiO_2 pzc = 6.6). The reduction in dye concentration is not the one that stems from the effectiveness of the semiconductor, but from the opposite electrostatic charge of the dye and photocatalyst surface [150]. This adsorption falsely increases the amount of dye that was removed from the solution. What is more, the complete dye decomposition follows equation (2.1), which will likely cause a reduction in the pH value. This, on the other hand, may lead to the reduction of the MB to the leucomethylene blue form, which is colourless and stable in the de-aerated solution (caused by insufficient stirring of the solution). Yet again, it distorts the results of the photocatalytic efficiency of the material. At the same time, both phenomena can be avoided by monitoring the pH of the dye solution and keeping it between the 5.0-6.6 pH range [149,151].

$$C_{16}H_{18}N_3SCl + 25\frac{1}{2}O_2 \xrightarrow{semiconductor} HCl + H_2SO_4 + 3HNO_3 + 16CO_2 + 6H_2O \qquad (2.1)$$

The double concentration of the conditioning solution also seems to lack justification. To prove this claim, firstly the primary objective of the conditioning step must be explained, which is to reach the adsorption-desorption equilibrium. The norm follows the procedure (Fig. 2.5.2) that starts with submerging the photocatalytic sample in the conditioning solution (dye's concentration $C_M = 20 \pm 1$ µmol/L). In these 12 hours, the difference between the dye's concentration on the sample's surface and the conditioning solution is evened, reaching equilibrium. However, the subsequent step, which involves replacing the conditioning solution with the test solution (half as concentrated as the conditioning solution), disrupts the obtained equilibrium. Consequently, the dye's molecules adsorbed to the sample's surface may relocate to balance the local variance in the dye concentration in order to satisfy the notion of the conditioning step. In other words, the established equilibrium is lost. To ensure the equilibrium between the separate conditioning stages the conditioning solution concentration and the reaction solution must match, enabling the observation of the photocatalytic process facilitated by the semiconductor [149].

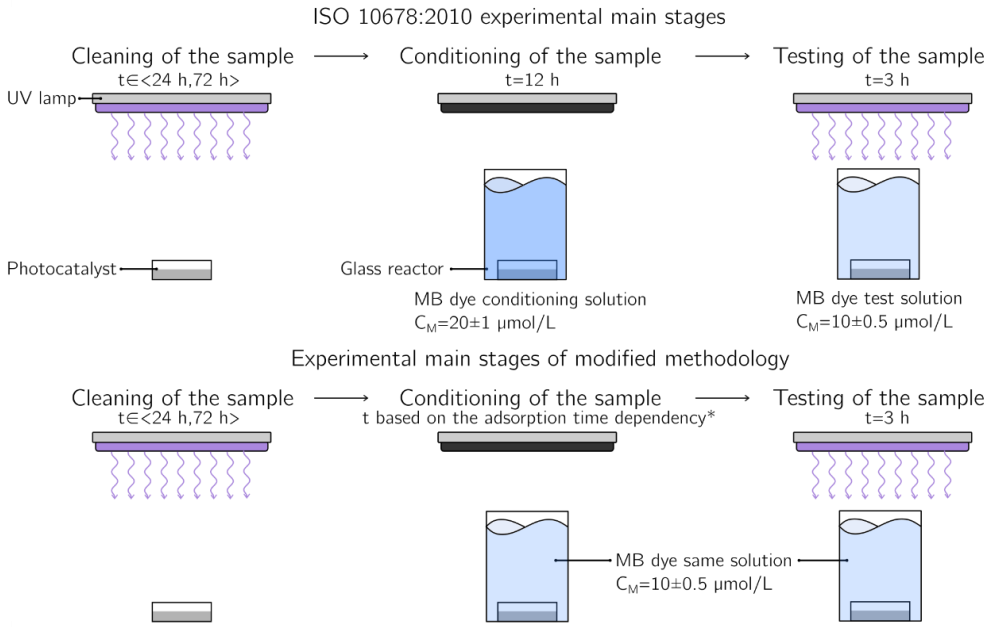

Fig. 2.5.2 the idea of the main stages of the photocatalyst properties evaluation based on the norm and based on the modified approach presented in the literature [149,153].* - in order to base the adsorption time of the sample one needs an additional experiment which enables setting the shortest time of the sample's adsorption, after which its influence is negligible.

The norm is surely needed to be able to standardise and compare the experimental results of different origins. This is why the norm ISO 10678:2010 should be applied, however its shortcomings should be properly addressed when used. This is why many researcher do not follow the standard but use it as a base for their own methodology [152]. Based on the literature presented in this Section, among the most significant changes that contribute to the credibility of the norm are:

- defining the MB dye solution not by its concentration (C_M = 10 ± 0.5 µmol/L), but by the absorbance (A=0.74), allowing better control over the initial MB dye concentration;
- providing a more elaborate characterisation of the light source, which includes the spectral characterisation of the lamp with its main emission peak specified, making it possible to assess the similarity of the equipment between the different laboratories;
- continuous observation and control of the pH of the MB dye solution to maintain its value in the range of 5.0-6.6 pH, which would prevent the dye electrostatic-driven adsorption and the reduction of the MB dye into colourless form, making the photocatalytic properties assessment more reliable;

- matching the concentration of the MB dye conditioning and test solution, by using the same solution for both stages, the time of the adsorption time should be customized for the specific material based on the experimental data that include its time vs adsorption characteristics.

When it comes to the evaluation of the results based on the ISO 10678:2010 standard, it involves several steps. They are composed mainly of the calculation of the degradation efficiency (based on the dye decomposition progress monitored via UV-vis spectrometer and described in Section 3.3.11.1) and kinetic analysis [144], the latter will be described more comprehensively in the next Section.

2.5.2 Kinetic aspect of semiconductor photocatalysis

The heterogeneous photocatalytic process, like the photocatalytic decomposition of the organic contaminant on which the ISO 10678:2010 is based, can be thoroughly described with the Langmuir-Hinshelwood (L-H) kinetics (eq. (2.2)). Thanks to its universality, this mechanism includes the description of such processes as photocatalytic decomposition of water pollutants including organic dyes like methylene blue and is widely utilized by researchers to evaluate the photocatalyst efficiency [154].

$$r = -\frac{dC}{dt} = \frac{k_r K C}{1 + KC} \tag{2.2}$$

r – the rate of the reaction,
C – concentration of the contaminant molecule in solution at any given time during degradation (mg/L),
k_r – limiting rate constant of reaction at maximum coverage under the given experimental conditions,
K – equilibrium constant for adsorption of the substrate onto the catalyst.

The L-H mechanism assumes a series of four steps systematising the heterogeneous catalytic reactions: (1) adsorption of the molecules on the photocatalyst surface; (2) dissociation of adsorbed molecules; (3) reaction of dissociated molecules to create products; and (4) desorption of products [155]. The first step facilitates the decomposition process by adsorbing the relevant species on the photocatalyst's surface. In this context, the 12-hour conditioning

period in darkness, during which the sample reaches the adsorption-desorption equilibrium, significantly influences the sample efficiency estimation process. The conditioning time is pivotal given the difference in the progress of the adsorption and photocatalytic processes, with the former occurring faster. Consequently, considering that the processes progress in a sequence, the reaction rate can be estimated for each process. Considering the objective of photocatalyst application, the determination of efficiency rates should be attributed to photocatalysis, which takes place when the semiconductor is activated. The L-H mechanism includes contributions from both adsorption (represented by K) and photoreaction (represented by k) (2.2). However, once adsorption-desorption equilibrium is attained, if the sole variation concerns the concentration of the organic pollutant over time, the general photocatalytic degradation can be expressed as:

$$r = -\frac{dC}{dt} = k_n C^n \tag{2.3}$$

n – the reaction order, typically in the range of $0 \leq n \leq 2$.

when n=1 the equation (2.3) takes the form of the pseudo-first-order kinetic model, which rewritten to a linear form allows obtaining the value as the slope of a straight line of $ln(C_0/C_x)$ vs. t [155,156].

$$ln\left(\frac{C_0}{C_x}\right) = k_1 t \tag{2.4}$$

C_0 – the initial concentration of the pollutant,
C_x – the remaining concentration of the pollutant.

The pseudo-first-order kinetic model (2.4) allows for obtaining a high and reliable correlation coefficient when fitted to the experimentally acquired data. Additionally, taking into consideration recent studies involving the TiO_2-based photodegradation of the MB dye, which revealed that the reaction followed the pseudo-first-order kinetic model [155], the use of this model is sufficiently justified.

2.5.3 Tests for the photocatalysts' durability/longevity evaluation

The photocatalyst activity is typically evaluated through short-term tests that conclude within a few hours or upon complete pollutant decomposition. However, for potential commercial applications, it is not only the initial efficiency that matters but also the ability of the photocatalyst to retain its properties over prolonged periods of operation. Furthermore, there is currently no standardised protocol for assessing photocatalyst longevity or durability. Consequently, researchers have gradually developed their own methodologies to study long-term behaviour, generally by mimicking the operational conditions. In many cases, the efficiency is gauged based on model pollutant degradation, such as that of methylene blue [157]. In the literature, there are three primary approaches for evaluating photocatalyst longevity/durability:

1) Photocatalyst cycle testing, in which the sample undergoes repeated cycles of pollutant degradation followed by regeneration (e.g., washing or thermal treatment). Performance metrics, such as degradation rate, total removal efficiency, and regeneration efficiency, are monitored over successive cycles [152,158–160].
2) Continuous long-term testing, whereby the photocatalyst is subjected to sustained operational conditions in a continuous flow reactor, with performance metrics monitored throughout the experiment [161,162].
3) Accelerated ageing, in which the photocatalyst is exposed to intensified conditions (e.g., high UV intensity, elevated temperatures) for extended durations. Changes in structural integrity, surface chemistry, and photocatalytic activity are monitored to evaluate the ageing mechanisms [163–165].

The objective of these tests is to assess the effects of simulated operational conditions on the retention of photocatalytic performance and structural integrity, as well as to understand the ageing mechanisms at play. This knowledge is critical for developing strategies to enhance the longevity of photocatalysts. Notably, although there is a substantial body of research on photocatalytic processes, only a few studies have addressed photocatalyst longevity; when

durability data are presented, the efficiency is either maintained or only slightly decreases over the test duration [157].

3 Experimental procedure: powder synthesis, coatings spraying, characterizations and evaluation of their performances

3.1 Powders preparation

The feedstock powders (FP) necessary to obtain the LPCS coatings are produced using the sol-gel method, which allows for the production of homogeneous, amorphous TiO_2 powders. The initial TiO_2 FP (called TiO_2-0 powder) synthesis process is determined experimentally on the previous work of the team [26]. Due to the low temperature of the synthesis and room temperature drying process, powder naturally agglomerates and is compatible with the LPCS deposition process. In addition to the production of TiO_2 initial feedstock powder according to the procedure developed by the team [26], a number of modified syntheses are carried out. The modifications are performed to study the influence of the solvent in the synthesis process on the TiO_2 powder's morphology [142]. With this in mind, when synthesising the TiO_2 feedstock powder, the solvent varied between methanol, isopropanol, and acetone.

3.1.1 Chemical reagents

The syntheses described and presented in the experimental part of the thesis are performed using the following reagents:

Table 3.1.1 Chemical reagents used for preparation and evaluation of the samples.

Substance (concentration)	Chemical formula	Manufacturer
Methanol (100.0%)	CH_3OH	CHEMPUR
Isopropanol (100.0%)	C_3H_7OH	P.P.H. "STANLAB" Sp. z o.o.
Acetone (100.0%)	$(CH_3)_2CO$	P.P.H. "STANLAB" Sp. z o.o.
Ammonia water (25.0%)	NH_4OH	P.P.H. "STANLAB" Sp. z o.o.
Titanium (IV) isopropoxide (97.0%)	$Ti[OCH(CH_3)_2]_4$	Sigma-Aldrich

3.1.2 Sol-gel synthesis of initial TiO_2-0 powder

The sol-gel method is used specifically to synthesise the TiO_2 powder in an amorphous state. The initial TiO_2-0 powder synthesis started by measuring out all the reagents in accordance with the proportions outlined in Table 3.1.2. All reagents are combined under a fume hood. The mixing process of the reagents is facilitated by a magnetic stirrer. At first, water, which played the role of both solvent and reactant and another solvent (isopropanol) is poured into a flat-bottomed plastic flask. Next, the pH of the mixture is increased to a pH value of ≈11 by adding a catalyst (ammonia water). The last step is to dropwise add the metal-organic precursor (TTIP) into the turbulently stirred solution. The resulting sol is stirred for 2 hours and subsequently dried at room temperature.

Table 3.1.2 Reagents and the volume proportions employed in the synthesis of the non-modified TiO_2 powders.

series	isopropanol (ml)	water (ml)	ammonia water (ml)	TTIP* (ml)
TiO_2-0	105	17.5	10	22.5

*-added dropwise when stirred

3.1.3 Sol-gel synthesis of the TiO_2 powder using different solvents

The solvent choice is among the factors that can influence the agglomeration process, especially when the agglomerates are formed naturally, without any external intervention. The solvent properties impact both the rate of synthesis (and consequently, particle size) and the self-organization time after synthesis (affecting agglomerate size) [166]. To assess the influence of solvent choice on powder agglomeration three solvents are chosen: methanol, isopropanol, and acetone. In order to maintain similar synthesis conditions, the amount of solvent used is calculated in moles (based on the proportions of the reagents used in the synthesis of the initial TiO_2 powder). This allowed for maintaining consistency among the planned three syntheses. Additionally, to inhibit the TiO_2 crystallisation process and obtain amorphous particles, the pH of the synthesis is elevated to 12 by adding a higher amount of ammonia water [167]. The calculated proportions of the reagents are presented in

the table (Table 3.1.3). The sequence of adding reagents remains unaltered; after the droplet addition of the metal-organic precursor, each solution is mixed for two hours. Subsequently, the powders are air-dried at ambient temperature.

Table 3.1.3 Reagents and the proportions employed in the synthesis of the TiO_2 powders using different reaction media.

series	solvent type -	solvent volume (ml)	solvent number of moles (mol)	water (ml)	ammonia water (ml)	TTIP* (ml)
TiO_2-IPOH	isopropanol	105	1.33	17.5	15	22.5
TiO_2-MOH	methanol	55.5	1.37	17.5	15	22.5
TiO_2-ACE	acetone	103.3	1.35	17.5	15	22.5

*-added dropwise when stirred

3.1.4 Sieving of the powders

After the TiO_2-0 powder is dried, it is subjected to the sieving process. The sieving aims to remove agglomerated particles larger than 63 µm since such a size is not recommended for the low-pressure cold spray process used for obtaining the coatings. Applying coarse powders leads to obtaining porous and rough coatings with lowered cohesion [81,92,168]. The sieve used for this process is compliant with the DIN ISO 3310 standard, the apertures are square-shaped with a side of 0.063 mm (Labindex, Warsaw, Poland), and the process is performed manually. As the powders TiO_2-IPOH, TiO_2-MOH, and TiO_2-ACE are modified to determine the effect of the synthesis on their agglomeration, and ultimately on the LPCS deposition process, they are omitted from this procedure.

3.2 Coating deposition process

3.2.1 Low-pressure cold spraying (LPCS) of the coatings

The formation of the TiO_2 photocatalytic coatings on the substrate material is achieved via low-pressure cold spraying using the DYMET 413 unit (Obninsk Center for Powder Spraying, Obninsk, Russia), combined with the aerosol powder feeder RBG 1000 D (Palas GmbH, Karlsruhe, Germany, Fig. 3.2.1).

The aluminium alloy AW-1050A H14/H24 is selected as the substrate material, and for the spraying, plates with dimensions of 20×20×4 mm^3 are used. Prior to the spraying process, the substrate surface is degreased and grit-blasted with alumina powder (mesh 45). The spraying process is conducted with the use of a standard circular de Laval nozzle (with throat and outlet diameters of 2.5 and 5 mm). The feedstock powder is transported by an aerosol powder feeder to the beginning of the divergent part of the nozzle by silicon pipe (instead of the vibrating hopper supplied with the unit). The powder feeding rate is calculated as approximately 12.8 mg/s. Nitrogen pressurised to 0.1 MPa is used as the feedstock powder carrier gas and feeds powder radially into the de Laval nozzle. The movement of the spraying gun is performed by a manipulator (BZT Maschinenbau GmbH, Leopoldshöhe, Germany). When spraying, the air pressurised to 0.5 MPa and heated to 600°C is applied as a working gas. The stand-off distance between the nozzle and the substrate material is constant and equal to 10 mm.

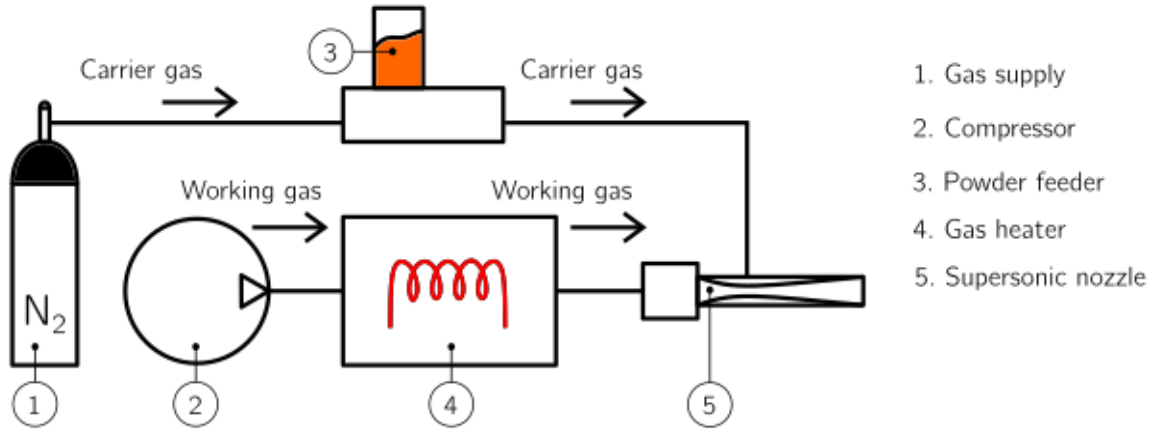

Fig. 3.2.1 the schematic arrangement of the LPCS system used for the photocatalytic sample spraying.

3.3 The characterization techniques and methodologies

In the experimental part of the thesis, in the first Section that concerns the characteristics of the coatings – Section 4.2.1 – the presented average results concern a smaller number of samples for specific sample type in contrast to the following Sections - Section 4.2.2 and Section 4.2.3 where the number is increased. Therefore, results between these specific Sections may differ due to the difference in the results accuracy. The relevant results for the referencing

samples (i.e. sample 0 and A) where obtained using new set of samples (not using the samples for the Section 4.2.1).

3.3.1 Laser Diffraction

The laser diffraction technique is used to determine the particle size distribution (PSD) of the synthesised powders. The characterisation is carried out using the HELOS BR R4 + RODOS laser diffraction system (Sympatec GmbH, Germany). The powder is delivered to the diffraction unit via a VIBRI dispersion unit (Sympatec GmbH, Germany) using an 80% feed rate, a 0.5 mm gap width, and a 190 mbar vacuum. Then, the powder is fed to the detector window using a 2-bar dispersal pressure. PSD statistics analysis is done in PAQXOS 3.1 software (Sympatec GmbH, Germany). The ISO 13320-1 standard is applied to calculate the $q_3(x_m)$ – fractional volumetric distribution density function and the $Q3(x_o)$ – cumulative volumetric distribution function of the powder samples, where x_m is the average particle size for the measurement class and x_o is the upper-end particle size of the measurement class. Volume median diameters x_{10}, x_{50} and x_{90} are also calculated. These values quantify the spread of particle sizes in a powder sample by volume, giving information about the size of fine (x_{10}), medium (x_{50}) and coarser particle sizes (x_{90}). The span of the examined powders is determined according to the equation (3.1) to provide a general measure of the total width of the distribution.

$$Span = \frac{x_{90} - x_{10}}{x_{50}} \tag{3.1}$$

3.3.2 Scanning electron microscopy (SEM)

Observation of the powders and the coatings are performed using a Scanning Electron Microscope (Hitachi S-3400 N, Tokyo, Japan) equipped with Secondary Electrons (SE), Backscattered Electrons (BSE) detectors, and EDX system for elemental analysis if needed. The powder specimens are mounted on a metal base using a sticky carbon disc and subjected to carbon-coating prior to the observations for increased material conductivity. The metallographic specimens are prepared by cutting the sample in the middle of its length.

The samples' cross-sections are immersed in epoxy resin and afterwards, ground using sandpaper with grit sizes of 180, 320, 600, 1200, and 2500, and then polished with diamond suspensions containing particles of 3 µm and 1 µm, without etching.

3.3.3 Raman spectroscopy

To study the chemical composition of the samples, Raman spectroscopy analysis is carried out using the Raman spectrophotometer LabRam HR800 (Horiba Jobin-Yvon, Japan). Each spectrum is recorded at room temperature with an Ar^+ laser (λ = 514.55 nm) as an excitation source. At least five measurements in different sample Areas are made on the surface of each sample.

3.3.4 Powder X-ray diffraction (XRD)

X-ray diffraction (XRD) patterns of the samples are recorded on an X-ray diffractometer Ultima IV (Rigaku, Japan), with the CuKα anode serving as the irradiation source (λ = 1.54056 Å). The XRD patterns are collected in the range of the Bragg angles 2Θ from 10° to 80°, a step of 0.05°, and an exposure time of 3 s per point. All samples are measured at an ambient temperature.

3.3.5 Evaluation of the crystallinity of the samples' structure (AMORPH statistical program)

The recorded diffractograms of the samples are further analysed in terms of the samples' crystallinity. The acquired XRD patterns are characterised by the AMORPH statistical program [169]. The program utilises a Bayesian statistical approach, which allows for the interpretation of both amorphous and crystalline structures. The program automatically sets the background, amorphous (A_{pa}), and crystalline (C_{pa}) components in the material and, as a result, calculates a fraction of the amorphous component for each posterior sample. At the same time, measured degree of crystallinity (DOC) is determined from the relationship described in equation (3.2).

$$DOC\% = C_{pa}/(A_{pa} + C_{pa}) \times \mathbf{100} \tag{3.2}$$

$DOC - the$ measured degree of crystallinity
$C_{pa} - the$ integrated peak areas for the crystalline component
$A_{pa} - the$ integrated peak areas for the amorphous component

The sample's crystallinity is determined by analysing at least 2 diffractograms from different samples of the same type and calculating the average from the obtained data. In the case of the longevity study the sample size is increased to 5. The estimations concerned only the chemically homogeneous TiO_2 materials consisting of both amorphous and crystalline structures.

3.3.6 Scratch-test

Evaluating the mechanical properties of the LPCS TiO_2 coatings poses significant challenges due to their porosity, rather low thickness resulting from using ceramic FP, and the high difference between cohesive and adhesive strength. These features make known standard testing unsuitable. For instance, ASTM C633-13(2021): Standard Test Method for Adhesion or Cohesion Strength of Thermal Spray Coatings [170] specifies a minimum coating thickness of 380 µm, which in this case the LPCS TiO_2 coatings rarely achieve. Similarly, ISO 14916:2017: Thermal spraying — Determination of tensile adhesive strength [171] requires specific surface preparation that alters the as-sprayed state of LPCS coatings, which would make the testing conditions incomparable to the coatings' operational conditions, making the results inapplicable in real-world scenarios.

Moreover, the porosity of the LPCS TiO_2 coatings significantly influences their mechanical behaviour by weakening their cohesion. In such cases, standards designed for adhesive strength determination, such as ASTM C633-13(2021) [170], may primarily measure cohesive failure, due to the significant difference between the cohesion and adhesion strength, leading to ambiguous results.

Conversely, scratch testing, described in EN 1071-3:2005 [172], allows for testing coatings of various thicknesses and evaluates the material in its unaltered state. At the same time, this norm specifies that the roughness of the tested coatings should not exceed 0.5 µm. The LPCS TiO_2 coatings are likely to exceed this threshold due to inherent process characteristics. Such

roughness might result in underestimated scratch-test data, as higher Ra values could lead to premature or irregular failure modes that do not accurately represent the coating's cohesive or adhesive strength. However, in order to mimic the operational state of the photocatalyst, it is essential to preserve the coating's surface in its operationally relevant state; thus, no surface processing should occur before testing.

Considering the constraints of available testing options the scratch-testing is deemed to be most suitable and is chosen for the LPCS coatings evaluation. In the method, controlled forces are applied through a sharp indenter, simultaneously moving along previously defined traversing length and generating scratches that simulate operational stress. In practice, the researcher gains knowledge about forces that lead to distinct types of coating failure: cracking, chipping, and delamination. Knowing this, one can predict whether the coating will be able to withstand its working conditions.

The cohesion and adhesion values of the TiO_2 coatings are determined with a scratch tester (CSM Instruments, Micro-Scratch Tester, CSM Instruments, Peseux, Switzerland) at ambient temperature and pressure in the air. A Rockwell indenter (Graz, Austria) with a diameter of 100 µm (instead of the typical 200 µm) is equipped to cause more intense damage and observe critical loads sooner. The intended purpose of the coatings is to perform the photocatalytic process in a liquid medium, meaning that the TiO_2 coatings are likely to work under relatively low loads and in a non-aggressive environment. Hence the range of the examination starts with a 30 mN load and ends with 30 N (with a linearly increasing loading rate of 10 N/min and a speed of 4.5 mm/min). During the measurement, the normal force (F_N), friction coefficient (μ), and penetration depth (P_d) are recorded. Based on these parameters (F_N, μ, P_d) characteristic loads (L_c): L_{c1} – cracking of the coating; L_{c2} – penetration of the coating to the substrate in the middle of the scratch; along with the cohesion of the coatings and adhesion of the coatings to the substrate, are specified. The surface damage originating from the scratch tests was assessed with a polarised optical microscope that was part of the scratch tester unit. The sample's cohesion and adhesion are determined by analysing

at least 5 reports from different samples of the same type and calculating the average from the obtained data. Each scratch is at least 6 mm long.

3.3.7 Diffuse Reflectance Spectroscopy (DRS)

The bandgap energy values (E_g) of the TiO_2 coatings are examined with a UV-Vis spectrophotometer equipped with a 75-mm integrating sphere (Specord 210, Analytik Jena, Jena, Germany). The spectra are registered in the range of 200-800 nm with a Spectralon® as the reference material. The Kubelka-Munk function is used to convert the recorded reflectance (R) into the absorption coefficient ($F(R)$, (3.3)), and the Tauc's plot ($[F(R)h\nu]^{0.5}$ vs. $h\nu$) is drawn to determine the bandgap energy (E_g). The final values are determined based on the 6 different results for each sample type.

$$F(R) = \frac{(1-R)^2}{2R} \tag{3.3}$$

3.3.8 Contact profilometry

The surface roughness (R_a, R_z) of the TiO_2 coatings is measured using a profilometer (Form Talysurf 120 L, Taylor-Hobson, Leicester, United Kingdom). For the measurements, the diamond stylus with a radius of 5 µm is transversed in the contact mode. The measurement parameters used for the examinations are: a force of 0.75 mN and a speed of 1 mm/s along the tracing length Lt = 15 mm, with a cut-off filter λ_C = 2.5 mm. The sample's surface roughness parameters are determined by analysing at least 5 different results for each sample type.

3.3.9 The optical microscopy

To observe the macroscopic properties of the coatings' top surface the optical microscope is used. Examinations are performed at x10 magnification using a metallographic microscope BX53M (Olympus, Tokyo, Japan) equipped with an Olympus UC90 camera with a nominal resolution of 9 megapixels (MP) and a square pixel size of 3.69 × 3.69 µm.

3.3.10 Eddy current method

The thickness of the TiO_2 sprayed coatings is determined through a non-destructive eddy current technique. The measurements are conducted with a Leptoskop 2042 apparatus (Karl Deutsch, Wuppertal, Germany), and a probe dedicated to non-ferrous substrates is applied, considering that samples are deposited on an aluminium plate. The probe generates the electromagnetic fields that create electrical currents in the conductive material beneath the coating; changes in these currents are analysed to calculate thickness. Samples are measured at 9 different points distributed across the coating surface of each 20×20 mm^2 sample. In the Section 4.2.1 the presented average results are taken from two samples, for specific sample type, whereas in the following Sections - Section 4.2.2 and Section 4.2.3 the final result is determined by analysing at least 4 different samples of each type.

3.3.11 Setup for assessing photocatalytic characteristics

The self-made setup is designed for the photocatalytic properties assessment by the degradation of the MB dye in the presence of artificial UV light. The system is incorporated into the fumehood (Fig. 3.3.1), and the room temperature is controlled to be 21 ± 3°C. The selection of the photocatalytic process conduct parameters is carried out, considering the MB decomposition ISO 10678:2010 standard test flawed assumptions described in the previous Section 2.5.1, as well as the photocatalytic reaction kinetics depicted in (2.5.2).

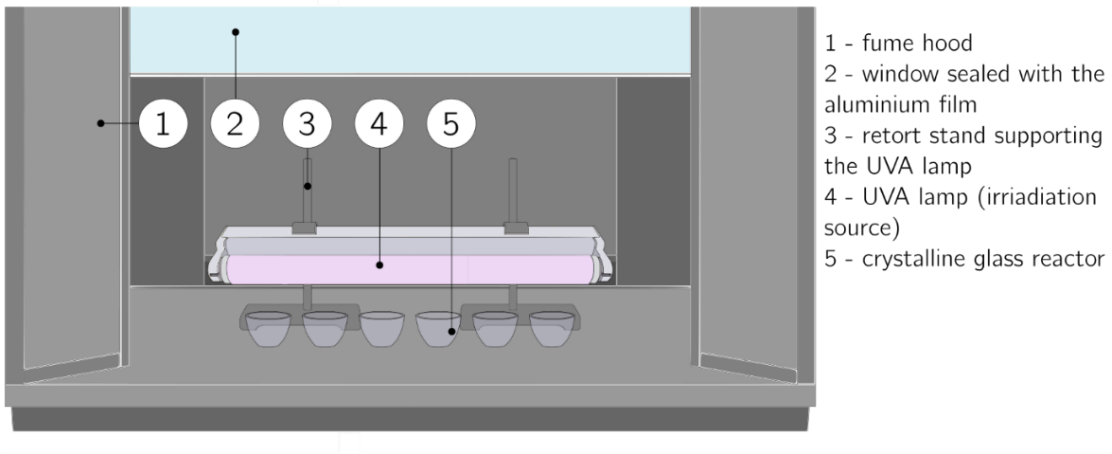

Fig. 3.3.1 the setup for assessing photocatalytic characteristics which is incorporated into the fumehood.

The setup is designed to fit a maximum of 6 glass reactors (UV-transparent glass), each with minimal inner diameter Φ=2.5 cm at the base and maximal inner diameter Φ=5.7 cm at its highest part (h=4 cm). Above the reactors, the UVA lamp is set using two retort stands. All reactors are arranged linearly along the radiation source since the UVA lamp bulb (model TL-K40W10R ACTINC) geometry is oblong. The lamp light spectrum, as well as the light intensity vs distance, is measured using a standard photodiode power sensor (S120VC, Thorlabs). The lamp characteristics are presented in Fig. 3.3.2. The lamp spectrum ranges from around 350 nm to 400 nm, with the maximum irradiance at 370 nm, a stabilisation time of 30 min is included prior to the irradiation process, for the lamp to reach a steady power output.

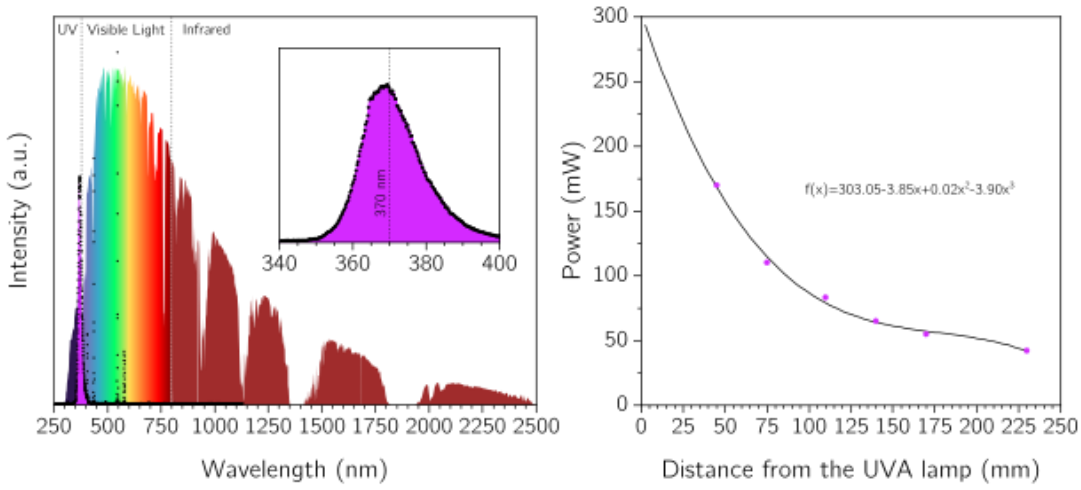

Fig. 3.3.2 On the left, the spectrum of the UVA lamp is plotted in the violet, the solar light spectra plotted in the background; and on the right, the powder output according to the distance from the UVA lamp.

The distance between each reactor and the UVA lamp is 75 mm long, which amounts to 110 mW. The surface/volume ratio of TiO_2 coating to MB dye is set experimentally to be 20x20 mm^2 and 30 ml respectively. The aim is to completely cover the sample in the dye solution, yet not create an excessively high MB dye solution column above the sample which would be an obstacle to the UVA irradiation needed to activate the sample. In this specific arrangement, the height of the MB dye solution column is around 18 mm (Fig. 3.3.6).

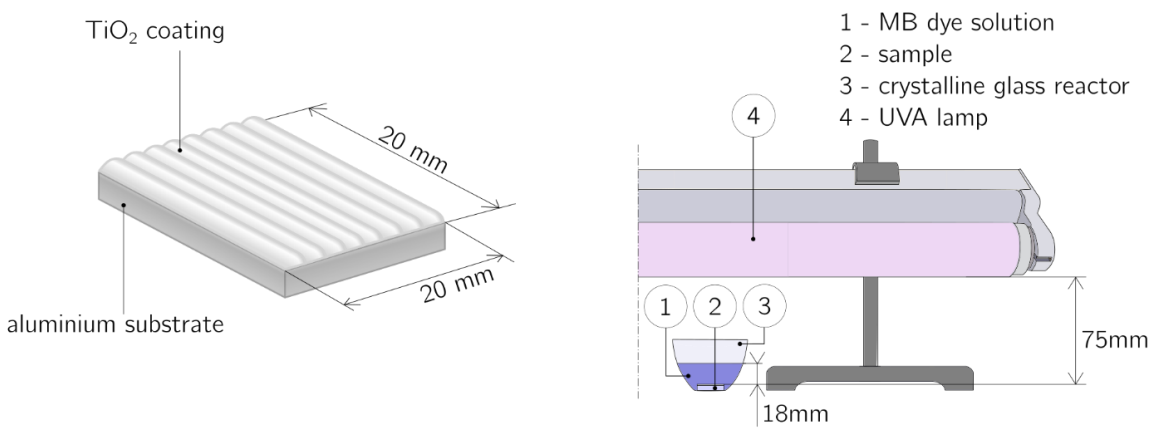

Fig. 3.3.3 Schematic representations of the LPCS-sprayed TiO_2 photocatalyst (on the left), the setup for assessing photocatalytic properties with key dimensions (on the right).

3.3.11.1 Methylene blue dye and its solution control

The preparation of the MB dye solution is always carried out the day before the test and consists of dissolving the methylene blue microscopic dye (POCH S.A.) in distilled water. The dye concentration used for all the experiments was $C_M = 1$ µmol/L. The extent of MB degradation in the solution is quantitatively estimated with a UV/VIS spectrophotometer (UV-VIS Nicolet Evolution 100, Thermo Lab) by analysing the change in the MB absorbance peak at 663 nm (Fig. 3.3.4, left).

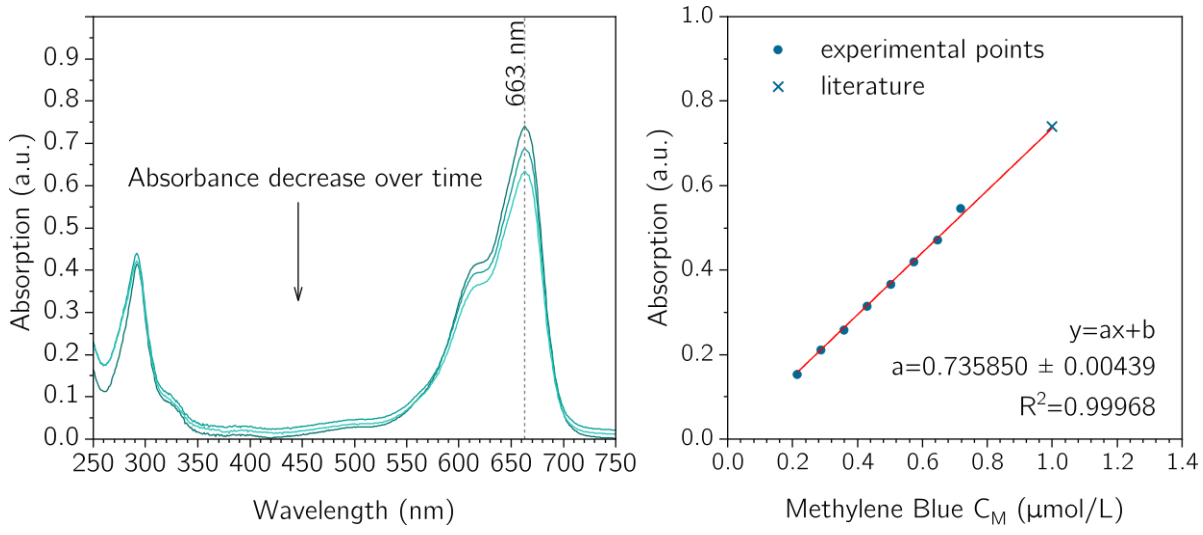

Fig. 3.3.4 On the left, are exemplary results of the methylene blue dye solution adsorption; on the right, is the calibration curve for the used methylene blue dye, the reference point is taken from [149].

The measurement glass cells which served as the containers for the dye solution are characterised by an optical length of 10 mm and transmittance (>80%). Additionally, to make

sure that the quality of the dye is satisfactory the calibration curve is done separately (Fig. 3.3.4, right).

Based on the premises presented in Section ISO standards for ceramic semiconductors, both the temperature and the pH of the methylene dye solution are monitored. After collecting the data mean values are presented in Fig. 3.3.5. According to the literature the temperature should be in the range of 23 ± 2°C, on the other hand, pH is advised to be in the range of 5.0-6.6 pH. In both cases (temperature and pH) there is an observable increase, however, none of the values is out of the limit and the criteria are met.

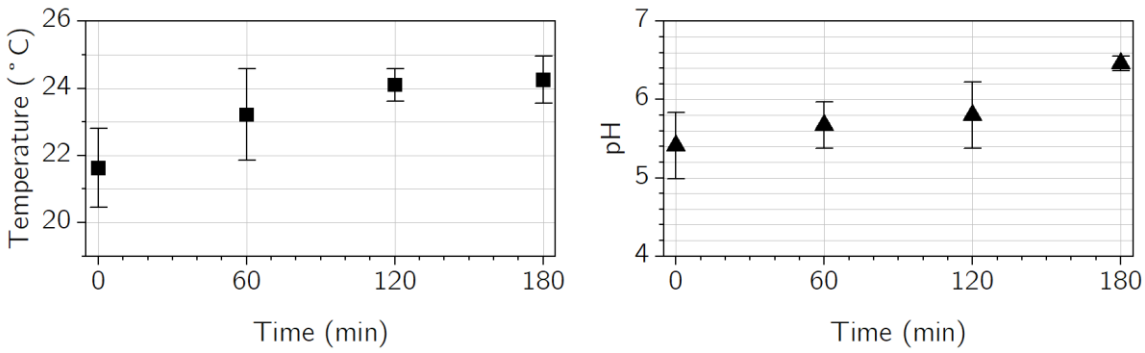

Fig. 3.3.5. The mean results of randomly selected 7 experiments where the temperature (on the left) and pH (on the right) are recorded over time of the photocatalytic degradation. The error bars stand for the standard deviation.

3.3.11.2 Methodology of the coatings' photocatalytic properties assessment

Firstly, all tested samples are subjected to at least 24-h UVA exposure to clean the samples' surface. The photocatalytic properties assessment process is modified and split into two parts: (I) dark to reach adsorption-desorption equilibrium (also referred to as the conditioning time); (II) photocatalysis in which each reactor was exposed to UVA radiation.

Additionally, as the literature states using two solutions of different concentrations leads to a loss of the equilibrium, this is why for the experiments only one solution of the MB dye is used. At first, the sample is conditioned in a solution with a concentration of C_M = 1 µmol/L and then used for photocatalytic decomposition. In order to allow one person to conduct the entire experiment, it is necessary to adopt a shorter conditioning time. The experiment is carried out to ascertain the dependence of the photocatalyst' adsorption on time and determine

the shortest time of the conditioning process. The experiment lasts for 24 hours in which the sample is submerged in the 30 ml MB dye solution, of concentration of C_M = 1 µmol/L. The degree of the dye adsorbed onto the sample's surface is estimated via UV-Vis measurements in the 30th, 60th, 90th, 120th, 180th, 240th and 1440th minute of the experiment. Afterwards, the dependency adsorption [%] versus time [min] is plotted in Fig. 3.3.6. Based on the acquired data the conditioning time is set to last 2 hours.

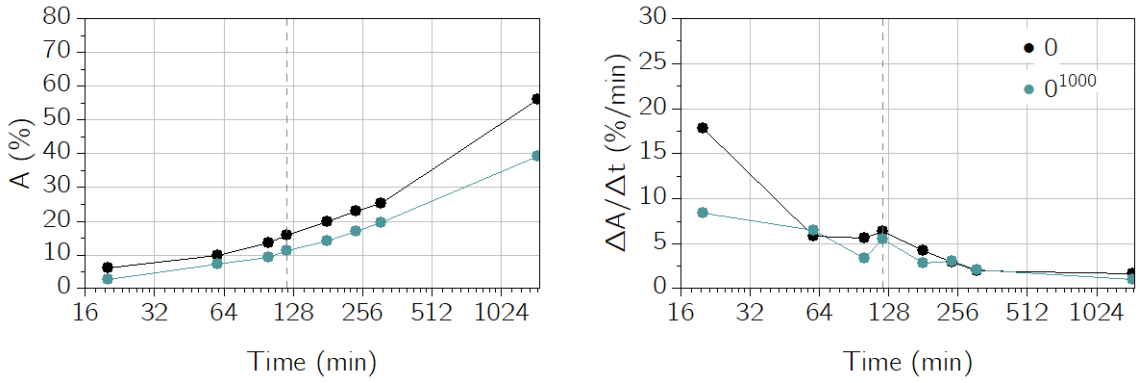

Fig. 3.3.6 Results of the 24-hour MB dye adsorption experiment. On the left: adsorption of the MB dye onto the surface of the different TiO_2 samples versus time. On the right, is the increase of the adsorption per time of the experiment. In both cases, the vertical dash line symbolizes the set conditioning time – 2 hours.

After the conditioning stage, the reactors are moved under the UVA lamp to perform the photocatalytic process. To control possible changes in MB concentration during UV irradiation, a reactor containing only MB reference solution (RS) is also subjected to the test and its concentration is observed as well. The absorbance values are converted into the dye concentration using the beforehand prepared calibration curve for the MB aqueous solution. The degradation efficiency (D) is calculated by the following equation (3.4):

$$D = \frac{C_x}{C_0} \times 100\% \tag{3.4}$$

Where C_x and C_0 (both in mg L^{-1}) are the initial and remaining concentration of MB in the solution, respectively, at any irradiation time (min). The kinetics of the photocatalytic decolourization rate of MB is determined using the Langmuir–Hinshelwood kinetics model, as given in the following equation (3.5):

$$\ln\left(\frac{C_0}{C_x}\right) = k_1 t \tag{3.5}$$

The pseudo-first-order rate constant (k_1) is calculated from the slope of the logarithmic plot of the concentration-dependent function described by equation (3.5) versus irradiation time (t). The final degradation efficiency and reaction rate constant are determined based on the results from at least 5 different samples of each type.

3.3.11.3 Evaluation of the coatings' structure stability

The LPCS coatings' structure stability is examined using the condensation humidity tests, in compliance with DIN 50017:1982 *Condensation water test atmospheres*. Throughout the test, a controlled atmosphere of 100% relative humidity and a temperature of 40 °C is maintained to allow condensation on the test samples. The exposure time of the samples to moisture was: 96, 192, 384, 768, and 1000 hours. To evaluate each type of coating, at least 5 samples underwent the experiment.

3.3.11.4 Evaluation of the recyclability/longevity of the coatings

The longevity of the LPCS coatings is evaluated by repetitive photocatalytic decomposition of the MB dye. Each photocatalytic process is done as described in the previous Section (3.3.11.2). The experiment is repeated four times per sample. In between the photocatalytic processes, the coatings are exposed to UVA radiation, at the same time, between the tests, the samples have one night of rest during which they are not subjected to any actions. Then the curves describing the MB decomposition vs time, per each photocatalytic process are prepared and stacked in one plot to present the difference between the cycles. To evaluate the one type of coatings, at least 5 samples underwent the experiment.

4 Results

4.1 TiO_2 powders characterisation

In this Section, the properties of the sol-gel-synthesised powders are discussed. Firstly, the initial powder TiO_2-0 is characterised, and afterwards, its modifications, TiO_2-IPOH, TiO_2-ACE and TiO_2-MOH are presented. The effect of the solvent used in the sol-gel process on the powders' properties is discussed, including LPCS-relevant properties (namely, particle size and self-agglomeration). Following this, the feasibility of powder application in the LPCS process is discussed.

4.1.1 Initial powder (TiO_2-0) characterisation

The sol-gel-derived initial TiO_2-0 XRD pattern and Raman spectrum are presented in Fig. 4.1.1. The initial powder is amorphous, and no distinct peaks are visible in the diffractogram. At the same time, the crystallisation process might have started, which is indicated by the broad hump around 30° 2θ [173]. The amorphicity of the structure is also visible in the Raman spectra of the powder, where broad, low-intensity bands are present [174].

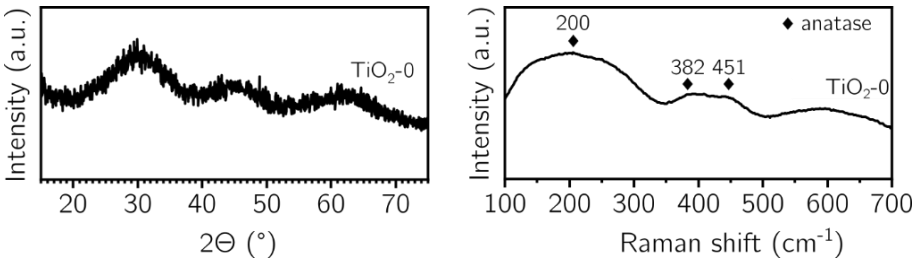

Fig. 4.1.1 On the left, there are diffractogram, and on the right, the Raman spectrum of the TiO2-0- as-synthesised powders.

The morphology of the as-synthesised TiO_2-0 and sieved TiO_2-063 powders is visible in Fig. 4.1.2. The size of the created structures is approximately a few tens of micrometres, which is consistent across both powders and remains unchanged after the sieving process. At higher magnification, the observable smallest particle size is around 500 nm. The powder particles form a complex structure formed out of two discernible particle types: round-shaped amorphous and sharp-edged particles, which might be crystalline. The crystalline particles are

enveloped by the smaller amorphous ones, resulting in irregular agglomerate formation. Structures resemble the sol-gel-derived TiO_2 powders reported in the literature [26].

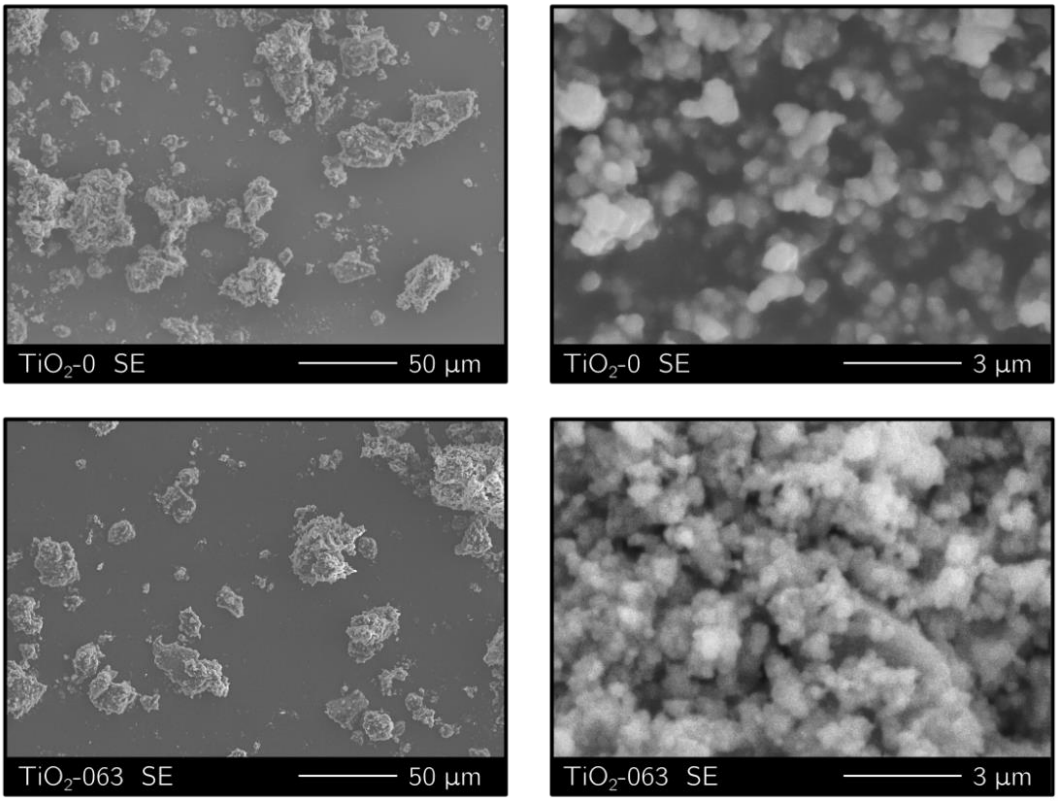

Fig. 4.1.2 the SEM-SE images of the TiO_2-0 initial (top row) powder and sieved TiO_2-063 powder (sieve 63 µm, bottom row); left column: magnification x500; right column: x10 000.

The TiO_2-0 initial powder particle size distribution (PSD) analysis shows a wide range of particle sizes: from 0.5 µm to 142.36 µm, the volume median particle size is 11.51 µm. The synthesised particles are characterised by bimodal granulometric distribution; the main visible fractions are centred around 2.5 µm and 50.0 µm, with the latter as a predominant share (Fig. 4.1.3). The bimodal distribution might be the result of the powder agglomeration since such large structures are not noticed in the SEM observations.

After the sieving process (powder denoted as TiO_2-063), the largest particles' size is reduced from 142.36 µm to 81.57 µm. A cutoff for particles larger than 63 µm, resulting from the sieving process, is successfully achieved. Similarly, the volume median particle size shifted towards smaller values: from 11.51 µm to 6.55 µm. The powder still presents a bimodal distribution; however, after the sieving process, the main fractions are centred around 2 µm and 40 µm.

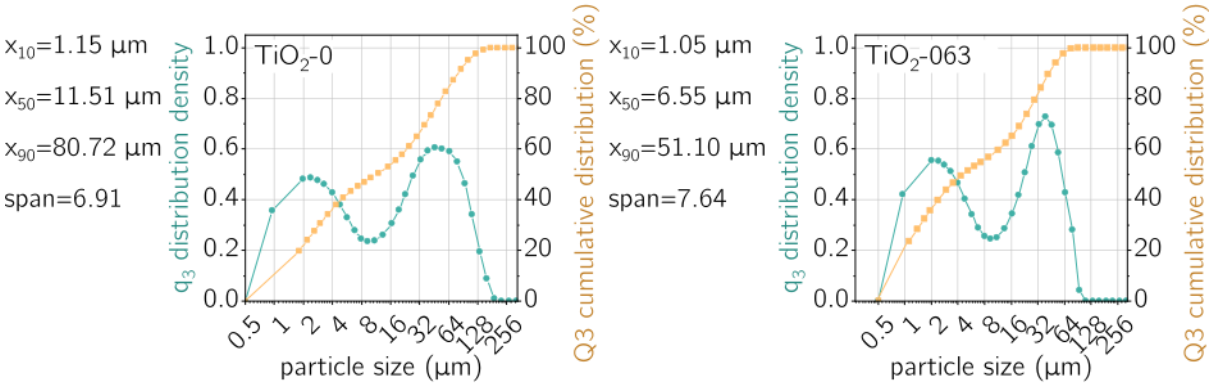

Fig. 4.1.3 Particle size distribution of the synthesised TiO_2 initial and sieved powders, where density (q3) and cumulative distribution (Q3) are presented. Each of the plots is characterised by the volume-weighted percentile particle diameters of the synthesised powders.

The TiO_2-0 powder agglomerated structure consists mainly of amorphous share, with the presence of the crystals evidenced in the SEM observations. Combined with the LPCS process, such a structure facilitates a more effective deposition process than the crystalline powders [122]. Additionally, the TiO_2-063 powder after the sieving particle size range is within the range of the granulometry recommended for the LPCS workstation [175].

Summary

The sol-gel synthesis of the TiO_2-0 powder yields an amorphous, self-agglomerating powder. The initial powder particles can be divided into two groups: round-shaped amorphous particles and sharp-edged particles, which might be crystalline, with the former being the dominant type. The initial powder exhibits a bimodal granulometric distribution, with the main fractions centred at 2.5 µm and 50.0 µm. The larger particles likely result from agglomeration of the primary particles, which constitute the first fraction. The irregular shape of the agglomerates might enhance their kinetic energy in the deposition process, making the coating less porous. Additionally, the sieving process effectively filters out particles larger than 63 µm, improving suitability for the LPCS process.

4.1.2 Solvent-modified powders (TiO_2-IPOH, TiO_2-ACE, TiO_2-MOH) characterisation

The powders synthesised using different solvents and a higher pH of 12 are all characterised by very similar diffraction patterns; no distinct peaks are visible that correspond to the presence of a crystalline phase, meaning that the powders are amorphous. All modified powders – TiO_2-IPOH (isopropanol), TiO_2-ACE (acetone) and TiO_2-MOH (methanol); have a visible broad hump characteristic for the amorphous structure present in their diffraction patterns (Fig. 4.1.4, left) [173]. The high amorphicity of the powders' structure is also recorded in the Raman spectra of the powders. The visible bands are faintly pronounced (low and broad) [189]. Between the three powders, there are no significant differences; therefore, the solvent change in the synthesis process does not significantly affect the powders' crystalline structure.

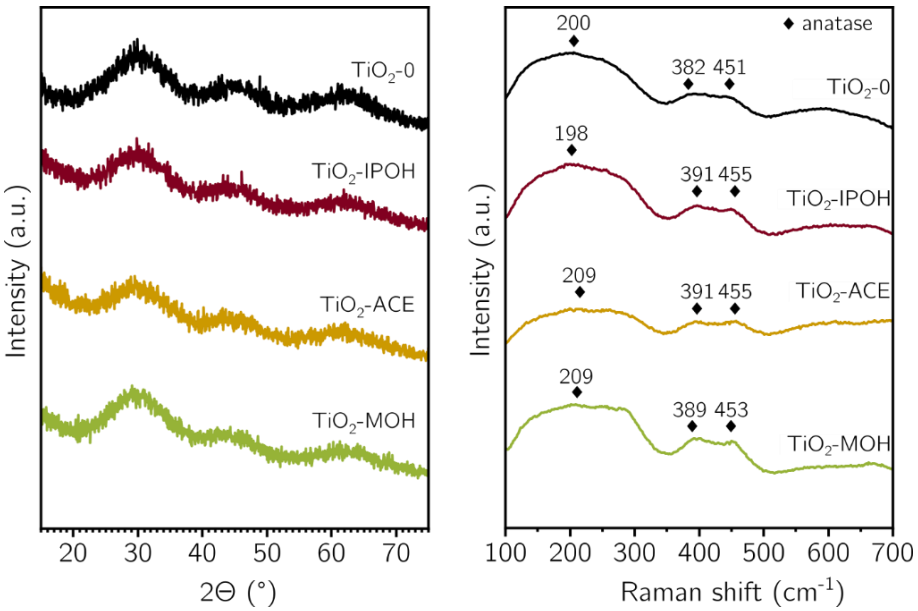

Fig. 4.1.4 On the left, there are diffractograms, and on the right, Raman spectra of the TiO2-0- as-synthesised and solvent-modified powders: TiO_2-IPOH, TiO_2-ACE, and TiO_2-MOH.

The morphology of the powders TiO_2-IPOH, TiO_2-ACE, and TiO_2-MOH are presented in Fig. 4.1.5. The most similar synthesis conditions, compared to the initial synthesis process, are used for obtaining the TiO_2-IPOH powder, where only the pH is increased. The TiO_2-IPOH powder morphology resembles the initial powder TiO_2-0 microstructure, consisting of sharp-edged grains and smaller, clustered particles, with the majority being the latter. The smallest

observable particles are around 300 nm. The TiO_2-ACE powder morphology is the most similar out of the three modified powders to the initial TiO_2-0 powder, the size of the smallest observable particles is around 500 nm, which makes them slightly larger than those observed for TiO_2-IPOH. The powder TiO_2-MOH has a similar microstructure to the TiO_2-IPOH powder; again, the smallest observable particles are around 300 nm. All powders are irregularly shaped, which is favourable for LPCS deposition [66].

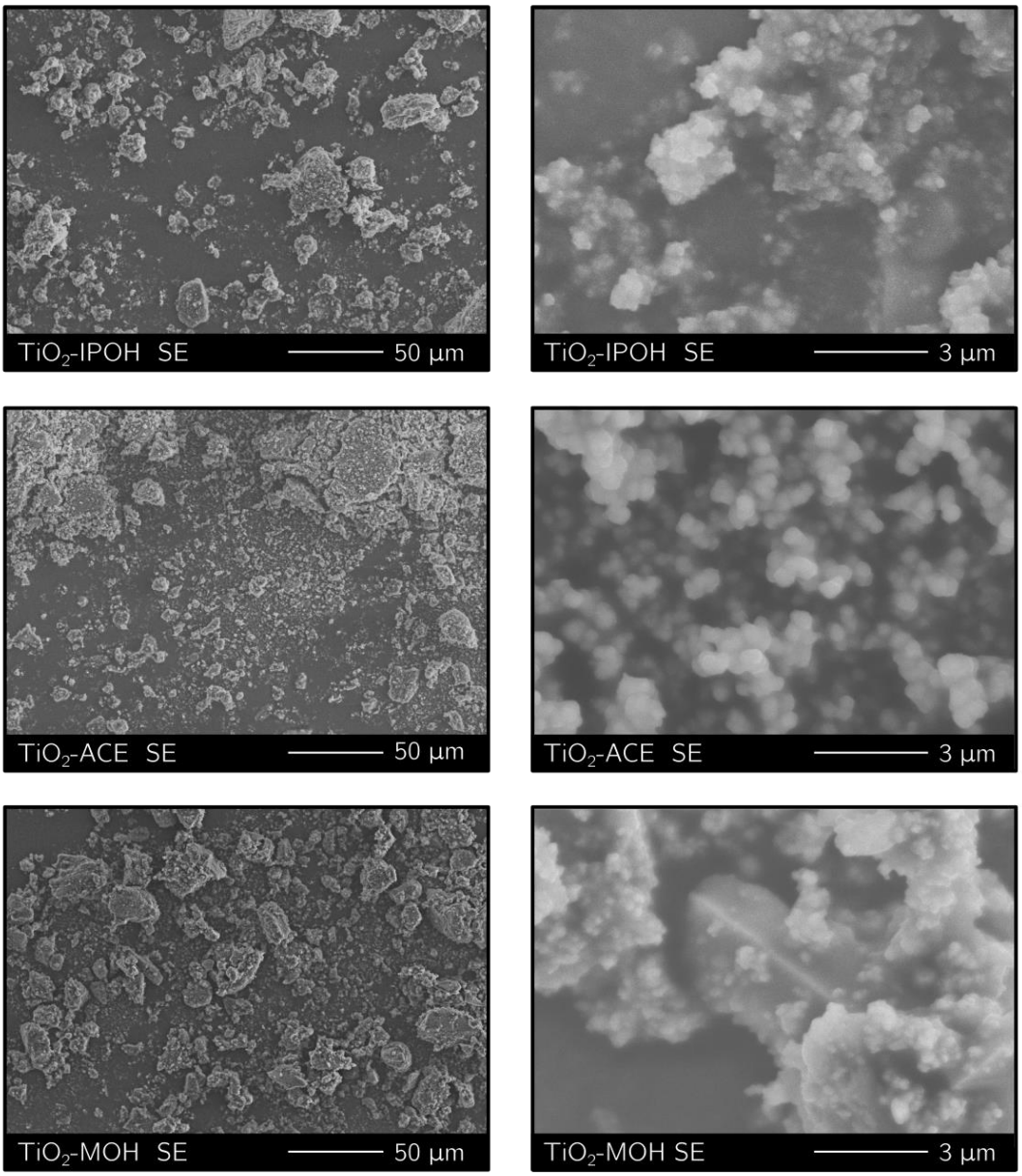

Fig. 4.1.5 the SEM images of the TiO_2 powders synthesised using different solvents are presented in: the top row, the TiO_2 IPOH powder; the middle row, the TiO_2-ACE powder; and the bottom row, the TiO_2-MOH powder, all in topographic contrast. Left column: magnification x500; right column: x10 000.

The modified powders have different PSD depending on the used solvent. The TiO_2-IPOH powder agglomerates' size shifted towards larger diameter values (Fig. 4.1.6, top, right); the TiO_2-IPOH powder particle size range starts at 0.5 µm and ends at 157.04 µm. The volume median particle size is 22.83 µm, which is two times more than for the initial powder and results from the agglomerate size increase. The bimodal granulometric distribution consists of two main shares, the first centred around 2 µm and the second around 64 µm. The powder consists of the majority of 64-µm agglomerates.

Compared with methanol, isopropanol produces more moderate hydrolysis and condensation rates due to its longer, branched alkyl chain, which introduces greater steric hindrance. The complexity of the structure of the solvent directly influences the size of the metal-alkoxide intermediates in the sol–gel process: longer, bulkier chains stabilise smaller clusters by impeding their aggregation and slowing the formation of new nuclei. Smaller alkoxide species react more rapidly, whereas larger species (such as those derived from isopropanol) slow down overall reaction rates and favour particle growth over nucleation [137]. Consequently, isopropanol-based syntheses yield larger, more aggregated TiO_2 particles compared to the finer powders obtained using lower-molecular-weight solvents.

The TiO_2-ACE powder, on the other hand, is characterised by the widest span value (Fig. 4.1.6 bottom, left), meaning that those particles are the least uniform in size out of all powders. The particle size distribution range starts at 0.5 µm and ends at 130.23 µm, which is quite similar to the initial TiO_2. The volume median particle size is 7.27, which is smaller than the value recorded for the initial powder, meaning that the shares of the two main fractions have changed for the acetone-based powder. The first fraction is centred around 2 µm, and the second, main one is around 64 µm, yet for this powder, their shares are almost equal, which shifted the volume median particle size towards smaller values. Those changes may be the result of the higher polarity of the acetone, as well as its lower boiling point and viscosity (Table 4.1.1), which increase the hydrolysis and condensation rates, making the nucleation faster and allowing many nanoparticles to form at the same time, causing them to attach to themselves and hinder their growth [137,166,176]. Additionally, a lower amount

of hydroxyl groups present in the synthesis (caused by using aprotic solvent, such as acetone) can also decrease agglomeration[177].

Table 4.1.1 Chosen solvents' physical properties [178].

Solvent type	Polarity index	Boiling point (°C)	Viscosity (cPoise)
isopropanol	3.9	82	2.30
acetone	5.1	56	0.32
methanol	5.1	65	0.60

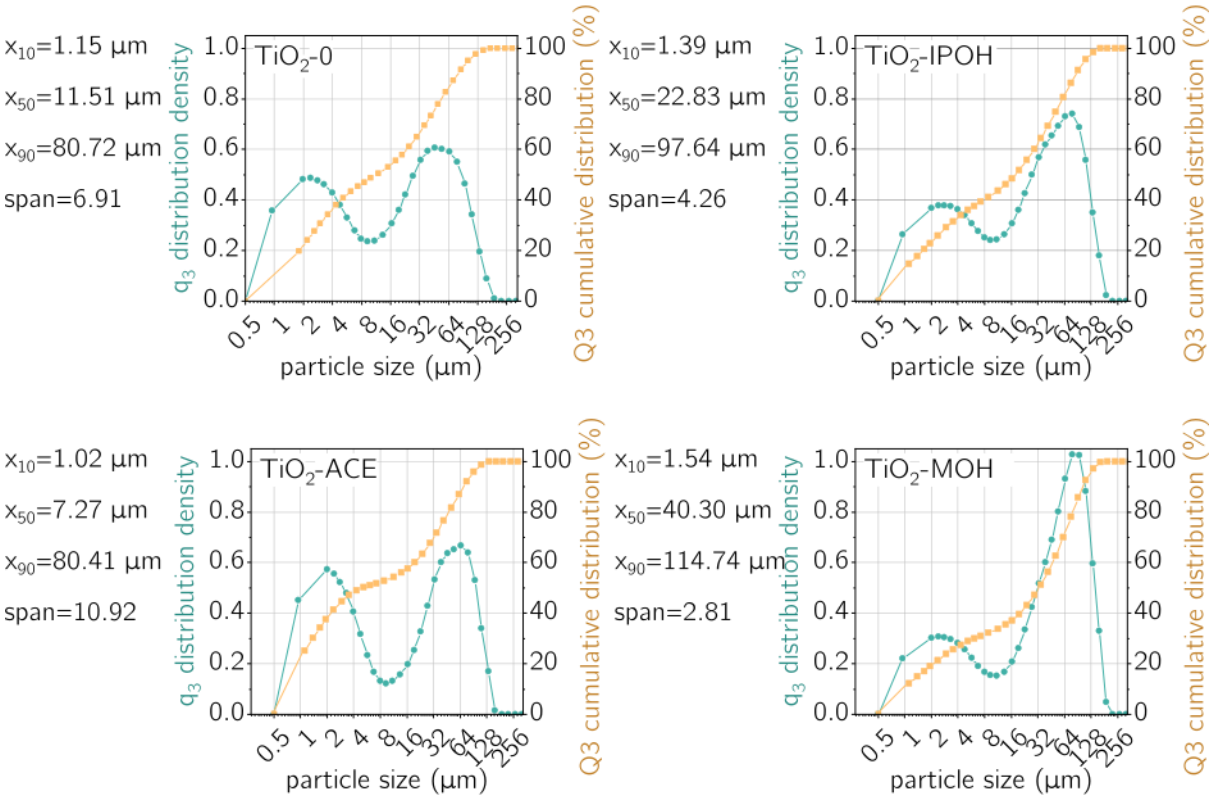

Fig. 4.1.6 Particle size distribution of the synthesised TiO_2 initial and solvent-modified powders, where density (q3) and cumulative distribution (Q3) are presented. Each of the plots is characterised by the volume-weighted percentile particle diameters of the synthesised powders.

A noteworthy change occurred in the PSD of the TiO_2-MOH powder, synthesised using methanol. The agglomerate's size shifted towards larger values, and the difference between the two main fractions' shares increased (Fig. 4.1.6 bottom, right). The size particle range starts at 0.5 µm and ends at 166.76 µm; the volume median particle size is 40.30 µm. The smaller fraction constitutes one-third of the main share and is centred around 2 µm, the main fraction

around 85 µm. Both acetone and methanol have the same polarity index, meaning that the particles should be approximately the same size. However, methanol is a source of additional hydroxyl groups in the synthesis and evaporates slower than acetone, which gives more time for the interaction between synthesised particles, ultimately creating the agglomerates [177,179].

The particle size has increased for the TiO_2-IPOH and TiO_2-MOH powders, while TiO_2-ACE is characterised by the reduced particle size. This change is likely due to the increased amount of the hydroxyl groups present in the alcohol-based syntheses, which aids the agglomeration process [177]. The modified powders also vary in their homogeneity; the most homogeneous is the TiO_2-MOH powder (characterised by the lowest particle size distribution span value), while the TiO_2-ACE powder is characterised by the least uniform particle size distribution. Compared to the typical cold-spraying particle size (5-100 µm [175]), the TiO_2-IPOH and TiO_2-MOH exceed the recommended range, which can result in lowering the particles' in-flight speed and impact energy, which ultimately can decrease the deposition efficiency and the coating's thickness mechanical properties.

Summary

The solvent-modified powders TiO_2-IPOH (isopropanol), TiO_2-ACE (acetone) and TiO_2-MOH (methanol) are characterised by similar amorphous structures and particle morphology, compared to the initial powder TiO_2-0. All modified powders exhibit a bimodal granulometric distribution, resembling the TiO_2-0 powder. The modified powder's size distribution changes depending on the solvent used. Synthesis based on isopropanol, which has a more complex structure and lower polarity, leads to a more moderate synthesis process compared to the rest of the used solvents. As a result, the TiO_2-IPOH powder particles are larger and more aggregated compared to TiO_2-ACE powder. As for the TiO_2-ACE powder, it is the result of faster hydrolysis and condensation processes due to its higher polarity and lower viscosity, resulting in a higher number of smaller particles. The TiO_2-MOH primary particles are similarly sized to those of TiO_2-ACE powder; however, likely due to the higher amount of hydroxyl groups present in the synthesis process, there are more agglomerates in methanol-

based powder. Due to the increased powder particle size in TiO_2-IPOH and TiO_2-MOH, the LPCS spraying efficiency might be reduced due to the lower kinetic energy of entrained particles.

4.2 TiO_2 LPCS coatings characterisation

This Section examines the chosen factors affecting the low-pressure cold-spraying of TiO_2 powders, which are traverse speed, number of layers, and scanning step. Following this, these factors influencing the TiO_2 photocatalytic coatings properties and long-term performance are also assessed. The investigation is divided into three Sections:

- The first Section explores the impact of LPCS process parameters on the structure, surface and mechanical properties of LPCS coatings;
- The second Section analyses the effect of the ageing process on the coating microstructure, ultimately affecting their mechanical stability and photocatalytic efficiency;
- The third Section investigates how the TiO_2 feedstock powder properties modification (mainly self-agglomeration) affects the LPCS process and obtained coating's properties.

By systematically addressing these aspects, this Section aims to provide a comprehensive understanding of how powder characteristics, deposition parameters, and post-processing conditions influence the functionality and durability of LPCS-deposited TiO_2 coatings.

The results and figures presented in these Sections are partly published in [78,180,181].

4.2.1 Influence of the LPCS parameters (scanning step, number of layers, traverse speed) on the TiO_2 coatings' structure and properties

the influence of low-pressure cold spraying (LPCS) parameters on the properties of photocatalytic coatings is investigated by systematically varying chosen process parameters, namely traverse speed, number of layers, and scanning step. The parameters examined in this study are summarised in Table 4.2.1. For all experiments, TiO_2-063 powder is used as the feedstock material to deposit photocatalytic coatings. Other critical LPCS parameters, including working gas temperature, gas pressure, carrier gas pressure, and stand-off distance remain constant at experimentally determined values to ensure controlled conditions. This Section builds upon previously published research [78], expanding on the effects of the LPCS parameters on the TiO_2 phase composition, coating morphology, and mechanical properties.

To ensure the strength of the LPCS coatings created in this study, the working gas temperature is set to the maximum operating value of 600°C, as higher temperatures improve deposition efficiency and coating strength for both metallic and oxide powders [95,122]. Another critical parameter is the working gas pressure. While higher working gas pressures facilitate particle deformation in ductile materials, they can lead to particle fragmentation and substrate erosion when using oxide powders [182]. Furthermore, the pressure influences the temperature drop in the divergent part of the nozzle, with higher initial pressures resulting in greater cooling. Thus, the working gas pressure is experimentally optimised and fixed at 0.5 MPa to maintain adequate thermal energy for deposition [112].

Table 4.2.1 Low-pressure cold spray parameters used to spray the TiO_2 coatings using the TiO_2-063 powder.

sample	0*	A	B	C	D	E
traverse speed [mm/s]	5	5	10	10	10	10
number of layers	1	1	1	2	2	1
scanning step [mm]	2	1	2	2	3	1
spraying time [s]	40	76	20	38	26	38
powder carrier gas pressure [MPa]	nitrogen, 0.1					
working gas pressure [MPa]	air, 0.5					
working gas temperature [°C]	600					
stand-off distance [mm]	10					
(*)- sample 0 is the reference sample sprayed with the initial LPCS spraying parameters.						

The carrier gas (nitrogen) with FP particles is delivered to the start of the divergent section of the de Laval nozzle through a silicon pipe (as described in Section 3.2.1). During this process, the pressure and temperature of the working gas decrease due to expansion. In such an arrangement, it is possible to use low pressures of the carrier gas [83], such as 0.1 MPa, as used here. Additionally, for the carrier gas, bottled nitrogen with low moisture content is chosen to ensure effective powder feeding and prevent moisture-related issues, which might disrupt the deposition process.

The stand-off distance determines the thermal and kinetic energy retained by the particles at impact, directly affecting deposition efficiency. Excessively short stand-off distances can significantly increase the effect of the bow shocks on the entrained particles, ultimately reducing their velocity and disrupting the deposition process. Conversely, overly long stand-off distances cause the reduction of the particle energy, lowering deposition efficiency [87]. For the TiO_2-063 powder, the optimal stand-off distance is experimentally determined to be 10 mm.

The phase structure of the LPCS samples (TiO_2 coatings sprayed on aluminium plates with varying parameters presented in Table 4.2.1) consists of a mixture of the amorphous-anatase phases (Fig. 4.2.1). The samples' XRD patterns show the presence of a crystalline phase; the visible peaks are located at 25.25°, 37.85°, 48.00°, 53.90°, 55.05° and 62.70° 2theta and can be attributed to the anatase crystalline structure. Moreover, in samples 0, B, C, and D, the characteristic broad hump can be observed around 25° 2theta, which indicates a substantial share of amorphous structure in the samples [26]. The additional peaks present in the sample D diffractogram (located at 38.40°, 44.40° and 64.40° 2theta) correspond to the aluminium phase. Their presence suggests that either the coating is extremely thin in some places, or it is not fully covering the substrate material. The structure of the sprayed coatings is confirmed by Raman spectroscopy; the characteristic bands of anatase located around 153, 398, 521, and 642 cm^{-1} are present for all measured samples [26].

The difference in the thermal energy used during the deposition process can be indirectly assessed by comparing the degree of crystallinity (DOC) of the sprayed coatings [21,183]; the results are presented in Fig. 4.2.1. The reference sample 0 exhibits a DOC of 14%, while sample A, deposited with the longest uninterrupted spraying time (76 s), achieves the highest DOC of 37%. Continuous spraying increases sample temperature due to the constant heat input, resulting in more effective crystallisation of the coating TiO_2 amorphous structure [184]. This trend is observable in other single-layer samples; for instance, sample B, deposited in 20 s (process time reduced by half compared to reference sample 0), exhibits a DOC of 14%. Sample E, deposited with a spraying time similar to sample 0 but with faster and denser nozzle

movement, achieves a slightly improved DOC of 16%. Interrupted processes (e.g., two-layer samples C and D) result in DOC values similar to the reference sample (16% and 12%, respectively). While sample C, sprayed with a 2 mm scanning step, yielded a continuous coating, sample D, sprayed with a 3 mm scanning step, produced a thin or discontinuous TiO_2 coating, which is confirmed by the presence of peaks characteristic of substrate material in the XRD diffractogram for sample D (Fig. 4.2.1). Thus, scanning step value of 3 mm, combined with a traverse speed of 10 mm/s, fail to meet the conditions necessary for successful TiO_2 deposition, emphasising the critical boundaries for spraying continuous coatings.

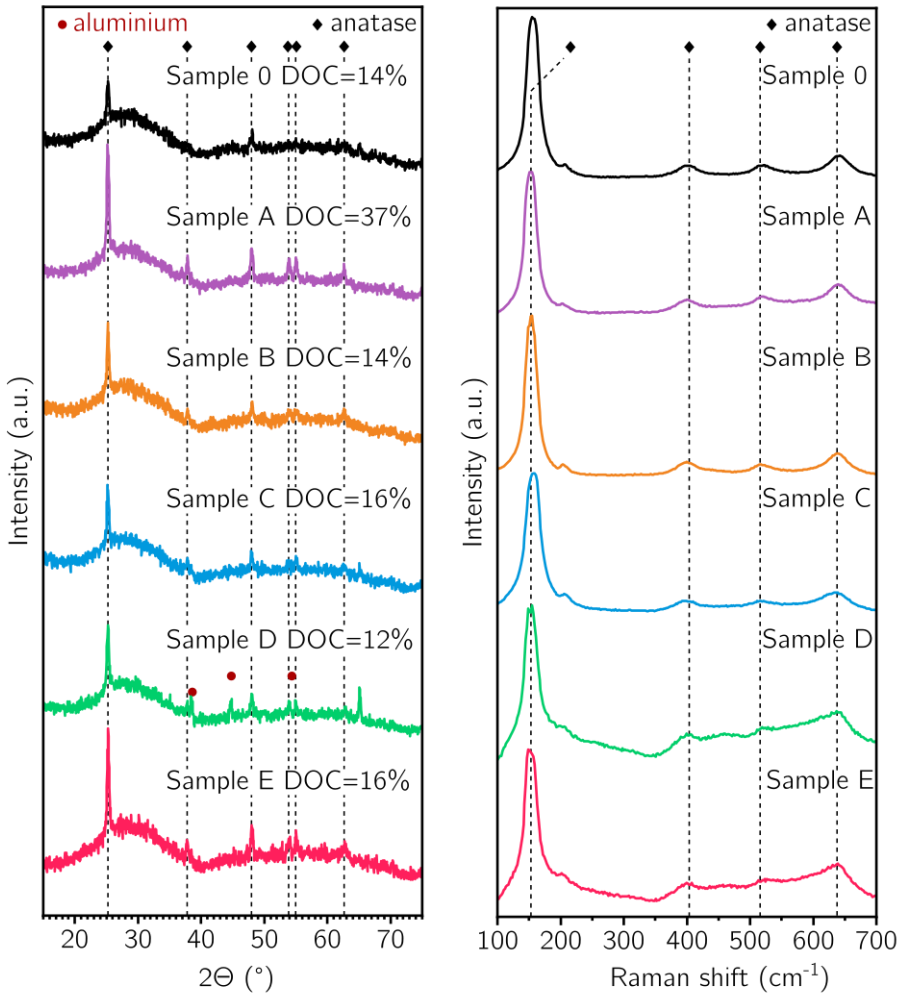

Fig. 4.2.1 On the left there are diffractograms and the DOC values of respective coatings, on the right, Raman spectra of the low-pressure cold-sprayed samples: 0, A, B, C, D and E.

The cross-section microstructures of the LPCS coatings are presented in Fig. 4.2.2. The substrate material, which is grit-blasted before the spraying process, exhibits high surface

roughness. Regardless of the used LPCS process parameters, the substrate surface is consistently coated, with no cracks or voids between the coating and substrate material. The sprayed coatings' structure comprises crystalline, sharp-edged grains embedded within an amorphous, fine-particle TiO_2 matrix. The number of visible grains increases closer to the substrate material. For the single-layer coatings, the crystalline grains form a continuous interconnected matrix, as adjacent grains share boundaries (samples 0, A, B, and E), whereas two-layer samples (samples C and D) exhibit less homogeneity, with smaller grain sizes, that are not interconnected and have more pronounced boundaries with the amorphous matrix. In the microstructure of coating the size of the visible grains decreases near the substrate-coating interface, indicating higher material densification. What is more, enclosed pores are present in all sprayed TiO_2 coatings; however, samples A and E (sprayed with smaller values of the scanning step) exhibit near-interface regions that are largely free from pores, unlike the other samples (0, B, C, and D). At the same time, the near-surface areas of all the coatings are characterised by some degree of porosity and loosely connected particles are visible at the surface. The visible pores are randomly distributed within the amorphous parts of the structure and along the boundaries between the matrix and the crystalline grains. This is particularly visible in samples 0, B, C, and E. Interestingly, apart from sample 0, all the coatings from the mentioned set are sprayed with the increased traverse speed value of 10 mm/s, suggesting that this value is too high to densify the sol-gel-derived TiO_2 powder. Sample A, sprayed with reduced traverse speed, also shows some porosity in the top layer, however, particles at the surface are firmly attached. Similarly, sample D demonstrates an improved top surface, which compared to sample A presents a higher degree of porosity, but there are no loosely attached particles visible. The lack of loosely attached particles in sample D might result from the two-layer deposition process, which removed them from the coating surface.

Sprayed samples' surface roughness examination (Fig. 4.2.2) and optical assessment (Fig. 4.2.3), reveals the correlation between the scanning step value and the coatings' surface roughness. In general, denser scanning step values grant smoother surfaces [108], which is also evident for other kinds of FP, such as metals [115].

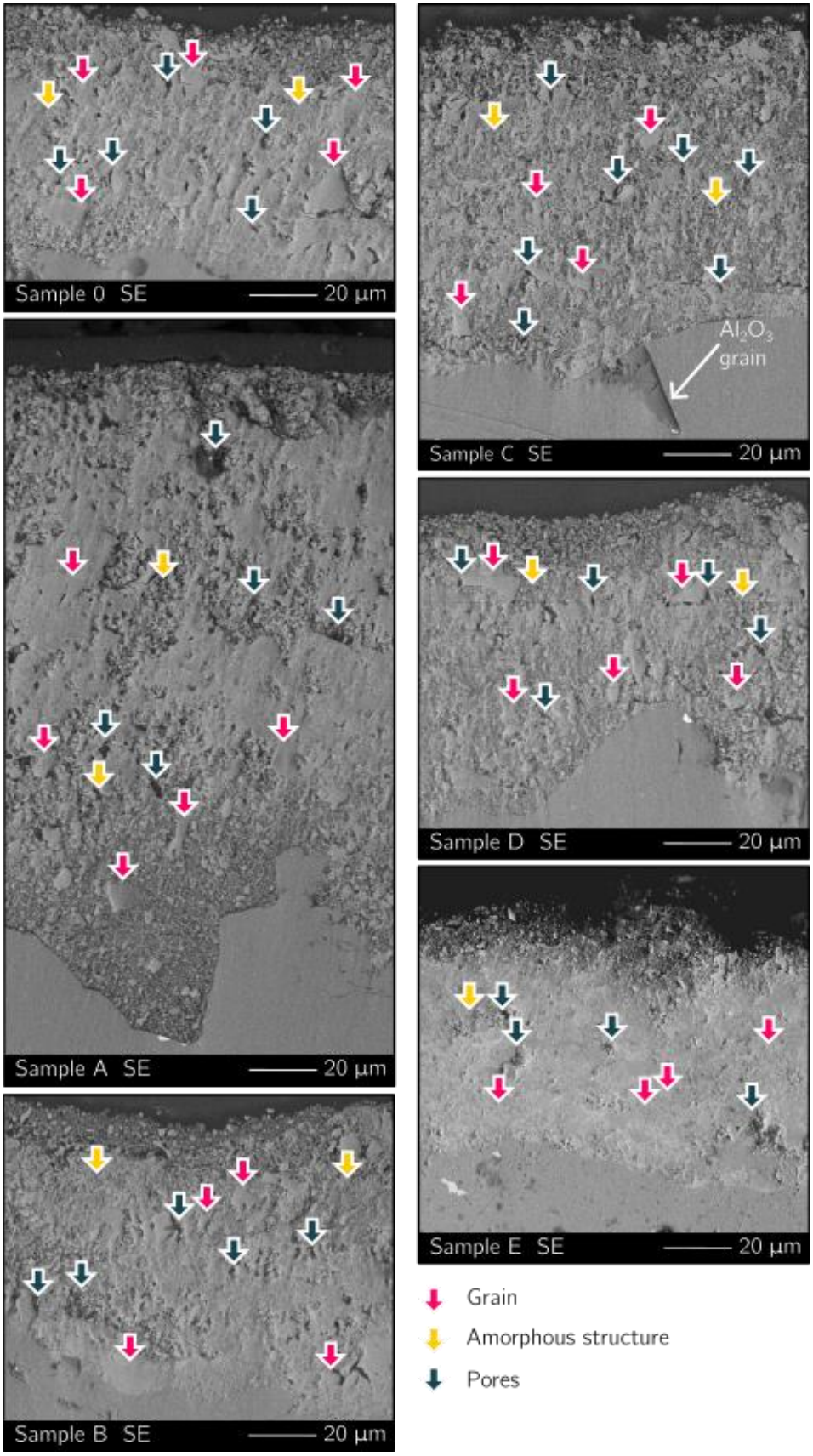

Fig. 4.2.2 the SEM SE images of the cross-section of the sprayed TiO_2 coatings: 0, A, B, C, D, and E. The coating material is at the top of the picture, while the aluminium substrate is at the bottom. The exemplary characteristic parts of the structure are highlighted with the arrows.

Compared to sample 0, sample A, sprayed with a smaller scanning step and a traverse speed of 5 mm/s, shows reduced surface roughness compared to the reference sample 0. The surface of sample A is more uniform and homogeneous (Fig. 4.2.2). Conversely, sample E, sprayed with the same scanning step as sample A but a higher traverse speed (10 mm/s), displays a nearly twofold increase in surface roughness compared to sample 0 (Fig. 4.2.2). Similarly, sample B (sprayed with the same scanning step as sample 0 but with a higher traverse speed) also shows slightly increased surface roughness. Typically, a higher traverse speed promotes uniform particle distribution, reducing roughness [114]. However, in this case, this tendency is not observed. In sample E, the denser scanning step might have increased the thermal energy delivered during the deposition process, enabling loose particle attachment and promoting higher surface roughness. In sample B, the deposition process might have occurred too rapidly to deform and densify the top layer of the coating. In both cases, the coatings' surface roughness increases due to loosely bonded particles remaining on the surface. This suggests that agglomerated powders require severe deformation to achieve smoother surfaces, which is possible when applying a denser scanning step.

Table 4.2.2 Measured roughness, thickness, cohesion and adhesion of the low-pressure cold-sprayed samples 0, A, B, C, D, and E. The x is the mean value calculated, and the s is the standard deviation.

	0		A		B		C		D		E	
	x	s	x	s	x	s	x	s	x	s	x	s
Ra (μm)	6.0	0.8	4.3	1.0	6.4	0.8	7.0	1.1	7.0	0.8	9.5	1.6
Rz (μm)	32.6	4.0	25.4	4.8	34.0	3.6	38.1	6.1	37.4	3.5	60.2	8.8
Thickness (μm)	81	17	189	26	91	22	95	28	69	21	125	20
Cohesion - L_{c1} (N)	1.7	0.7	1.2	0.4	1.5	0.8	1.2	0.4	1.1	0.3	0.8	0.2
Adhesion - L_{c2} (N)	7.2	2.4	≥30.0*	-	10.6	1.9	5.2	2.4	3.6	1.8	20.2	2.6

(*) – the adhesion value exceeded the device's maximum load of 30.0 N.

The attempt to even the surface with the second layer sprayed in the valleys of the first coating causes the increase of the LPCS coatings' roughness. The two-layer coatings (samples

C and D) are characterised by increased roughness values, compared to the reference sample 0. The roughness increase stems from a few reasons. Firstly, the larger scanning step values used (for sample C scanning step value is 2 mm and 3 mm for sample D) promote greater undulations in the surface profile, increasing surface roughness [115]. Secondly, the additional gun passes in multi-layer spraying introduce further profile irregularities [185]. The surface roughness effect on material performance is context-dependent and requires consideration of the operational conditions. Smooth surfaces are generally favoured in engineering contexts due to their positive effect on the material mechanical integrity [116]. Conversely, high roughness is a critical property in biomedical applications, where textured surfaces promote the bonding processes between the bone and the attached implant [185].

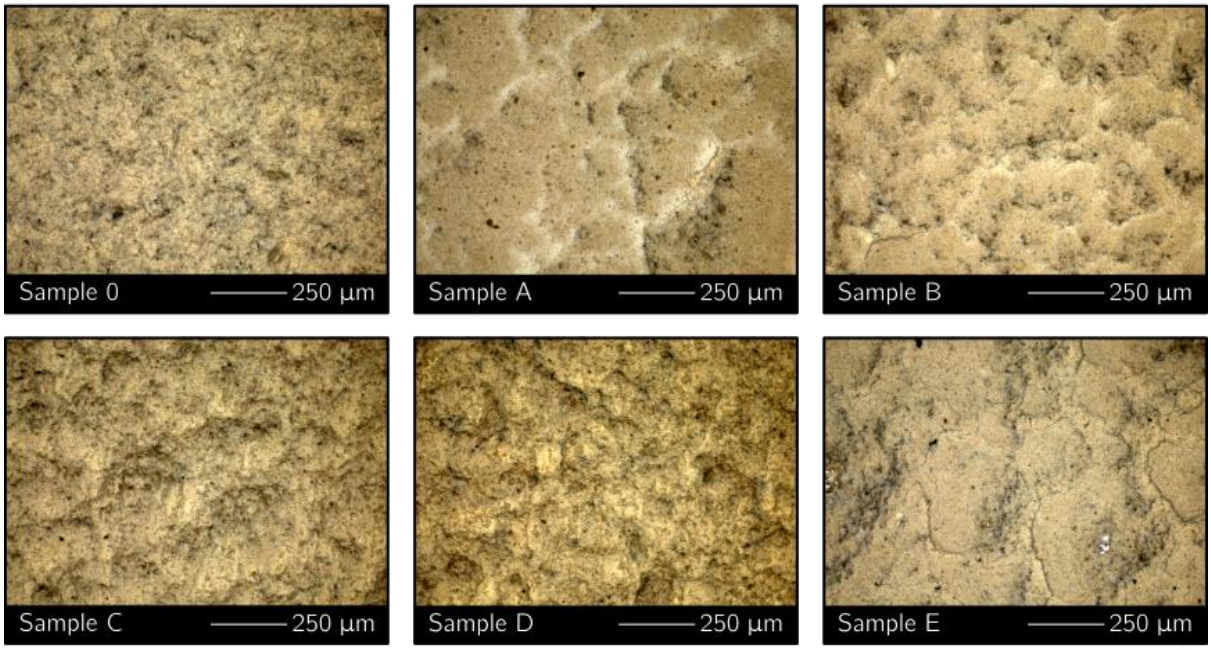

Fig. 4.2.3 Optical micrographs of the LPCS TiO_2 coatings: 0, A, B, C, D, and E. The view presents the top surface of the coatings in magnification x10.

The thickness of the samples varies significantly depending on the used spraying parameters (Table 4.2.2). The reference sample 0 is characterised by a thickness of 80 ± 18 µm. The highest coating thicknesses are achieved with the smallest scanning step values: sample A measures 189 ± 26 µm and sample E measures 125 ± 20 µm. Coatings B and C, sprayed with the same scanning step value as sample 0 but higher traverse speed, have thicknesses of 91 ± 22 µm and 95 ± 28 µm, respectively, making them comparable to

the reference sample. Sample D, sprayed with the widest scanning step value (3 mm), is the thinnest coating (69 ± 21 µm). These results indicate that smaller scanning step values enhance material build-up,improve deposition efficiency and the coatings thickness, which is in line with the literature [186].

Another factor enabling thickness customisation is the traverse speed value adjustment. In LPCS processes, the thickness increases as the traverse speed decreases [184]. For samples sprayed with dense scanning step (e.g., sample A, E), coating thickness increases at lower traverse speeds. Yet, this trend is not evident for coatings obtained with wider scanning steps (e.g., samples 0 and B). This suggests that the LPCS process may be not stable at this value of the scanning step, making it more susceptible to other LPCS process instabilities, like for example powder feeding inconsistencies. In such cases, the process instability factors can have a significantly greater magnitude than the actually controlled parameters - traverse speed.

Additionally, applying a second layer proves ineffective for material buildup. Coating B (single-layer) and coating C (double-layer) are sprayed with the same traverse speed and exhibit comparable thicknesses, despite the doubled spraying time duration for sample C. Considering the fact that the LPCS coatings tend to be more porous in their top part [187], the second-layer gun pass might have removed the weakly-bonded parts located at the top of the TiO_2 coating, preventing the further build-up of the material.

The mechanical properties of the coatings are presented in Table 4.2.2, while the coatings' surface characteristic damage is presented in Fig. 4.2.4. Chosen examples of characteristic damage are presented in detail at the bottom of Fig. 4.2.4. The chipping of the small coating's parts (Fig. 4.2.4, left column) occurs before the material cracking (L_{c1} – cohesive failure). Such material damage in the range of the small load indicates the brittleness and low cohesion of the coating, typical for ceramic materials [188]. The cohesion (L_{c1}) of TiO_2 coatings remains relatively consistent across all samples, with recorded values of 1.9 ± 0.4 N, 1.5 ± 0.4 N, 2.2 ± 0.8 N, 1.3 ± 0.4 N, 1.1 ± 0.3 N, and 0.8 ± 0.2 N for 0, A, B, C, D and E coatings, respectively. The cohesion values suggest that, despite their predominantly amorphous structure (as confirmed by XRD examination), the coatings exhibit brittleness, typical of oxide

materials. The arc-shaped cracks, resulting from tensile stress, are visible only within the scratch track (Fig. 4.2.4, middle column). This type of cohesive damage occurs when the fracture strength of the coatings' material is exceeded and is frequently observed in oxide TS coatings [102,103]. Additionally, the LPCS process may sometimes be insufficient for proper bonding of sprayed materials, particularly oxides [189], leading to increased porosity, especially in the top part where the coating densification is less effective and in turn, decreased cohesion [189,190]. In this case, SEM examinations confirm the presence of pores in all sprayed coatings. Another factor affecting cohesion is surface roughness; rougher surfaces typically exhibit lower mechanical stability [116]. The highest surface roughness is achieved for sample E, which also exhibits reduced material cohesion. On further sliding, the damage progresses into a through-thickness cracking of the coatings. Simultaneously, two types of damages are observed: conformal cracking and ductile tensile cracking, which possibly is the result of the coating's structure consisting of an amorphous matrix and embedded crystalline (anatase) grains. In some cases the conformal cracking is caused by the increased load, resulting from the material being pressed into the scratch track [188]. At higher loads, the damage further evolves to buckle spallation, resulting in substrate exposure (L_{c2} – adhesive failure); again the damage is limited to the scratch track area (Fig. 4.2.4, right column, white patches along the scratch track). The lowest adhesion is observed for samples C and D (two-layer coatings), with adhesive strengths of 5.2 ± 2.4 N and 3.6 ± 1.8 N, respectively. Slightly higher adhesion is observed in samples 0 and B, which differ only in traverse speed, achieving adhesion values of 7.2 ± 2.4 N and 10.6 ± 1.9 N, respectively. The best adhesion results are seen in samples A and E, sprayed with the smallest scanning step. For sample A, adhesion exceeded the device's maximum load and is estimated to be over 30 N, while sample E achieved 20.2 ± 2.6 N. In the microscopic observations the adhesive failure occurs mostly locally, with only small areas of the substrate exposed; full coating detachment is not observed (Fig. 4.2.4, right column). However, for sample 0, damage progression is rapid, uncovering substantial substrate areas during indenter sliding. At the end of each sample's scratch track, piled-up material is observed. The gathered material is the result of indenter movement; it is not bonded with the coating and loosely rests in the scratch track.

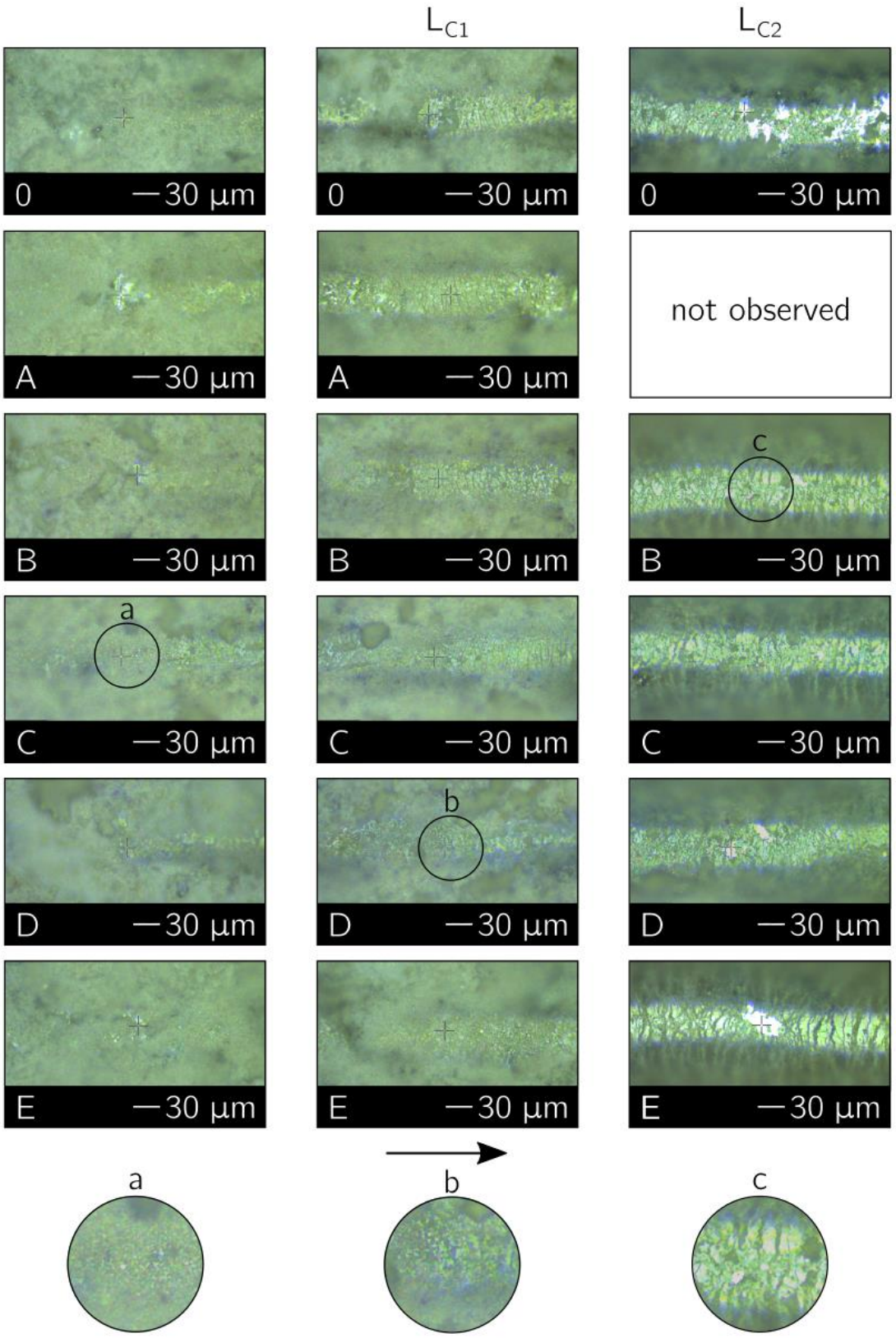

Fig. 4.2.4 Optical micrographs of the surface damage caused by scratch testing of LPCS TiO_2 samples 0, A, B, C, D, and E. The left column presents the small loads' damage, the middle column presents cohesive failure (L_{c1}), right column presents adhesive failure (L_{c2}). The load is progressing from left to right (following the black arrow at the bottom). The detailed exemplary damage is presented below, details a, b and c correspond to small loads' damage, L_{c1} and L_{c2} respectively.

Samples A and E, sprayed with the smallest scanning step and in a single pass, exhibit the best performance. This improvement may be attributed primarily to better material compression, achieved through reduced scanning step values [191]. Additionally, the increased thickness of these coatings correlates with higher adhesive strength. Cross-sectional analysis of samples A and E (Fig. 4.2.2) shows increased homogeneity of their structures, compared to initial sample 0, with sample A additionally displaying a densified region near the substrate, which likely enhances adhesive strength [109,192]. Additionally, the increased crystallinity of the sample A structure can positively affect the material, reducing the number of potential notches as well as pores [189,190]. On the other hand, the two-layer coatings present lower adhesive strength than the initial sample 0. The decrease in the adhesive strength is inversely correlated with the scanning step value; the wider the distance, the lower the adhesion. The lower adhesion may also result from the structure's lower crystallinity and smaller grains present in the material, which do not strengthen the structure through an interlocking mechanism [193].

For the further evaluation of the TiO_2 coating's properties, samples 0 and A are chosen. Sample 0 serves as a reference, while sample A is chosen on the basis of the highest mechanical strength (i.e., adhesion).

Summary

Modification of LPCS process parameters, such as scanning step, number of layers, and traverse speed, enables the production of TiO_2 coatings varying in phase structure, surface properties, thickness, and mechanical characteristics. Sprayed coatings consistently exhibit a mixture of amorphous and anatase structures in varying ratios. The deposition time plays a crucial role in defining the coating's crystalline structure; an extended and uninterrupted spraying duration promotes crystallisation, suggesting that phase composition can be controlled through precise process time optimisation.

Among the chosen LPCS parameters, the scanning step has the most pronounced impact on the TiO_2 coating properties, as it directly influences thickness, roughness, and adhesion

strength. Reducing the scanning step results in smoother, denser coatings with an enhanced adhesion, likely due to the increased material density. The obtained results concerning the effect of a traverse speed on the properties of the coatings do not show a clear tendency. What is more, the number of layers does not significantly influence the final coating thickness, as no notable improvement is observed when applying the second layer. Instead, the second gun pass may induce surface erosion, reducing the coating thickness while increasing roughness.

Based on the obtained results, samples 0 (reference) and A are selected for further examination. Sample A, fabricated with a reduced scanning step and a single-layer deposition, demonstrates the most promising properties, including the highest crystalline fraction and the strongest adhesion to the substrate. The traits make it the most promising candidate for a durable photocatalytic coating, while sample 0 provides a baseline for comparative analysis.

4.2.2 Influence of the ageing process (humid chamber test, multi-cycle dye decomposition test) on the TiO_2 coatings' structure and properties

The coatings' 0 (initial, reference coatings) and a (the most durable coating based on the adhesion strength results presented in 4.2.1) stability assessment involves two experiments, the first consisting of the long-term ageing (1000 h) of the material of the coating in the humid chamber to assess their structure stability. After the ageing process, samples are denoted as chamber-aged samples 0^{1000} and A^{1000}. The second experiment is based on the multi-cycle dye decomposition tests to determine the photocatalytic activity and stability (4-cycle dye decomposition test) of the samples, both before and after the chamber-ageing process. This Section is based on the results published in [180] and [181].

Fig. 4.2.5 shows diffractograms (left) and Raman spectra (right) of as-sprayed samples 0 and A (described in previous Section 4.2.1) and chamber-aged samples 0^{1000} and A^{1000}. The chamber-aged samples' diffractograms present more pronounced anatase peaks present at 25.25°, 37.85°, 48.00°, 53.90°, 55.05°, 62.70°, 68.95° and 70.04° 2theta, compared to the as-sprayed samples (0 and A). Peaks' intensity increase is the result of the higher crystallinity of the aged coatings' structure. Additionally, new peaks characteristic of the brookite structure are visible at 30.75°, 36.25°, 40.10°, 42.30°, 46.15°, 49.10°, 57.05° and 64.50° 2θ [180]. The Raman spectra of the samples (0, A, 0^{1000} and A^{1000}) confirm the results from the XRD analysis. The anatase bands are located at 149, 391, 513 and 631 cm^{-1} and less intense brookite-related bands at 256, 321, 368, 470 and 546 cm^{-1} [38]. The estimated *DOC of* the chamber-aged samples reveals that their crystallinity significantly increases after the ageing process (Fig. 4.2.5). Sample 0 crystallinity is 17 ± 4%, increasing up to 72 ± 6% in the 0^{1000} sample. Similarly, the crystallinity of sample A, which is 37 ± 11%, after ageing in the chamber reaches 78 ± 4%. It seems that regardless of the initial coating's crystallinity the ageing process induces further material crystallisation up to around 75%.

Based on the literature analysis, the temperature used in the chamber-ageing process (40°C) is too low to trigger the further crystallisation of the as-sprayed coatings alone. However, it is possible to induce the low-temperature crystallisation of such structures using water as

a medium [194–197]. Both coatings subjected to the chamber-ageing process are exposed to water vapour, which can penetrate the structure and provide the conditions needed for water-assisted crystallisation. Water-assisted crystallisation predominantly yields the anatase phase [194–197]. The anatase structure is promoted as a result of the increased number of hydroxyl groups attached to the TiO_6 octahedra. In such conditions, the octahedra favour bonding through face sharing, yielding an anatase structure [195]. However, in the case of samples 0^{1000} and A^{1000}, the water-assisted crystallisation of the amorphous structure leads to the crystallisation of the brookite phase rather than anatase. The literature indicates that brookite TiO_2 crystallisation is promoted in oxygen-depleted environments [198] or by introducing lower-oxidation-state cations (e.g., Ti^{3+}, Fe^{3+}) during synthesis [199]. This suggests the existence of another factor influencing crystallisation apart from water vapour presence, such that the brookite lattice is favoured during the structural organisation when samples are subjected to chamber-ageing.

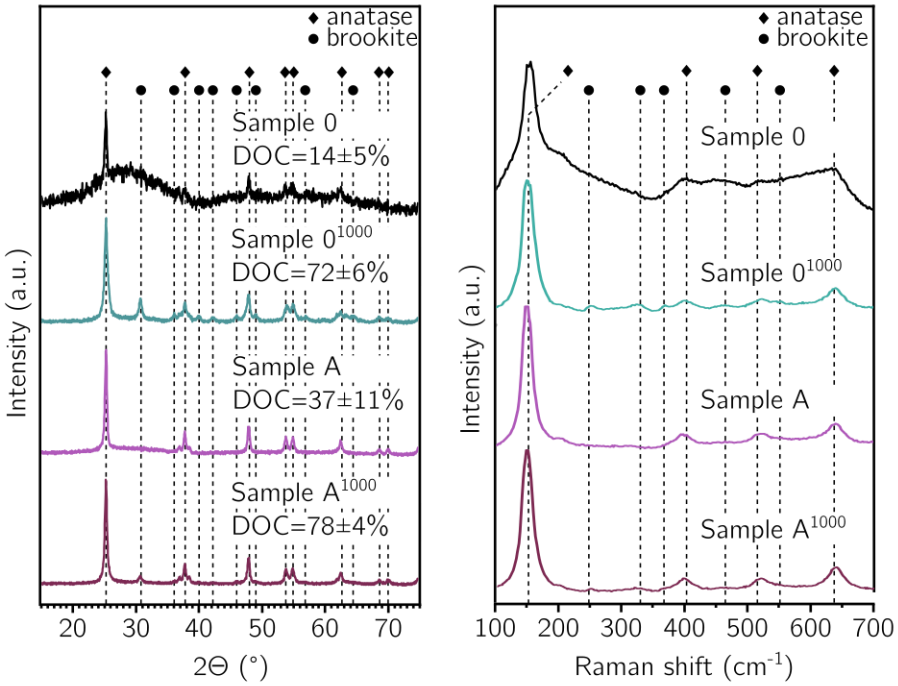

Fig. 4.2.5 On the left there are diffractograms and the *DOC* values of respective coatings, on the right Raman spectra of the low-pressure cold-sprayed samples: as-sprayed 0, A, and chamber-aged: 0^{1000} and A^{1000}.

The microstructures of the samples are presented in Fig. 4.2.6. The coatings' microstructure comprises two types of particles: smaller irregular-shaped particles – which serve as a matrix

and are likely amorphous, and sharp-edged particles that are randomly distributed and may be crystalline. The detailed description of the coatings 0 and A microstructure is presented in the previous Section 4.2.1. Two grains observed at the sample's a coatings/substrate interface are the result of the grit blasting process, which can embed the Al_2O_3 grains into the substrate material. A comparison of the as-sprayed and chamber-aged samples reveals no discernible differences in the TiO_2 coating structure or porosity, implying that the chamber-ageing process does not significantly affect these properties. However, at the interface with the aluminium substrate, a new, thin, continuous interlayer is observed, indicating oxidation of the aluminium. Based on cross-sectional observations, the newly formed passivation layer reaches up to 5 µm in thickness; an order of magnitude greater than the naturally occurring passivation layer, which typically measures only a few nanometres [200]. Considering that both as-sprayed TiO_2 coatings are characterised by some porosity (Fig. 4.2.6), the voids in the structure may facilitate water penetration. Consequently, the substrate passivation process could be accelerated by the water that penetrated the porous TiO_2 coating down to the substrate [180]. Apart from the formation of the passivation layer, SEM analysis shows no other notable changes caused by the ageing test, such as discontinuities, voids or cracks within the coatings.

The TiO_2 coating and the aluminium substrate show different mechanisms of ageing. Based on the literature, these separate ageing processes can eventually interact, affecting each other. In many cases, metallic substrate ageing triggers the migration of ions from the substrate to the TiO_2 coating [201,202]. Additionally, in both as-sprayed coatings, the structure consists of the amorphous and anatase phases, with the former being dominant, as evidenced by the DOC estimation. This amorphous character of these coatings likely facilitates the Al^{3+} diffusion from the aluminium substrate into the coating structure, as ion migration is more efficient in defective and amorphous systems [203]. Additionally, the ionic radius of Al^{3+} ($r_{Al^{3+}} = 0.535$ Å) and Ti^{4+} ions ($r_{Ti^{4+}} = 0.605$ Å) is similar, which makes it possible for the aluminium ions to substitute the titanium ions within the octahedral sites. However, this substitution (Al^{3+} replacing Ti^{4+}) introduces a charge imbalance due to aluminium's lower valence. The stabilisation of this system can be achieved through the formation of positively charged

oxygen vacancies. Which, as mention before might promote the crystallisation of the brookite rather than the anatase phase [204]. As mentioned, the chamber-ageing aloe is not sufficient for triggering the crystallisation process, however, interaction with water vapour may provide the necessary energy (via hydrolysis or surface-adsorbed moisture) [197]. This leads to the conclusion that the crystallization of brookite must be related to the interaction of two factors at the same time: water penetration and its interaction with the coatings and oxygen depletion of the amorphous TiO_2 structure caused by the substrate passivation [180].

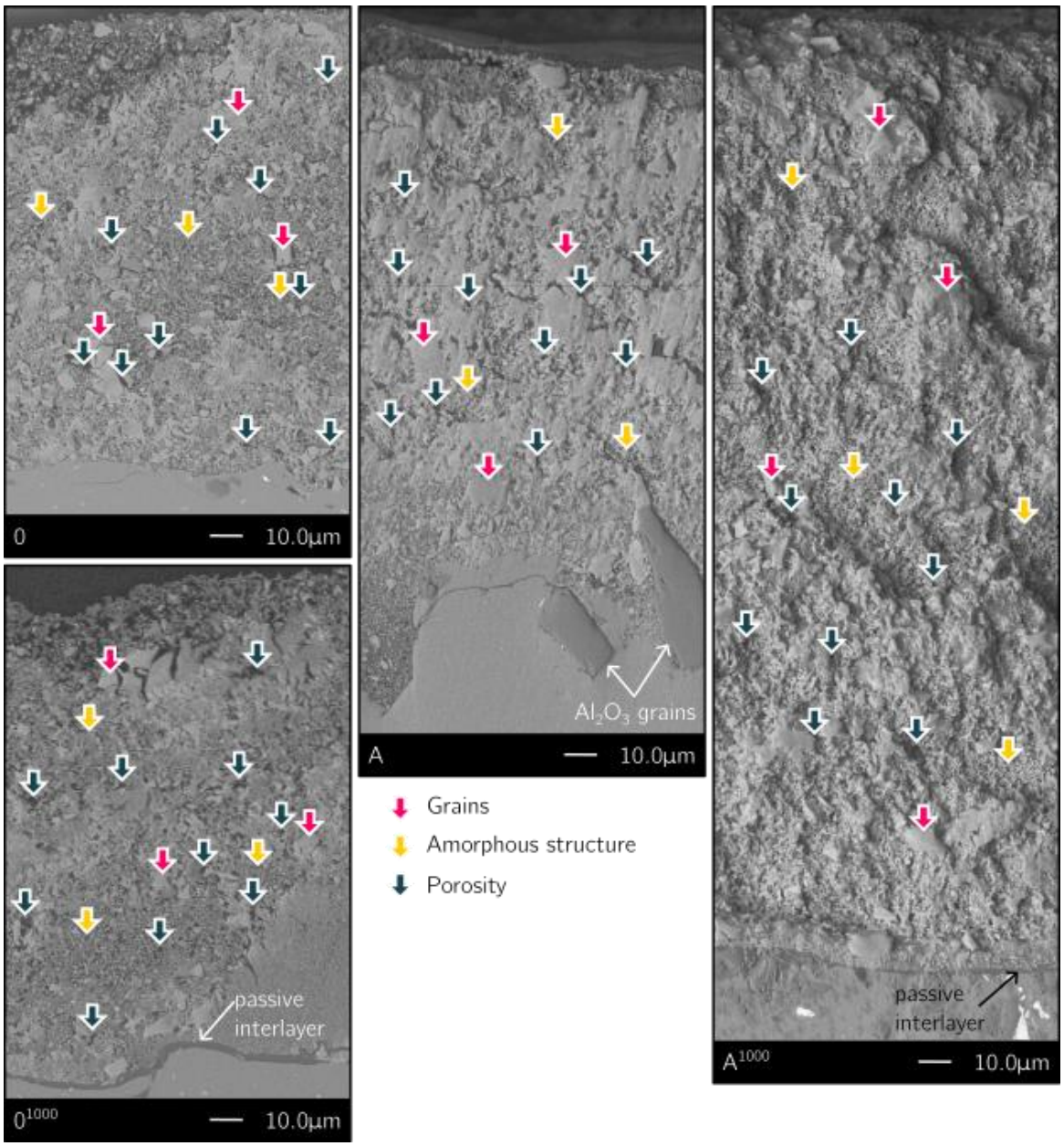

Fig. 4.2.6 the morphology of the 0, 0^{1000}, A and A^{1000} selected samples. The pictures are taken in the topographic contrast. The noticeable thickness difference between as-sprayed and aged samples is still within the expected range (sample 0 thickness 118 ± 49 µm and sample A thickness 254 ± 90 µm).

Both amorphous and crystalline TiO_2 structures are arranged out of TiO_6 octahedra [205]. However, to form a distinct crystal lattice, multiple TiO_6 octahedra adopt a specific spatial configuration by sharing either an edge or a vertex (corner) (Fig. 4.2.7) [206]. Between these two configurations, vertex sharing is preferred as it minimises Coulomb repulsion between two adjacent ions of the same charge. As a result, the most thermodynamically stable polymorph, rutile (Fig. 4.2.7.a), has the highest amount of vertex-sharing octahedra, followed by brookite (Fig. 4.2.7.b), and then anatase (Fig. 4.2.7.c), which is built mostly from the edge-sharing octahedra. In contrast to these crystalline forms, amorphous TiO_2 (Fig. 4.2.7.d) lacks long-range spatial ordering, and some of its TiO_6 octahedra are partially hydrolysed. Partial hydrolysis results in the retention of hydroxyl (-OH) groups that remain bound to titanium ions. The interactions between TiO_6 units under water-assisted and oxygen-deficient crystallisation conditions will therefore be examined in the paragraphs that follow.

The crystallisation of TiO_2 phases from this amorphous state proceeds through dehydration and subsequent cross-linking process, where water molecules facilitate the bonding of adjacent octahedra. Initially, a water molecule, via its lone electron pairs, links two hydroxyl (-OH) groups from neighbouring octahedra. The reaction between the detached hydroxyl (-OH) group from one octahedron and a proton (H^+) from the adjacent octahedron creates a new water molecule. The remaining oxygen atom, having lost the proton, forms an edge-sharing bond with the second octahedron (Fig. 4.2.7.d). A higher concentration of hydroxyl groups promotes frequent edge-sharing, driving the formation of anatase. At the same time, the presence of water in the TiO_2 coating structure and its interaction with the aluminium substrate which undergoes passivation, leads to the formation of an oxide layer at the coating-substrate interface. This passivation process can draw oxygen from the surrounding TiO_2 structure, potentially creating oxygen vacancies and affecting the crystallisation pathway. These vacancies drive a spatial rearrangement of octahedra from an edge-sharing to a vertex-sharing configuration (Fig. 4.2.7.e). Under conditions of significant oxygen deficiency, rutile formation is favoured. However, in this case, the oxygen depletion is moderate, resulting in the crystallisation of brookite rather than rutile [180].

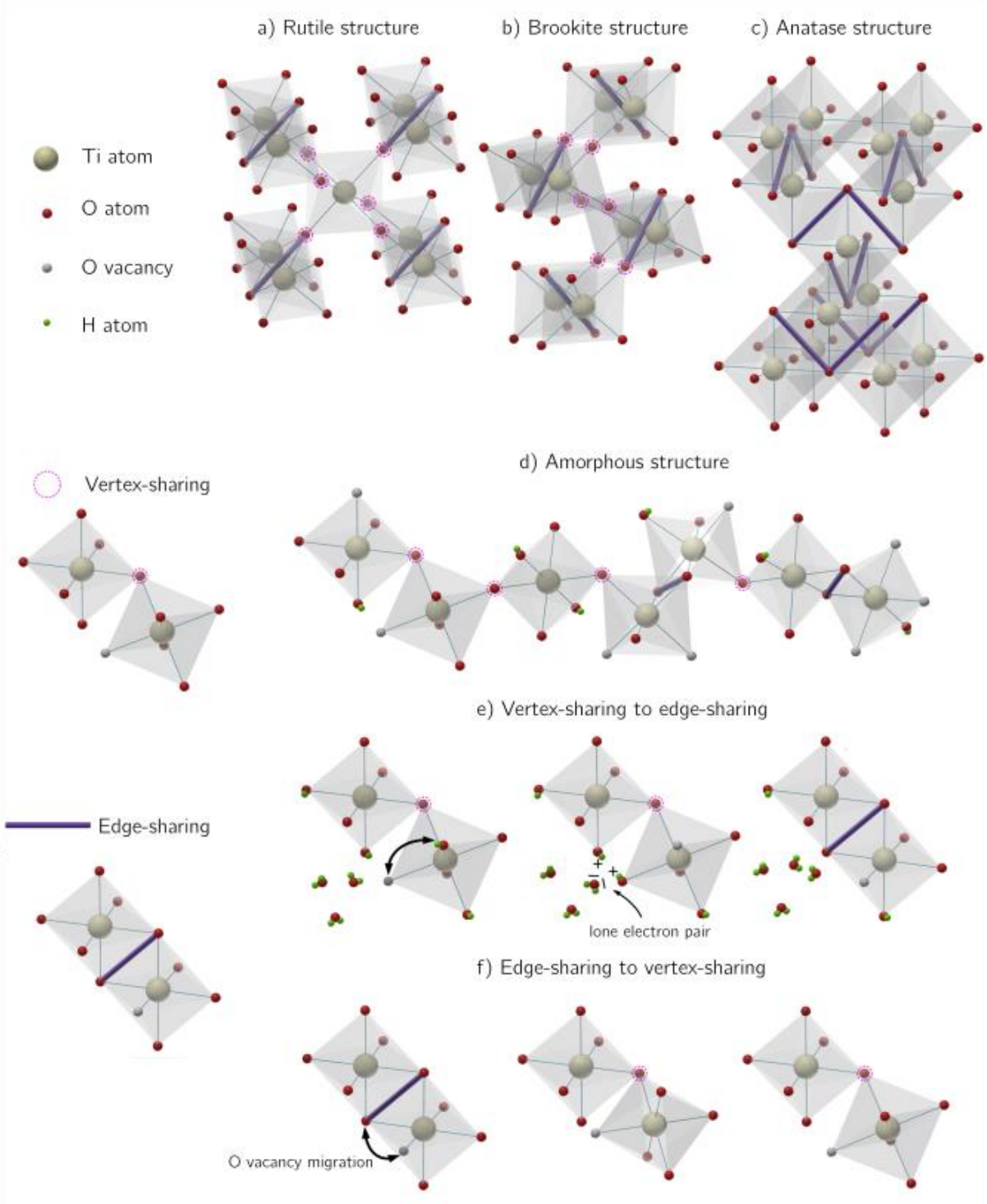

Fig. 4.2.7 Schematic representation of structural reorganisation of TiO_6 octahedral connectivity and configuration with an indication of octahedra connected by edges or corners. Crystal structure of a) rutile, b) brookite, c) anatase and d) amorphous phase. e) Formation of edge-sharing connection from corner-shared TiO_6 octahedra containing residual hydroxyl groups in the water environment. f) Formation of edge-sharing connection from corner-shared TiO_6 octahedra due to migration of oxygen vacancies. Adapted from [180].

The thickness of the as-sprayed samples 0 and A varies significantly due to variations in the scanning step values (2 mm and 1 mm, respectively) used for the LPCS deposition. For

sample A, where the scanning step is smaller, the TiO_2 coating is thicker compared to sample 0 (Table 4.2.3). The presented average thickness values show some variation for the as-sprayed samples when compared to the data presented earlier in Section 4.2.1. Although, these differences remain within the margin of measurement uncertainty. This variation may arise from the fact that results presented in this Section onward are calculated from the increased number of samples for each type, which introduces variability between separate samples series.

Table 4.2.3 Assessed thickness, cohesion and adhesion of the low-pressure cold-sprayed samples 0, A, 0^{1000}, and A^{1000}. The x is the mean value calculated, and the s is the standard deviation.

	0		A		0^{1000}		A^{1000}	
	x	s	x	s	x	s	x	s
Thickness (µm)	118	49	254	90	141	41	256	91
Cohesion - L_{c1} (N)	1.7	0.7	1.2	0.4	1.0	0.3	2.1	0.9
Adhesion - L_{c2} (N)	7.2	2.4	≥30.0*	-	9.5	2.8	17.7	2.5

(*) - the adhesion value exceeded the device's maximum load of 30.0 N.

In terms of structure, the most significant difference between the as-sprayed samples lies in their crystallinity, which can further influence the mechanical properties of the TiO_2 chamber-aged coatings. For this reason, the as-sprayed and chamber-aged samples are compared in terms of cohesion and adhesion strength. In general, the surface damage follows the described tendencies so far: at small loads, the chipping of all coatings happens, regardless of the coatings' crystallinity (Fig. 4.2.8, left column). The example of the chipping is provided in Fig. 4.2.8a. With the indenter load increase, the deformation of the coatings is visible, as the track after the passing indenter appears. The cohesive failure takes the form of arc-shaped cracks (Fig. 4.2.8b), which is the result of the tensile strength exceeding the coatings' material integrity [188], the cracks appear only in the scratch track (Fig. 4.2.8, middle column). Cohesion values are similar across all the TiO_2 coatings, ranging from 1.02 to 2.1 N, despite the minor differences in the value they fall within the error margin. With further load increase, when the material is bent into the scratch track of the coating, damage evolves into conformal cracking [188]. This type of damage appears almost simultaneously with the brittle tensile

cracking in the A^{1000} sample (Fig. 4.2.8c). For the rest of the samples, the damage evolution takes longer. Additionally, for all scratched coatings the conformal cracking is limited to the scratch track (Fig. 4.2.8, right). The adhesive strength measurements highlight the disparity between samples 0 and A. Sample 0 exhibits the lowest adhesion (7.2 ± 2.4 N), while sample A exceeds the device's maximum load and is therefore denoted as ≥30.0 N; both are described in detail in the previous Section 4.2.1. The chamber ageing process has a contradictory influence on the sample; in the case of sample 0^{1000} it works in favour of the adhesion, enhancing its value to 9.5 ± 2.8 N. While the chamber-ageing of sample A results in a significant reduction in adhesion, down to 17.7 ± 2.5 N. Similarly to the scratch-test results of the coatings described in the previous Section 4.2.1, at the end of the scratch track left after the indenter passing, the removed coating material has piled up.

The contradictory effects of the humidity-chamber ageing process on the coatings' 0 and a properties can be attributed to the adhesion mechanism at the coating-substrate interface. While these mechanisms are well-established in principle, their application in this specific context is still underexplored. The bonding of two materials results from several possible interactions, which can be divided into two types: first, based on chemical/physical bonding, and second, based on mechanical bonding (Fig. 4.2.9) [207,208]. The first one, namely chemical/physical bonding, takes place at an atomic/molecular scale and arises from chemical interactions such as covalent, ionic, and metallic bonding (including metallurgical bonding) or Van der Waals forces which hold the atoms of the coatings and substrate together [88,209]. The second one, mechanical bonding occurs at a micro/macroscopic scale and depends mainly on the material's surface properties and the powder's morphology. Ridges, grooves or irregularities on the surfaces facilitate the physical interlocking of the materials [210], while the suitable size and shape of the powders can promote the embedding of particles into surface irregularities, enabling the mechanical bonding process [23]. Since the two bonding types happen at different scales, they can occur in the same space simultaneously, and while chemical interactions provide an essential bonding at the molecular level, the mechanical one can strengthen the materials' connection through physical contact [207].

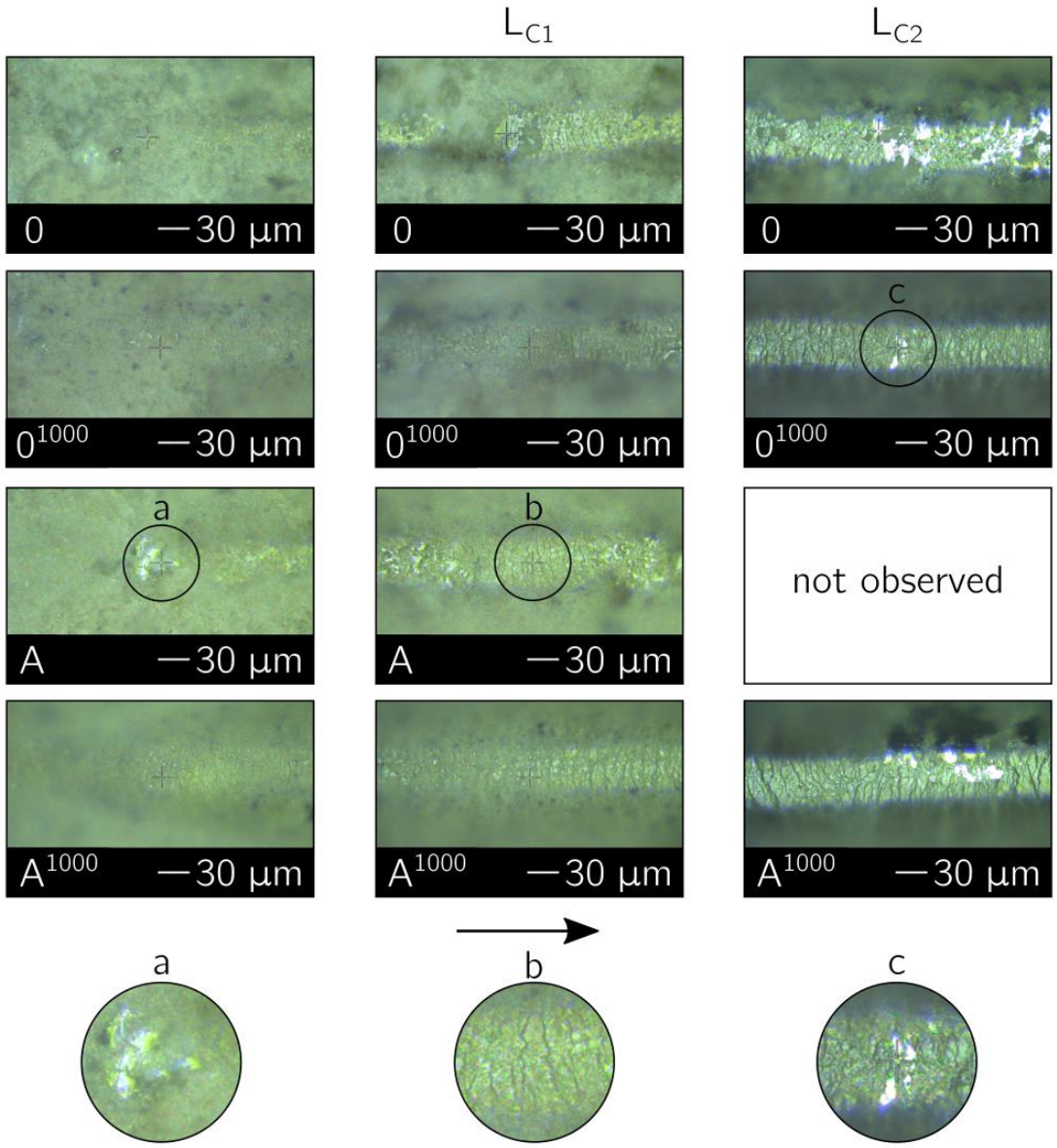

Fig. 4.2.8 Optical micrographs of the surface damage caused by scratch-testing of LPCS TiO_2 samples 0, 0^{1000}, A, and A^{1000}. The left column presents the small loads' damage, the middle column presents cohesive failure (L_{c1}), right column presents adhesive failure (L_{c2}). The load is progressing from left to right (following the black arrow at the bottom). The detailed exemplary damage is presented below; details a, b and c correspond to small loads' damage, L_{c1} and L_{c2} respectively.

Identifying the main type of coating-substrate bonding in materials produced by thermal spraying deposition processes is quite straightforward. Most of the TS methods utilise heat to facilitate permanent chemical bonding coating and substrate materials [209,211]. However, when a low-temperature technique, such as low-pressure cold spray is used, the determination of the bonding mechanisms becomes more complex. Given the characteristics of the LPCS process, mechanical bonding is expected to be the predominant factor [66]. Nevertheless,

the use of sol-gel-derived amorphous TiO_2 feedstock powder increases the chances of chemical interactions between the coating and substrate. Therefore, both bonding types are likely to occur; yet, a deeper insight into the semicrystalline TiO_2 coating and aluminium substrate material interactions is needed to discern the main bonding factor in the case of coatings 0, A, 0^{1000} and A^{1000}.

The amorphous TiO_2 feedstock powder is used for obtaining the coatings. Unlike the commercially available powders, this TiO_2 sol-gel powder contains a lot of alkoxide and hydroxyl groups attached to titanium ions remaining after synthesis. Some groups can remain in their unaltered (-Ti-O-R) or hydroxylated form (-Ti-OH) [131] constituting an obstacle to the crystallisation of the oxide network [137]. This TiO_2 powder is cold-sprayed onto the aluminium substrate, which naturally oxidises, forming a surface layer of -Al-OH [212]. As a consequence, at the interface between the layer and the substrate, three types of chemically reactive groups can be present in the region: -Ti-OH and -Ti-O-R (both from the TiO_2 coating), and -Al-OH (from the substrate). These groups chemically interact with each other and link the natural passivation layer on the aluminium substrate to the TiO_2 coating (-Al-O-Ti- or -Al-O-H··Ti) [212,213]. The amorphous nature of the feedstock powder influences the number of chemical bonds formed; a higher amorphous content enhances the potential for bond formation because the disorganised, thermodynamically unstable structure of low–crystalline materials lowers the energy barrier for chemical bonding [214]. In addition, the LPCS process itself can moderate the number of established bonds. A lower processing temperature helps to preserve a higher amount of organic groups within the coating material, thereby further facilitating chemical bonding [88,215]. In contrast, mechanical bonding arises from the interlocking of crystalline grains present on the aluminium substrate, which is further enhanced by the increased surface roughness achieved through grit blasting [216]. Consequently, greater coating crystallinity enhances mechanical adhesion as the number of interlocked crystalline grains increases. These two bonding mechanisms – chemical and mechanical – and their relationship to the material's crystallinity (i.e., the proportion of crystalline grains within the amorphous matrix) account for the notably different adhesion

results observed for sample 0 and sample A. Sample 0, characterised by a low amount of crystalline grains in the coating material, primarily attaches to the aluminium substrate through chemical bonding. Whereas, sample A, with a more crystalline and densified TiO_2 coating structure, relies more on mechanical bonding than chemical for adhesion (Fig. 4.2.10, samples 0 and A).

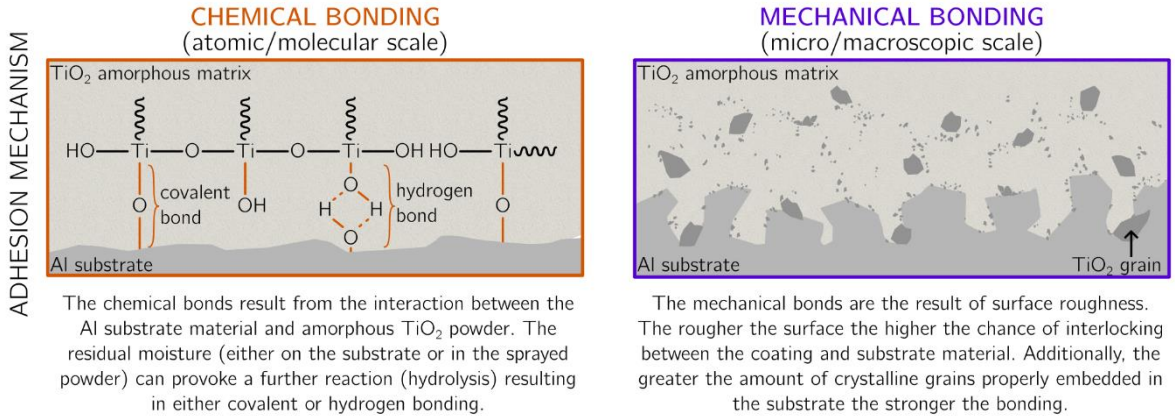

Fig. 4.2.9 the adhesive bonding mechanisms of the LPCS TiO_2 coatings on aluminium substrate. Adapted from [181].

The chamber ageing process led to the overgrowth of the passivation layer in the interface area from manometer range up to 5 µm for samples 0^{1000} and A^{1000} (Fig. 4.2.10). The formation of the aluminium passivation interlayer resulted in the creation of new Al-OH chemical bonds, thereby promoting the creation of additional Al-O-Ti and Al-O-H··Ti bonds between the interlayer and coating material [213,217]. The adhesion increase observed for sample 0^{1000} stems from the described phenomenon, as increasing the number of chemical bonds in the interface enhances the coating's adhesion to the substrate [213]. Another contributing factor that affects the adhesion is the expansion of the substrate passive layer, which leads to an increase in the surface area (at the nanoscale) where bonds can form (Fig. 4.2.10, sample 0^{1000}). However, in the case of sample A^{1000}, the reorganised substrate/coating interface did not yield positive effects. In this case, expansion of the passivation layer, whilst promoting new chemical bonds, may also diminish interface geometry (at the microscale). Without the main driving factor (Fig. 4.2.10, sample A^{1000}) of the elevated mechanical adhesion of as-sprayed coating A, its adhesion is reduced [207].

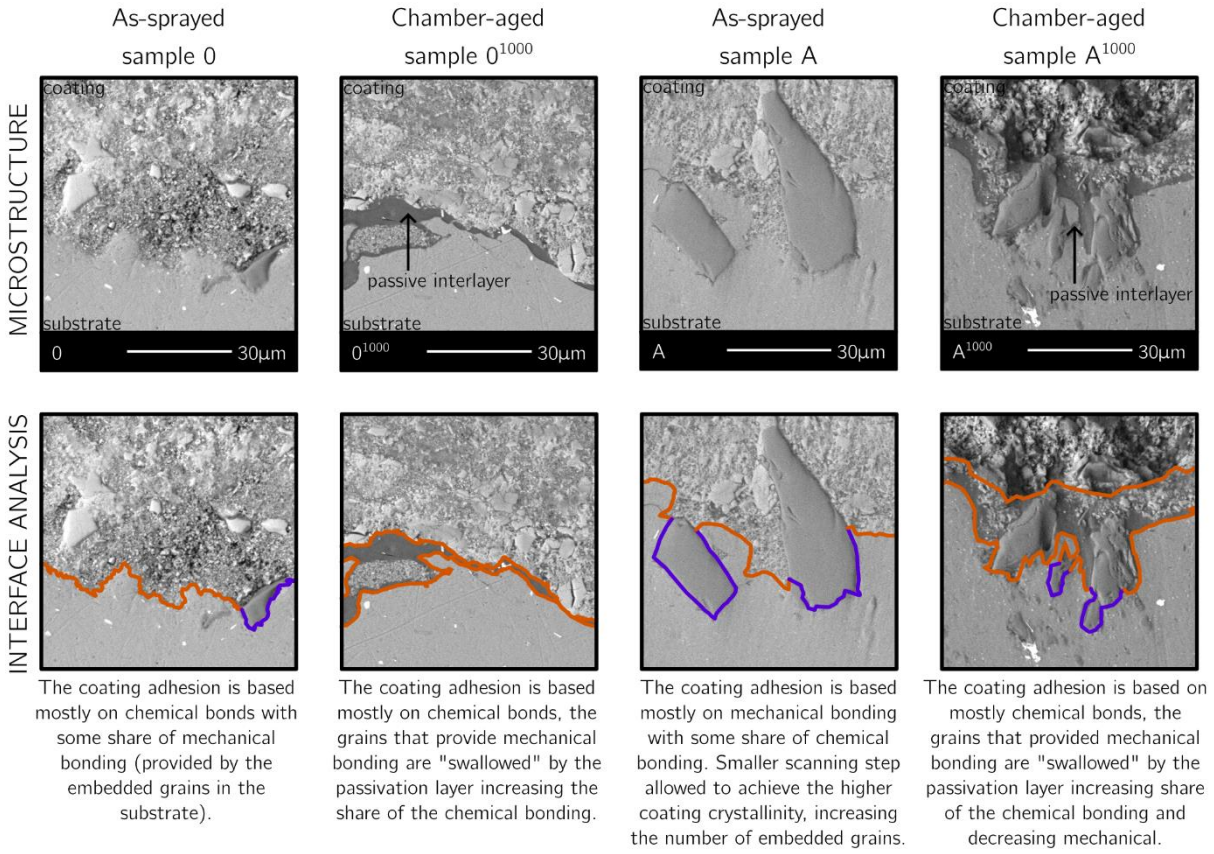

Fig. 4.2.10 the interface analysis of the LPCS TiO_2 coatings. The interface region was analysed in terms of two types of bonding mechanisms chemical (orange) and mechanical (blue).

The 1000-hour chamber-ageing process simulates the long-term operation of TiO_2 photocatalytic coatings. Taking into account the effects of ageing on the as-sprayed coating structure, sample A exhibits superior material stability for several reasons. Firstly, the initial adhesion strength of sample A exceeds that of sample 0 which makes it a more durable photocatalyst. Secondly, even after chamber-ageing, the adhesion of sample A^{1000} remains twice as high as that of sample 0^{1000}. Given the differences in crystallinity and initial adhesion mechanisms between the two as-sprayed samples, it can be assumed that the initial crystallinity of the photocatalyst is a key variable in predicting the effects of ageing on adhesion strength of TiO_2 LPCS photocatalytic coatings. Although coatings with a predominantly amorphous structure may experience an increase in adhesion over time, those with higher crystallinity and bonding mechanisms based on mechanical interlocking ultimately demonstrate greater durability.

The band gap values and the light adsorption properties of the as-sprayed and chamber-aged coatings are determined before the four-cycle dye decomposition test. The determined band gap energies are comparable with the anatase phase band gap value (Fig. 4.2.11, left), with minor variations (3.18 eV for A and A^{1000} and 3.21 eV and 3.23 eV for 0^{1000} and 0) [218]. The small band gap value shifts might result from the differing crystallinity of the samples [219]. The light absorption characteristics of the coatings are presented in Fig. 4.2.11 on the left. Both as-sprayed and chamber-aged coatings are characterised by negligible adsorption in the visible range (>400 nm). The highest absorption of the light is in the UV range (<400nm), which is typical for the non-modified TiO_2 material [220].

The photocatalytic stability of the samples is estimated based on a four-cycle MB decomposition test. The single decomposition test consists of three steps: the conditioning of the samples, which allows them to reach the adsorption/desorption equilibrium; the photocatalytic decomposition of the dye when the coatings are activated with the UVA lamp; and the rest time in which samples are dried and their surface is cleaned with the UVA irradiation. Afterwards, this single experiment is repeated up to four times using the same sets of samples. Throughout the test, the coatings are irradiated with the UVA lamp (lamp properties are characterised in 3.3.113.3.11.2).

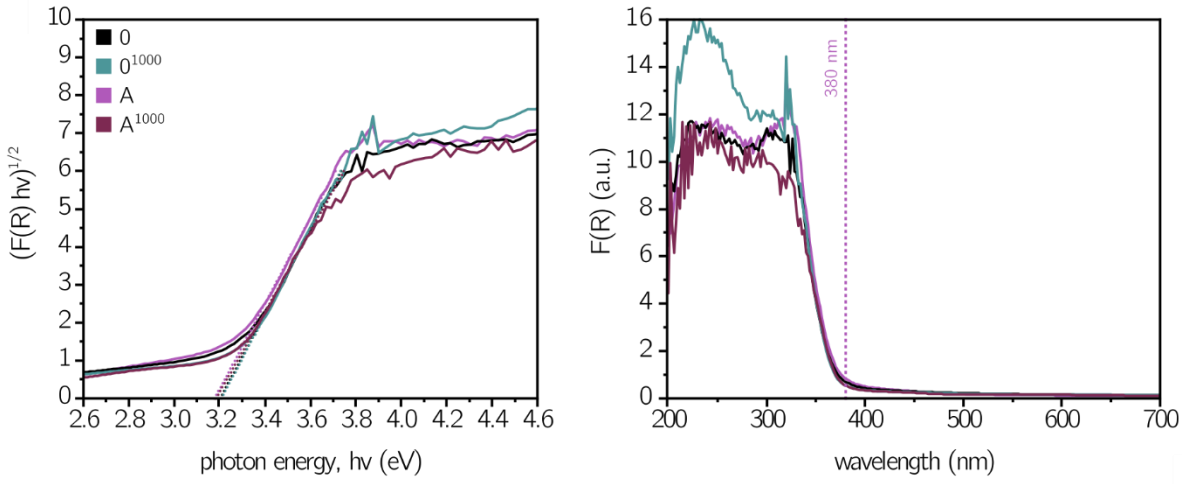

Fig. 4.2.11 On the left, the Tauc plots are used to determine the band gap energy values for the TiO_2 as-sprayed coatings 0 and A and chamber-aged coatings 0^{1000} and A^{1000}. On the right is the Kubelka-Munk function plot for the sprayed TiO_2 coatings, presenting their adsorption band.

The first step of the photocatalytic reaction is the adsorption of the MB dye molecules onto the photocatalyst surface, corresponding to a conditioning period of two hours prior to UVA lamp activation. In the first cycle of the experiment, the as-sprayed samples 0 and a display slightly different adsorption performances, with sample 0 adsorbing 11% and sample A adsorbing 9% of the dye (Fig. 4.2.12 top, left). Over the next cycles, their adsorption evens out around 8%. Due to the sample's 0 significant adsorption variability, the difference between the two samples becomes negligible. What is more, a reduction in adsorption is observed for both as-sprayed coatings after the first cycle. This decline may be the result of a reduction in the number of available adsorption sites on the coatings' surfaces after the initial cycle. Adsorption is driven by the diffusion of the MB dye molecules, which attach to the adsorption sites on the photocatalyst surface. While UVA irradiation degrades these molecules, freeing some adsorption sites, dye molecules localised in less exposed areas, such as pores, may remain intact, reducing the number of accessible sites [221–223].

The second step of the photocatalytic experiment involves the UVA lamp's activation and the decomposition of the MB dye. Across the four-cycle experiment, as-sprayed samples exhibit differing levels of efficiency. Sample 0 consistently decomposes approximately 20% of the MB dye, while sample A achieves a slightly higher efficiency of around 24% (Fig. 4.2.12, middle, left). Another difference between the as-sprayed samples is the consistency of their results; sample A produces more consistent decomposition results over repeated cycles, while sample 0 shows significant variance in activity. These inconsistencies may stem from differences in the coatings' crystalline structures: varying ratios of crystalline to amorphous TiO_2 phases. The randomness of the amorphous structure hampers reproducibility, since its defects, their's concentration and type are difficult to predict, govern the photocatalytic process [17]. On the other hand, a high crystallinity of the TiO_2 structure is known to slow down the recombination of charge carriers, enhancing the photocatalytic process [224]. Furthermore, the kinetics of MB dye decomposition for the as-sprayed coatings outline the differences between the samples (Fig. 4.2.12, bottom, left). For sample 0, a decline in reaction rate is observed after the first cycle and then stabilises, whereas sample A demonstrates

stable reaction kinetics throughout the test. The reducing efficiency of the more amorphous sample 0 may result from the accumulation of partially oxidised intermediates on the photocatalyst's active sites, which gradually deactivates the coating [160].

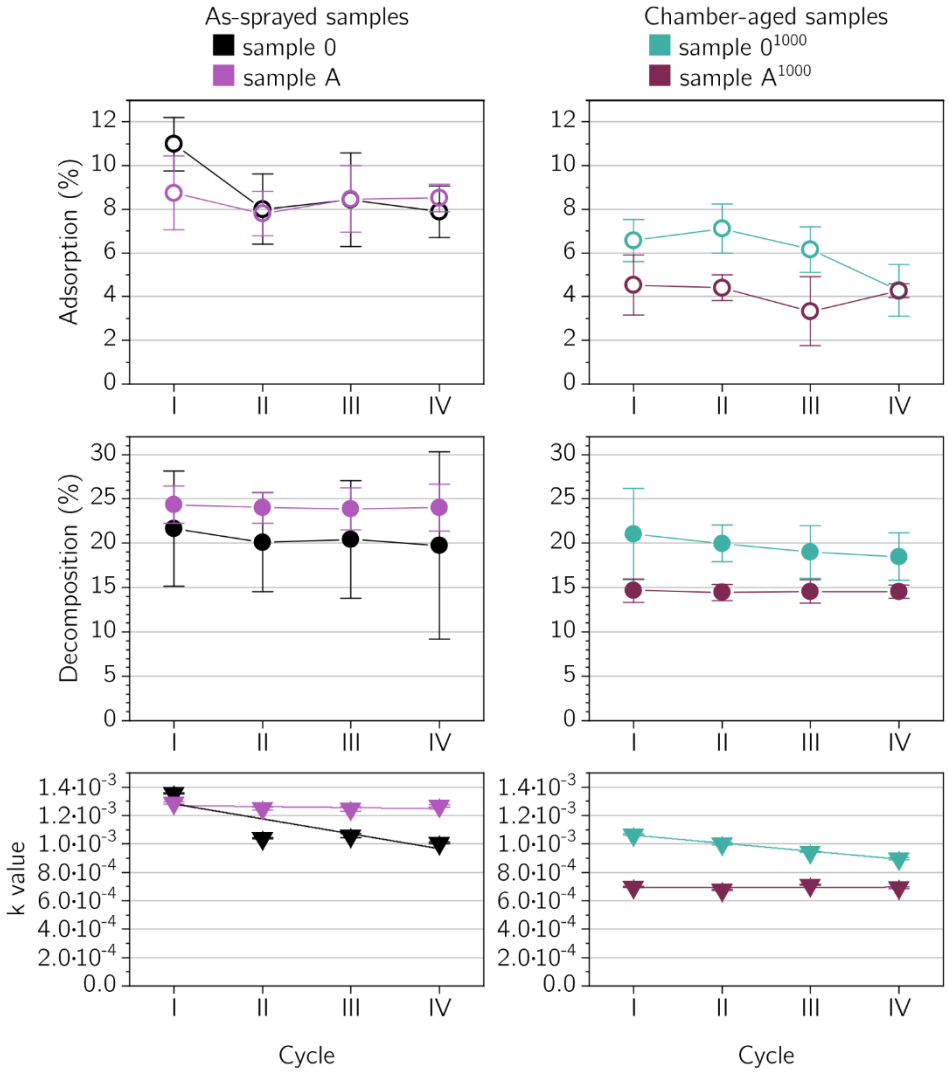

Fig. 4.2.12 the LPCS coatings' photocatalytic performance details in the span of four cycles. At the top is the amount of MB dye adsorbed. In the middle is the amount of the MB dye that is photocatalytically decomposed. At the bottom, the pseudo-1st-order reaction kinetics values for the MB dye photocatalytic decomposition are presented for samples per specific cycle.

The chamber ageing process affects both the adsorption and photocatalytic properties of samples. After ageing, samples 0^{1000} and A^{1000} show reduced adsorption properties compared to as-sprayed samples (Fig. 4.2.12 top, right). Sample 0^{1000} adsorbs around 7% of the dye in the first cycle while sample A^{1000} adsorbs 5%. Similarly, to as-sprayed samples, sample 0^{1000} adsorption slightly drops, while sample A^{1000} adsorption is more or less constant and after

the third cycle, they both reach similar values of 4%. From all the tested samples the best adsorbent is sample 0, then sample A, sample 0^{1000} and sample A^{1000}. The same order is observed for the increasing crystallinity of the samples. Suggesting that the as-sprayed samples' adsorption is connected to their crystallinity, which also affects their specific surface area [225].

The MB decomposition rate for sample 0^{1000}, which is around 19% (Fig. 4.2.12, middle, right) is comparable with the as-sprayed sample 0 (around 20%). On the other hand, the MB decomposition rate for sample A^{1000} (around 15%) is much lower than its as-sprayed equivalent (around 24%). The reaction kinetics of sample 0^{1000} resembles in value the results of as-sprayed sample 0, however, a gradual decrease is observed over four cycles (Fig. 4.2.12, bottom, right). Sample A^{1000}, on the other hand, gives the lowest rate values of the reaction kinetics, which is half of the value recorded for sample A.

Based on the analysed result there are two key distinctions between as-sprayed and chamber-aged coatings that are evident and concern the photocatalysis. It appears that one of the most significant differences in the properties of the coatings is the MB adsorption level. From another perspective, when considering the structural changes that occurred as a result of chamber ageing, the observed decrease in MB dye adsorption may be linked to changes in the coatings' degree of crystallinity. The origin of these differences and their impact on the photocatalytic properties of TiO_2 coatings are discussed below.

The surface properties of the photocatalyst can be affected by their operation conditions. Prolonged exposure to water vapour during the 1000-hour chamber-ageing process can reduce the number of active sites on the photocatalyst surface. As mentioned earlier, the TiO_2 sprayed coatings may have hydroxyl groups attached to titanium ions remaining after synthesis. Those hydroxyl groups can facilitate the adsorption of the MB dye by the electrostatic attraction or electron donor-acceptor interaction [226]. As a result their decrease on the surface , negatively affect adsorption and decomposition efficiency of the photocatalyst [162]. This effect is particularly evident when comparing samples A and A^{1000}. The deactivation of the photocatalyst can result from the MB dye products' presence on the TiO_2 surface [227]. In some cases, 24 hours of UVA exposure in the air is insufficient to fully regenerate

the photocatalyst's active sites [162]. As a result, species deposited on the photocatalyst surface remain there, reducing its adsorption and decomposition performance [227]. Additionally, considering the chamber-ageing is carried out in the humid atmosphere, the water vapour is likely absorbed onto the photocatalyst surface. This in turn may cause the adsorption of ambient CO_2 [162], creating optimal conditions for the carbonate ion formation on the photocatalyst surface. These ions are known to scavenge the hydroxyl radicals, lowering the photocatalyst's effectiveness [228,229].

The crystallinity of the coatings increased after the chamber-ageing process. While greater photocatalytic decomposition efficiency is known to be enhanced in highly crystalline structures [225,230], the chamber-aged samples exhibit reduced photocatalytic effectiveness. The ageing-induced crystallisation of the photocatalysts could decrease the surface area of the coatings' structure, affecting their adsorption capacity and, in turn, their photocatalytic effectiveness. Initially, the cold-sprayed coatings' material consists of amorphous and anatase phases, among which the former has the highest specific surface area [225]. With the increasing crystallinity, the surface area of the structure reduces as the amorphous phase transitions into crystalline. Additionally, the changed phase composition of the chamber-aged coatings might also influence the photocatalytic properties. Brookite presence typically enhances photocatalytic activity due to slightly higher conduction band energy compared to anatase. This allows for electrons to transfer from the brookite to the anatase conduction band. The energy difference between the phases' conduction band energies lowers the chance of electron-hole recombination, improving the photocatalytic process [219,231]. Based on the decomposition and reaction rate constant results the appearance of brookite is not affecting the coatings significantly, as the difference between the sample 0 and 0^{1000} is within the uncertainty range. This suggests that other factors i.e. photocatalyst surface state and morphology have a more significant influence on the photocatalyst effectiveness.

The ageing process is a naturally occurring phenomenon present in all materials and happens during the lifetime of the photocatalyst. The lower values of the adsorption and decomposition for the chamber-aged samples align with the intuition that long-time exposure

of the photocatalyst to the working conditions, which chamber-ageing is meant to simulate, reduces their photocatalytic efficiency. One can thus stipulate that if as-sprayed samples were subjected to many more working cycles, their adsorption and decomposition rates would match those of the chamber-aged samples. The difference is especially visible in the A and A^{1000} samples. Nevertheless, the photocatalytic activity decomposition test results reveal that coatings present different, yet stable (with the uncertainty range) values of reaction kinetics over four cycles for both as-sprayed and chamber-aged samples. This allows one to draw a conclusion that if the regeneration process, such as UV irradiation, is included in the photocatalytic process, the LPCS TiO_2 samples might operate in the 24-hour system (corresponding to the full four-cycle decomposition test) and largely retain their initial properties.

Summary

The chamber-ageing process induces the amorphous coating crystallisation process. Simultaneously, the substrate passivation process leads to oxygen depletion in the TiO_2 matrix, which is also exposed to the abundance of hydroxyl groups (from the penetrating water vapour) shifting the crystallisation process from typically favoured anatase to brookite.

The structural and interfacial changes resulting from the chamber-ageing process affect the coating's mechanical properties. The initially low cohesion values are not affected by the ageing of the samples. On the other hand, two adhesion bonding mechanisms between the LPCS coatings and the aluminium substrate are distinguished - chemical bonding and mechanical interlocking. The main bonding mechanism depends on the initial crystallinity of the coating. For primarily amorphous coatings, the chemical bonding is the main bonding factor, while more crystalline sample A relies more on mechanical interlocking. The chamber ageing has a contrary effect on the coatings; the amorphous coating adhesion is enhanced due to the increased amount of passivation layer-coating bonds established, while for the more crystalline coatings, the adhesion decreases due to reduced interface area, which lowers the mechanical interlocking between the coating and the substrate. Nevertheless, even after ageing, the adhesion strength of the crystalline coating remains twice that of the aged,

amorphous coating. Therefore, for long-term photocatalytic applications, maintaining a high initial crystallinity is essential to ensure superior durability of LPCS-deposited TiO_2 coatings.

The overall photocatalytic decomposition highlights the significance of surface properties in determining the coating performance. The coatings subjected to long-term ageing present adsorption reduction and, in turn, a decrease in both the decomposition level and reaction rate constant. This reduction likely stems from the decreased adsorption capacity due to the dye's products presence on the photocatalyst's surface and reduced surface area of the photocatalyst due to the lower fraction of the amorphous share in the aged coatings. At the same time, the regeneration of the TiO_2 coatings is likely to retain the initial decomposition properties over a four-cycle decomposition test.

4.2.3 Influence of the sol-gel synthesis parameters (solvent choice) on the TiO_2 coatings' structure and properties

In this Section, the effect of the sol-gel-derived TiO_2 powder properties (morphology and self-agglomeration) on the LPCS process and the obtained coating's properties is described. To change the powder's properties, the sol-gel synthesis is modified by varying the solvent. Isopropanol, acetone, and methanol are the chosen solvents, and the resulting powders are denoted TiO_2-IPOH, TiO_2-ACE, and TiO_2-MOH, respectively. Additionally, to spray the samples, parameters previously identified as optimal for achieving the highest adhesion (sample A, described in Section 4.2.1) are used for spraying. The sprayed TiO_2 coatings are marked as A-IPOH, A-ACE, and A-MOH.

The diffraction patterns of the sprayed coatings are presented in Fig. 4.2.13. The diffractograms of the solvent-modified samples are similar to that of sample A described previously. In the diffractograms the anatase phase is present at peaks 25.25°, 37.85°, 48.00°, 53.90°, 55.05°, 62.70°, 68.95° and 70.04° 2theta, the amorphous hump is no longer observable. The Raman spectra of the samples also show bands corresponding to the anatase phase – for samples A-IPOH, A-ACE and A-MOH at 149, 391, 513 and 631 cm^{-1}. In addition, sample A-MOH exhibits weak extra bands at 256, 321, 368, 470 and 546 cm^{-1}, which might be attributed to the presence of brookite [38].

The reference sample A is characterised by the DOC of 37 ± 11%. The sprayed samples A-IPOH, A-ACE and A-MOH have, respectively, crystallinities of 64 ± 15, 30 ± 4 and 26 ± 10%. In the LPCS process, the coating's crystallinity depends greatly on the initial powders' crystallinity and the kinetic energy the particles have upon impact [76]. The analysis of the powder's phase structure reveals that all solvent-modified powders are amorphous, with no clear evidence of any crystalline TiO_2 phase (Section 4.1.2). Assuming that these powders' crystallinities are approximately at the same level, the difference in the coatings' DOC values must result from the kinetic energy that they have upon impact. The main features that condition this energy are the powder's size, morphology and density of the material, as they determine the velocity of entrained particles when exiting the nozzle [66,76].

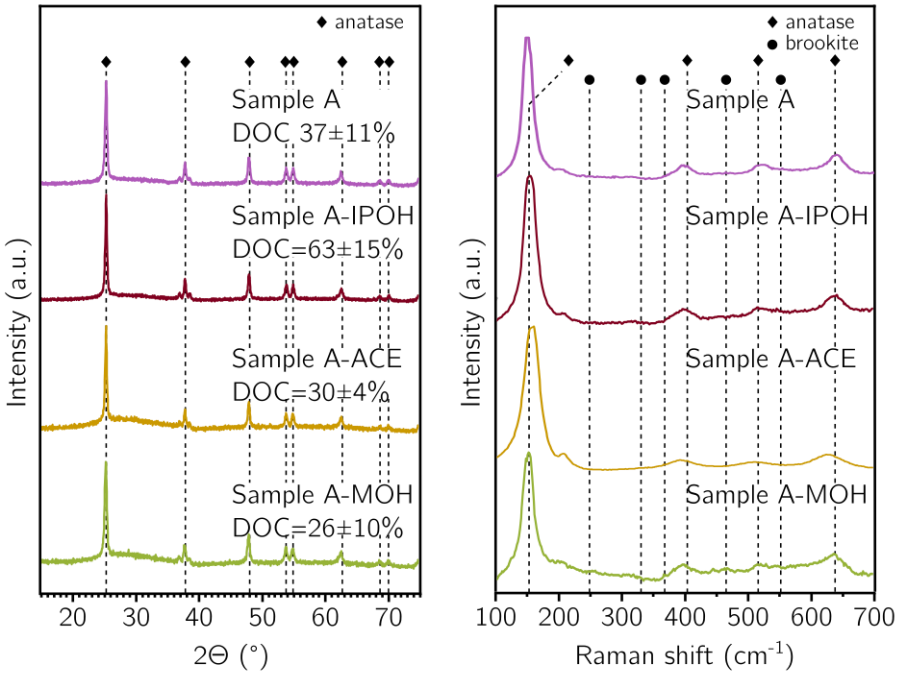

Fig. 4.2.13 On the left there are diffractograms and the *DOC* values of respective coatings, on the right Raman spectra of the low-pressure cold-sprayed samples: A, A-IPOH, A-ACE and A-MOH.

The most significant difference among the powders lies in their particle size distribution (Table 4.2.4). The acetone-based powder is most similar to the non-modified sieved powder. Given the same LPCS deposition conditions, the A-ACE coating's crystallinity closely resembles the non-modified a coating. The methanol-based powder is characterised by a higher fraction of large particles (agglomerates) with a mean diameter of around 85 µm. Experimentally measured in-flight velocities for the TiO_2 agglomerates in the 40-100 µm range indicate a gradual decrease in impact velocity as the particle size increases [193]. Consequently, the impact of larger particles is less intense, resulting in reduced crystallinity in the A-MOH coating compared with coating A. Furthermore, the highest coating crystallinity is observed in the A-IPOH sample. The isopropanol-based powder shows notable differences from the non-modified sieved powder and exhibits two main particle fractions shifted towards coarser size ranges and an elevated proportion of agglomerates, which are removed during the sieving process in the TiO_2-063 powder. It is highly probable that an increase in the agglomerates fraction enhances the efficiency of the LPCS process. The simulations of the hydroxyapatite powder, a different ceramic feedstock deposited via cold spraying, show that particles smaller than 10 µm may be deflected by the bow shock and fail to contribute to the coating's formation

[232]. Although the exact threshold for TiO_2 powder may differ due to the significant density difference between the materials (ρ_{Hap}=0.55 gcm^{-3} [233], $\rho_{TiO2}\approx$4 gcm^{-3} [234]), there is a strong likelihood that very small TiO_2 particles will rebound from the substrate. As a result, an increased proportion of larger agglomerates can lead to intensified fragmentation and deformation upon the high-energy-kinetic impact. This, combined with the strain-induced crystallisation of the amorphous feedstock powder, results in increasing the crystallinity of the A-IPOH coating.

Table 4.2.4 the particle size distribution characteristics of the powders used for spraying coatings A, A-IPOH, A-ACE and A-MOH.

	TiO_2-063	TiO_2-IPOH	TiO_2-ACE	TiO_2-MOH
x_{10} (µm)	1.05	1.15	1.02	1.54
x_{50} (µm)	6.55	11.51	7.27	40.30
x_{90} (µm)	51.10	80.41	80.41	114.74
span	7.64	4.26	10.92	2.81

The cross-sections of the LPCS coatings are presented in Fig. 4.2.14. The microstructures of the coatings resemble the coatings obtained using non-modified powder described in Section 4.2.1. The coatings' structure consists of the crystalline grains embedded into the amorphous matrix. The amount of the visible grains increases towards the coatings-substrate interface. Cavities visible in the coatings' cross-section likely result from the removed grains in the polishing process. The rough substrate is properly coated with the LPCS coatings in all cases (A-IPOH, A-ACE, A-MOH). The pores are present in all solvent-modified coatings; however, it seems that there are fewer in the near-interface area and more of them in the top part of the coatings.

The roughness of the solvent-modified coatings varies depending on the used solvent. The coatings A-IPOH and A-MOH resemble the reference sample A. Coating A-ACE, on the other hand, is characterised by slightly increased surface roughness (Table 4.2.5). In the cold-spray process, powder properties determine its deposition efficiency. When the maximum possible thickness of the coatings is achieved and no further material is being deposited, the tamping and hammering effect can still take place. The tamping effect comprises

the compression of the already deposited material resulting from the impact of subsequent particles [235]. Whereas the hammering effect refers to the deformation or fragmentation of the striking particles, which influence the surface of the obtained coatings, increasing their strength [236].

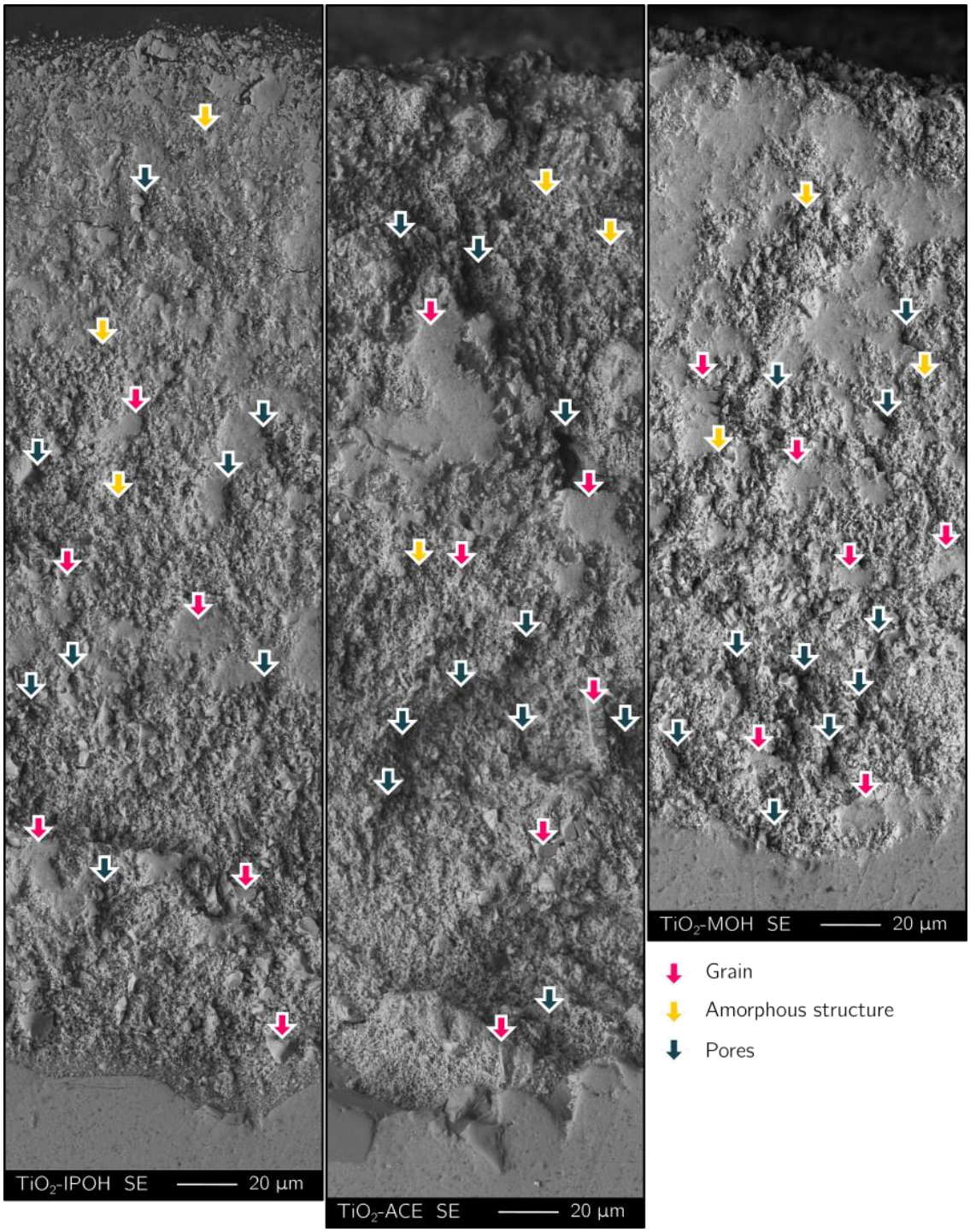

Fig. 4.2.14 the SEM SE images of the cross-section of LPCS coatings: A-IPOH, A-ACE and A-MOH. The coating material is at the top of the picture. While the aluminium substrate is at the bottom. The exemplary characteristic parts of the structure are highlighted with the arrows.

Typically, those effects are not as effective in the case of ceramic materials, as they are when depositing ductile materials like metals; however, in this case, the agglomerates consisting of brittle TiO_2 particles enable the deformation of the system. At the same time particles which do not adhere to the coating will impact and bounce off the surface of the ceramic coatings, smoothening the surface through the erosion process [125]. The powder used for spraying the A-ACE coatings is characterised by the increased share of smaller particles, which may be the reason for the higher roughness of the coatings since the smaller particles will facilitate a less effective surface smoothening process.

Table 4.2.5 Assessed thickness, cohesion and adhesion of the low-pressure cold-sprayed samples A, A-IPOH, A-ACE, and A-MOH. The x is the mean value calculated and the s is the standard deviation.

	A		A-IPOH		A -ACE		A -MOH	
	x	s	x	s	x	s	x	s
R_a (μm)	4.3	1.0	4.23	1.1	4.8	1.2	4.3	0.8
R_z (μm)	25.4	4.8	28.0	5.4	29.8	7.0	29.0	6.0
Thickness (μm)	254	90	322	49	326	120	238	62
Cohesion - L_{c1} (N)	1.2	0.4	0.8	0.3	0.5	0.2	0.8	0.2
Adhesion - L_{c2} (N)	≥30.0*	-	28.3	0.8	25.7	3.2	27.0	2.8

Furthermore, the modification positively influences the deposition efficiency of the isopropanol- and acetone-based powders, leading to increased thickness of the coatings A-IPOH and A-ACE compared to the reference sample A. At the same time, coatings A-ACE and A-MOH are characterised by significantly less consistent thickness results (Table 4.2.5). These inconsistencies are likely due to the distinct particle size distributions of the powders: A-ACE powder contains a higher proportion of fine particles, whereas A-MOH is dominated by large agglomerates. In the cold spray process, such inconsistencies often arise from incompatibilities between the powder characteristics and the cold spray unit's powder feeder [22]. Specifically, powders with poor flowability or unsuitable particle size distributions can disrupt the continuity of powder feeding, resulting in highly inhomogeneous coatings [237].

By contrast, the A-IPOH coating exhibits both the greatest mean thickness and the lowest variance, likely because, compared to the reference sieved powder – TiO_2-063 – it is characterised by a slightly increased agglomerate fraction, which can improve powder flowability and ensure uninterrupted feeding during deposition.

The results of the scratch testing of the solvent-modified coatings are presented in (Table 4.2.5). The solvent modification of the TiO_2 powder has not improved the cohesion of the obtained LPCS coatings, which remain brittle and are characterised by poor cohesive strength [188]. The coatings' surface characteristic damage is shown in Fig. 4.2.15, left column. In the small loads range the chipping of the coatings is observed, and with the load increase, the cohesive failure takes the form of arc-shaped cracks, visible only in the scratch track (Fig. 4.2.15, middle column). The cohesive failure is 1.2 ± 0.4, 0.8 ± 0.3, 0.5 ± 0.2, and 0.8 ± 0.2 for coatings A, A-IPOH, A-ACE and A-MOH, respectively. Further damage progression involves a through-thickness cracking of the coatings, observed only in the scratch-crack. Afterwards, the conformal cracking of the coatings can be observed, which finally evolves into buckle spallation, and in the case of all solvent-modified coatings, the adhesive failure can be observed. Additionally, for the A-ACE coating, the buckle spallation extends out of the scratch track (Fig. 4.2.16). Compared to the reference sample A, which adhesive strength exceeded the maximum load of the unit (30 N) the adhesive strength of the solvent-modified coatings decreased, giving the results of 28.3 ± 0.8 N, 25.7 ± 3.2 N, and 27.0 ± 2.8 N, for A-IPOH, A-ACE, and A-MOH, respectively.

The changes in adhesion of the solvent-modified coatings result from differences in powder morphology at both micro- and macro-scales, namely, the surface texture of primary particles and the size of their agglomerates. Compared to the non-modified powder, the solvent-modified powders are synthesised at an increased pH value. When comparing the characteristics of non-sieved initial TiO_2-0 and TiO_2-IPOH powders (Table 4.2.4) – synthesis conditions only varied in the pH– there is an observable increase of the large particles fraction.

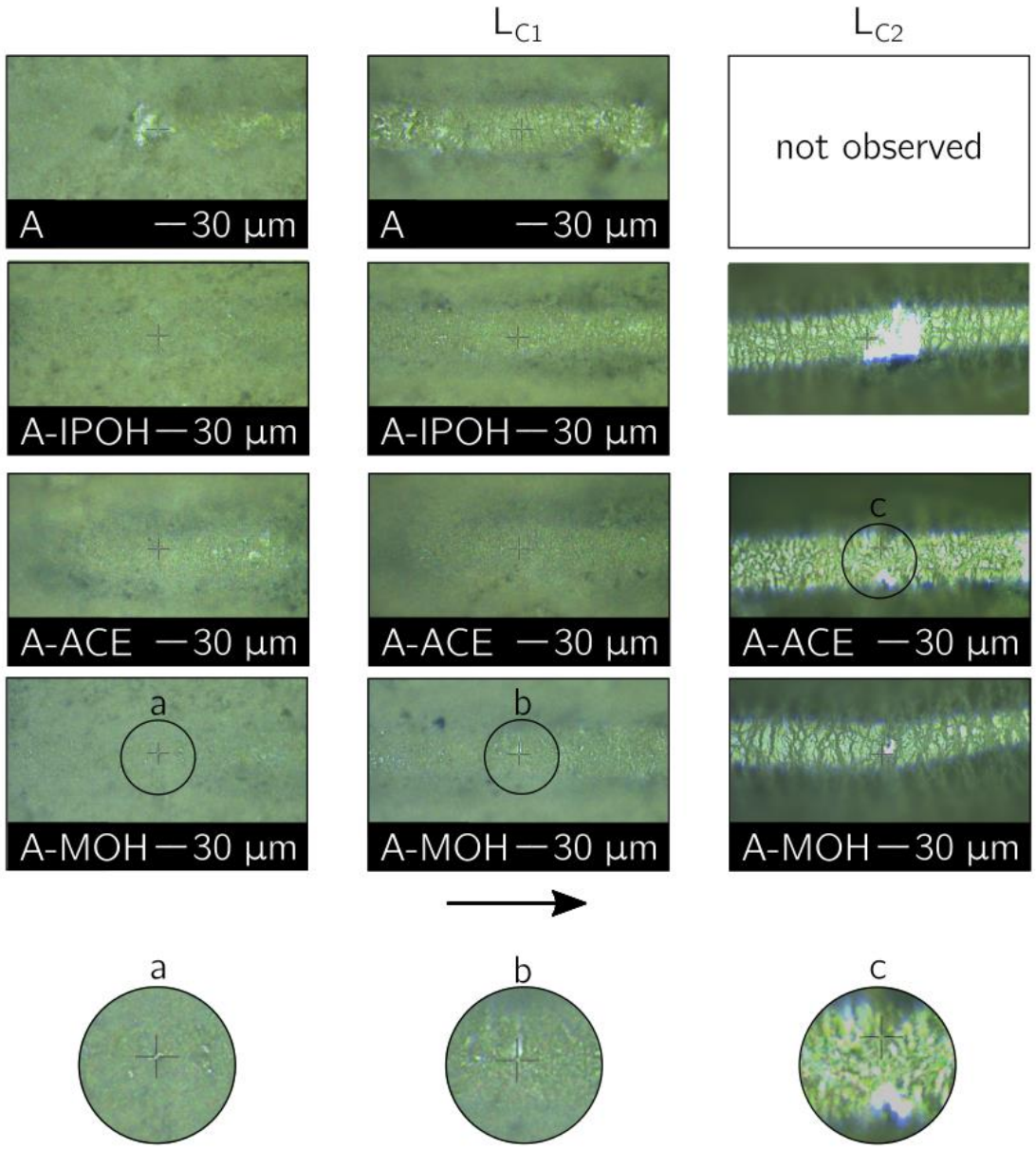

Fig. 4.2.15 The optical micrographs of the surface damage caused by scratch-testing of the LPCS TiO_2 samples A, A-IPOH, A-ACE, and A-MOH. The left column presents the small load's damage, the middle column presents cohesive failure (L_{c1}), right column presents adhesive failure (L_{c2}). The load is progressing from left to right (following the black arrow at the bottom).

This suggests that increasing the pH may yield larger agglomerate particles. The pH sol-gel synthesis increase enhances the effect of the repulsion between the titania species, retarding the crystallisation process and yielding smaller particles with more developed surfaces [238,239]. These textured particles subsequently agglomerate, and omitting the sieving step leaves the largest agglomerates intact. The coatings sprayed out of the solvent-modified powders are characterised by a reduced strength of the coating material (represented by both

cohesion and adhesion). According to Herring's law, the increase in the surface area of the powder particles comprising the bulk material makes the sintering process less effective. Cold-spraying of powdered materials involves generating deformation-induced heat. This increase of temperature is responsible for strengthening the bonding of the adjacent particles; however, for the more developed interfaces, the process is less effective [240]. Which suggests that the sieving process has a positive influence on the strength of the coatings and should be applied in order to increase the strength of the sprayed coatings material.

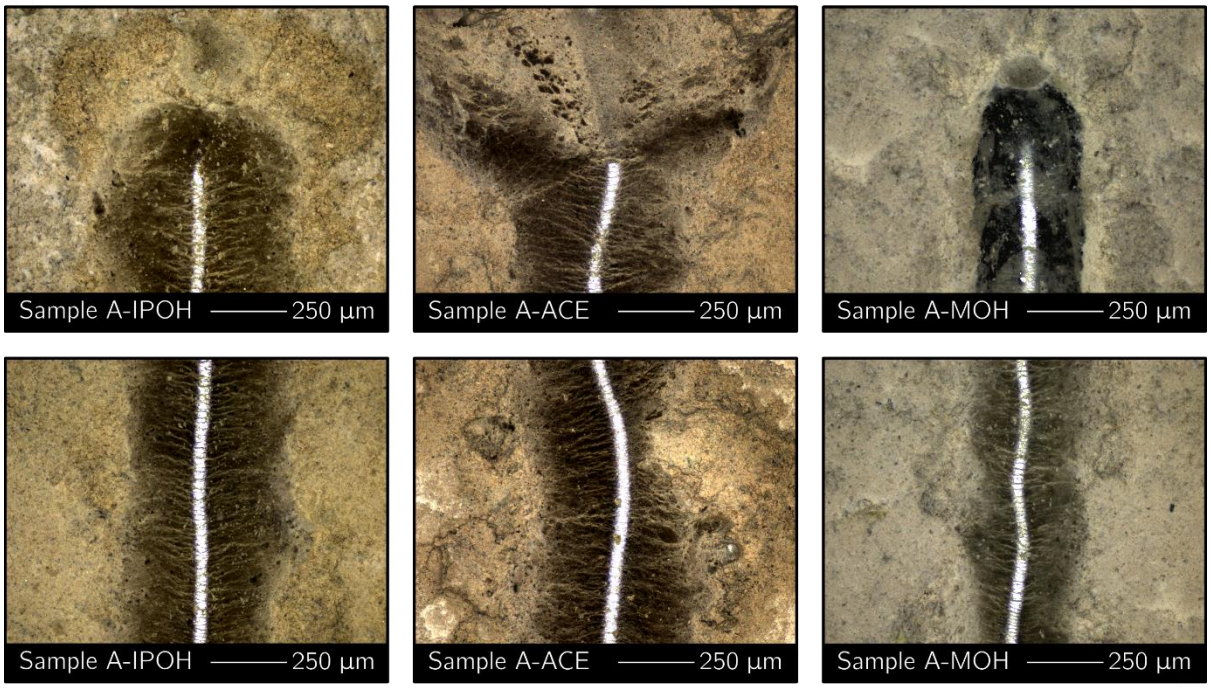

Fig. 4.2.16 Optical micrographs of the LPCS solvent-modified TiO_2 coatings. The view presents the top surface of the coatings after the scratch-testing examination.

The band gap value of the reference sample A is 3.18 eV. The band gap values of the solvent-modified coatings are 3.07 eV, 3.10 eV, and 3.18 eV for A-IPOH, A-ACE, and A-MOH, respectively, the isopropanol and acetone powders shifted towards smaller values (Fig. 4.2.17). Moreover, the absorption of the solvent-modified coatings also has changed; the highest absorption is still in the UVA range. However in the case of the A-ACE and A-IPOH powders, there is an improvement in the absorption of the coating in the visible range wavelength. The best absorption is observed for the A-ACE coating. These variations in optical properties are likely influenced by differences in crystallite size, as smaller crystallites can lead

to band gap narrowing [241]. Furthermore, the polarity of the solvents used in the sol-gel process affects the hydrolysis and condensation rates, thereby influencing the crystallite size, which also can affect the optical properties of the resulting TiO_2 coatings [242]. In some cases, the visible light activity is attributed to the presence of trace amounts of Ti^{3+} species introduced during high-pH synthesis. At elevated pH, strong electrostatic repulsion among the titania species can generate structural defects, some of which facilitate the partial reduction of Ti^{4+} to Ti^{3+} extending the activity range of the sprayed coatings [238].

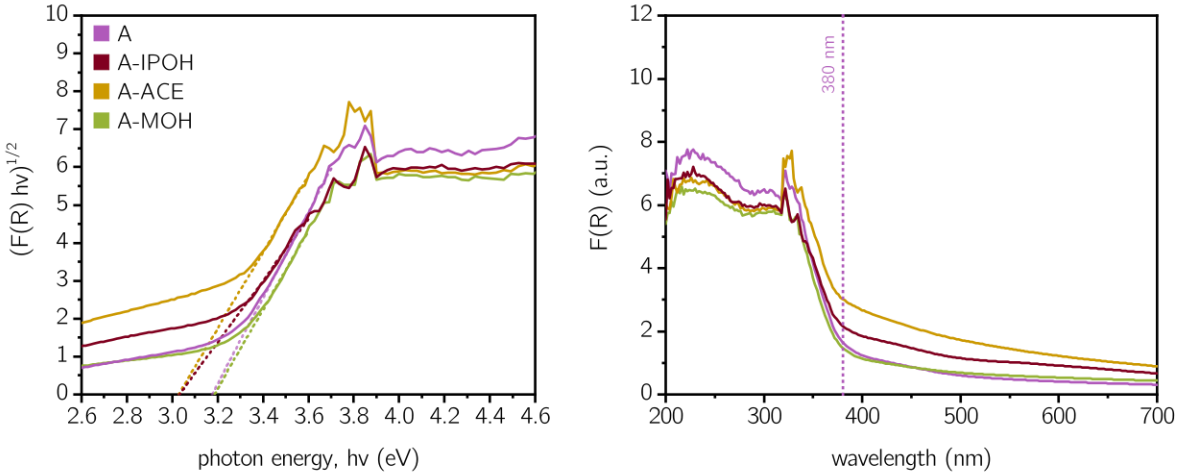

Fig. 4.2.17 On the left the Tauc plots were used to determine the band gap energy values for the A, A-IPOH, A-ACE, and A-MOH coatings; on the right, the Kubelka-Munk function plot A, A-IPOH, A-ACE, and A-MOH coatings presenting their adsorption band.

The photocatalytic properties of the solvent-modified coatings differ from those of the reference sample A. The adsorption capacity of sample A is 8.7%, whereas the modified samples exhibit subtly lower adsorption values: 4.9% for A-IPOH, 6.0% for A-MOH, and 7.1% for A-ACE (Fig. 4.2.18). Furthermore, the solvent-modified coatings demonstrate lower photocatalytic degradation efficiencies: 16.0% for A-IPOH, 14.5% for A-MOH, and 20.9% for A-ACE, compared to 24.4% for the reference sample A. This reduction in degradation efficiency correlates with the decreased adsorption capacities, suggesting that the adsorption properties of the coatings play a significant role in its subsequent photocatalytic degradation.

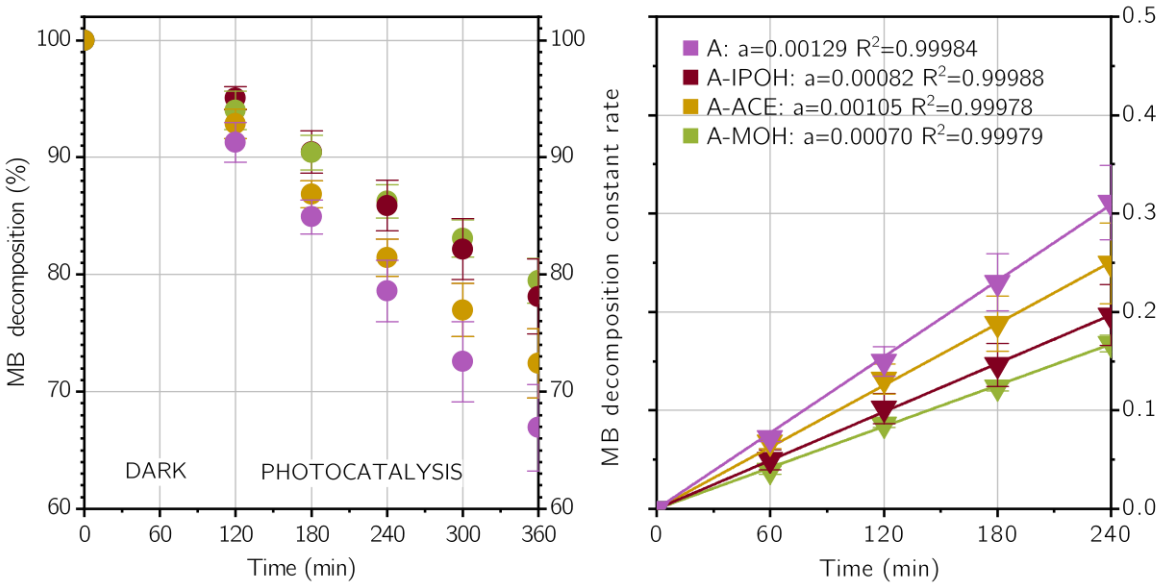

Fig. 4.2.18 On the left, MB dye adsorption and decomposition in the presence of samples: A, A-IPOH, A-ACE, and A-MOH. DARK refers to the conditioning time of the samples – carried out in the darkness, PHOTOCATALYSIS represents the process part of the process when the UVA lamp was on and the photocatalytic decomposition is conducted; on the right, the pseudo-first-order kinetics and reaction rate constant for the MB degradation process for samples: A, A-IPOH, A-ACE, and A-MOH.

The adsorption capacity of the photocatalyst is largely determined by its surface characteristics [54], which in turn reflect the morphology of the sprayed powders. Therefore, powder agglomeration may determine the surface properties of the deposited coatings. The used powders' particle size increases in the order: TiO_2-ACE < TiO_2-IPOH < TiO_2-MOH. Accordingly, A-ACE—deposited from the finest powder—achieves the highest methylene blue degradation rate, consistent with its larger surface area. A-IPOH, derived from mid-sized particles, exhibits intermediate activity, while A-MOH, prepared from the coarsest powder, shows the lowest degradation efficiency [82]. Additionally, powders present slightly lower effectiveness compared to the reference coating A, which is fabricated using the finest (sieved) powder, likely increasing the coating's surface area.

Summary

The solvent-modification of the TiO_2 powders results in the shift in powders particle size distribution, which strongly influences low-pressure cold spray process deposition and the coatings' properties. The coating crystallinity depends primarily on the kinetic energy of particles upon impact, which is conditioned by the particles size. A-IPOH exhibits

the highest crystallinity due to its optimised feedstock size, while A-ACE and A-MOH, in contrast, contain excessive fine and coarse fractions, respectively, and experience in-flight deceleration, obtaining lower kinetic energy and resulting in less crystalline coatings.

The solvent modification of the initial TiO_2 powders affects the deposition efficiency of the LPCS process. Compared to the unmodified sieved powder, the acetone- and isopropanol-based powders show an increase in the thickness of the sprayed coatings. At the same time, acetone- and methanol-based powders which are excessively fine or coarse, yield coatings with thicknesses characterised by large result variability. Due to the high variability of the acetone-based coating, the high thickness results should be regarded with caution. On the contrary, the A-IPOH coating is characterised by the lowest variability of the mean thickness value, which is likely due to the increased amount of agglomerates that facilitates better powder feeding.

On the other hand, the surface roughness of the solvent-modified coatings changes only marginally: A-IPOH and A-MOH remain comparable to the reference, while A-ACE shows a slight increase, likely due to its smaller average particle size.

The mechanical properties of the solvent-modified coatings decrease slightly, likely due to the larger surface area of modified powders particles which hinders sintering between splats during the coating material formation. Additionally, the modification has a marginal effect on the cohesion of the coatings. On the other hand, using the sieved TiO_2 powders may contribute to the increase of the coating's adhesion by facilitating more effective sintering process of the sprayed splats.

Optical and photocatalytic properties vary among the modified coatings: band gaps for A-IPOH and A-ACE are reduced relative to the reference sample A, which may be caused by their crystallites reduced sizes, whereas A-MOH resembled the non-modified sample A. Notably, the isopropanol-based and acetone-based coatings exhibit slightly enhanced visible-light absorption. However, overall photocatalytic efficiency has not improved. Based on the coating's performance, it seems that the powder's morphology and agglomeration played a key role in the overall photocatalytic performance.

5 Conclusions

This thesis investigates low-pressure cold-sprayed (LPCS) TiO_2 photocatalytic coatings, focusing on feedstock powder synthesis via the sol-gel method, deposition parameters and the evaluation of their photocatalytic performance and stability.

Section 1 presents a broader context of unconventional water-remediation methods, particularly photocatalysis, and identifies gaps in scalable deposition techniques. Section 2 reviews the fundamentals of photocatalysis and TiO_2 as a photocatalyst, discusses various deposition methods with emphasis on LPCS, and outlines photocatalytic testing methodologies. Section 3 details the experimental procedures: sol–gel synthesis of TiO_2 powders, LPCS deposition, and photocatalytic properties assessment and characterisation techniques, for example, SEM, Raman spectroscopy, and XRD.

In Section 4.1 the results of the sol-gel syntheses of the TiO_2 material for the LPCS process spraying are presented. The sol-gel-derived TiO_2 powders are shown to be initially amorphous with a bimodal size distribution of primary particles and their agglomerates. The powders are sieved after the synthesis, which removes larger agglomerates. Solvent modification (isopropanol, acetone, methanol) alters agglomeration behaviour via differences in alkyl-chain length, polarity and proticity. Isopropanol-based modification, where only pH is increased, produces powders the most similar to the reference. Acetone-based synthesis yields an increased fraction of finer particles. Methanol-based synthesis also enables obtaining an increased amount of smaller particles fraction; however, due to its protic character the primary particles agglomerate more effectively than in acetone, making the agglomerate fraction the dominant one. To study the effect of the agglomerates on their deposition process, the powders are not sieved.

In Section 4.2., the characterisation of the LPCS TiO_2 coatings obtained from the synthesised powders is presented. By varying LPCS process parameters, such as scanning step, number of layers and traverse speed, coatings with partially crystallised (amorphous-anatase) structures are produced. Their crystallinity increases with the uninterrupted spraying

time. Among the tested variables which impact the spraying time, the scanning step has the greatest influence on coatings' properties: decreasing it increases thickness, density and adhesion and smooths out surfaces. Adding layers increases roughness without altering other properties. Traverse speed showed no clear effect. The obtained results show that through proper parameter selection of the LPCS process, it is possible to customise the coating key properties like phase structure, thickness, roughness and adhesion. From the samples investigated in this part, two coatings – one reference and one with the highest adhesion – are selected for further study.

In the subsequent part of this Section the long-term stability of the selected coatings is assessed using chamber ageing and multi-cycle photocatalytic decomposition tests. Ageing in a humidity chamber promotes further crystallisation and initiated passivation of the aluminium substrate via water infiltration. The passivation layer draws oxygen from TiO_2 coating, shifting the crystallisation pathway from anatase to brookite, ultimately yielding amorphous-anatase-brookite structures. These changes have minimal effect on coating cohesion but significantly impact adhesion strength. Initially, two adhesion mechanisms are proposed – chemical bonding in coatings with dominant amorphous fraction in the structure and mechanical interlocking in coatings with increased crystallinity. These two respond differently to ageing: chemical bonding is strengthened by passivation, while mechanical interlocking is weakened by grain encapsulation. Nevertheless, coatings with increased crystalline share retain twice the adhesion of aged amorphous samples, suggesting that higher crystallinity of the TiO_2 structure prolongs lifetime. Photocatalytic tests highlight the need for photocatalyst regeneration: long-term aged coatings show reduced adsorption and activity, whereas when subjected to cycle testing with regeneration between the cycles, the coatings maintain stable performance. Amorphous coatings demonstrated higher adsorption, while crystalline coatings exhibited more stable and efficient decomposition. These results suggest that photocatalytic process design should include the periodic regeneration (e.g., UV irradiation) of the photocatalyst, granting increased longevity and more effective long-term operation.

In the final part of this Section, the influence of TiO_2 solvent-modified feedstock powders agglomeration on the LPCS deposition process and resulting coatings is analysed. The powder agglomeration is conditioned by the used solvent: isopropanol-based powder yields the best mechanical and photocatalytic results; acetone and methanol powders produce coatings with high thickness variability. This results from the powders inadequate agglomerate sizes, which make the deposition process unstable, possibly due to reduced kinetic energy of either the too large or too small agglomerate sizes. Moreover, comparing the solvent-modified- and sieved-powder-derived coatings, the increased mechanical properties of the latter suggest that limiting the size of agglomerates aids the mechanical properties of the coatings. What is more, isopropanol- and acetone-based coatings show slight activity in the visible light range. However, the overall photocatalytic performance of the solvent-modified coatings is not improved. Based on the coating's performance, it seems that the powder's morphology and agglomeration played a key role in determining their photocatalytic activity. These findings show the complex interplay of the TiO_2 feedstock material synthesis and kinetic deposition process, at the same time showing a premise of a wide range of material customisation, assuming that the parameters of both processes are carefully chosen. Additionally, particle size distribution analysis of solvent-modified powders suggests that employing powders with a narrow size distribution (low span) could improve deposition efficiency and coating strength. This aligns with the observed high thickness variance in coatings derived from powders with either too fine or too coarse particles' sizes, reinforcing the need for precise control of the feedstock in LPCS applications.

This thesis contributes to the advancement of scalable, non-conventional photocatalyst manufacturing routes by providing a systematic understanding of the adhesion mechanisms between the oxide coating and metallic substrate, photocatalyst longevity, and the changes these systems undergo when subjected to the long-term and multi-cycle ageing processes. This work lays the foundation for future studies of the photocatalyst obtained with sol-gel-derived TiO_2 feedstock powder and immobilised via the LPCS process and pinpoints further research

directions in this field, such as increasing the coating material integrity, i.e. cohesion and extending activity into the visible-light spectrum.

List of figures

List of tables

References

1. He C, Liu Z, Wu J, Pan X, Fang Z, Li J, et al. Future global urban water scarcity and potential solutions. Nat Commun. 2021;12(1):1–11.
2. Sikder M, Wang C, Yao X, Huai X, Wu L, KwameYeboah F, et al. The integrated impact of GDP growth, industrialization, energy use, and urbanization on CO2 emissions in developing countries: Evidence from the panel ARDL approach. Sci Total Environ. 2022;837(May):155795.
3. Haseena M, Javed A, Malik MF, Arshad S, Asif N, Zulfiqar S, et al. Water Pollution and Human Health. 2017;1(3):16–9.
4. Osman AI, Elgarahy AM, Eltaweil AS, Abd El-Monaem EM, El-Aqapa HG, Park Y, et al. Biofuel production, hydrogen production and water remediation by photocatalysis, biocatalysis and electrocatalysis. Vol. 21, Environmental Chemistry Letters. Springer International Publishing; 2023. 1315–1379 p.
5. Jiménez S, Micó MM, Arnaldos M, Medina F, Contreras S. State of the art of produced water treatment. Chemosphere. 2018;192:186–208.
6. Long Z, Li Q, Wei T, Zhang G, Ren Z. Historical development and prospects of photocatalysts for pollutant removal in water. J Hazard Mater. 2020;395(March):122599.
7. Wang H, Li X, Zhao X, Li C, Song X, Zhang P, et al. A review on heterogeneous photocatalysis for environmental remediation: From semiconductors to modification strategies. Chinese J Catal. 2022;43(2):178–214.
8. Ahmed SN, Haider W. Heterogeneous photocatalysis and its potential applications in water and wastewater treatment: a review. Nanotechnology. 2018;29(34).
9. Ge J, Zhang Y, Heo YJ, Park SJ. Advanced design and synthesis of composite photocatalysts for the remediation of wastewater: a review. Vol. 9, Catalysts. 2019.
10. Horikoshi S, Serpone N. Can the photocatalyst TiO2 be incorporated into a wastewater treatment method? Background and prospects. Catal Today. 2020 Jan;340(August 2018):334–46.
11. Loeb SK, Alvarez PJJ, Brame JA, Cates EL, Choi W, Crittenden J, et al. The Technology Horizon for Photocatalytic Water Treatment: Sunrise or Sunset? Environ Sci Technol. 2019 Mar 19;53(6):2937–47.
12. Guo Q, Zhou C, Ma Z, Yang X. Fundamentals of TiO2 Photocatalysis: Concepts, Mechanisms, and Challenges. Adv Mater. 2019;31(50):1–26.
13. Gonçalves MC, Pereira JC, Matos JC, Vasconcelos HC. Photonic band gap and bactericide performance of amorphous sol-gel titania: an Alternative to crystalline TiO 2. Molecules. 2018;23(7).
14. Haggerty JES, Schelhas LT, Kitchaev DA, Mangum JS, Garten LM, Sun W, et al. High-fraction brookite films from amorphous precursors. Sci Rep. 2017;7(1).
15. Reyes-Coronado D, Rodríguez-Gattorno G, Espinosa-Pesqueira ME, Cab C, De Coss R, Oskam G. Phase-pure TiO2 nanoparticles: Anatase, brookite and rutile. Nanotechnology. 2008;19(14).
16. Hurum DC, Gray KA, Rajh T, Thurnauer MC. Recombination pathways in the degussa P25

formulation of TiO 2: Surface versus lattice mechanisms. J Phys Chem B. 2005;109(2):977–80.

17. Sun S, Song P, Cui J, Liang S. Amorphous TiO2 nanostructures: Synthesis, fundamental properties and photocatalytic applications. Vol. 9, Catalysis Science and Technology. 2019. p. 4198–215.

18. Mills A, Lepre A, Elliott N, Bhopal S, Parkin IP, O'Neill SA. Characterisation of the photocatalyst Pilkington Activ™: a reference film photocatalyst? J Photochem Photobiol a Chem. 2003;160(3):213–24.

19. Dong H, Zeng G, Tang L, Fan C, Zhang C, He X, et al. an overview on limitations of TiO2-based particles for photocatalytic degradation of organic pollutants and the corresponding countermeasures. Water Res. 2015;79:128–46.

20. Toma FL, Bertrand G, Chwa SO, Meunier C, Klein D, Coddet C. Comparative study on the photocatalytic decomposition of nitrogen oxides using TiO2 coatings prepared by conventional plasma spraying and suspension plasma spraying. Surf Coatings Technol. 2006;200(20–21):5855–62.

21. Bozorgtabar M, Rahimipour M, Salehi M. Novel photocatalytic TiO2 coatings produced by HVOF thermal spraying process. Mater Lett. 2010;64(10):1173–5.

22. Vilardell AM, Cinca N, Dosta S, Cano IG, Guilemany JM. Feasibility of using low pressure cold gas spray for the spraying of thick ceramic hydroxyapatite coatings. Vol. 16, International Journal of Applied Ceramic Technology. 2019. p. 221–9.

23. Salim NT, Yamada M, Nakano H, Shima K, Isago H, Fukumoto M. The effect of post-treatments on the powder morphology of titanium dioxide (TiO2) powders synthesized for cold spray. Vol. 206, Surface and Coatings Technology. 2011. p. 366–71.

24. Rahim TA, Takahashi K, Yamada M, Fukumoto M. Effect of powder calcination on the cold spray titanium dioxide coating. Mater Trans. 2016;57(8):1345–50.

25. Nur ASM, Sultana M, Mondal A, Islam S, Robel FN, Islam A, et al. A review on the development of elemental and codoped TiO2 photocatalysts for enhanced dye degradation under UV–vis irradiation. J Water Process Eng. 2022;47(February):102728.

26. Baszczuk A, Jasiorski M, Winnicki M. Low-Temperature Transformation of Amorphous Sol–Gel TiO2 Powder to Anatase During Cold Spray Deposition. J Therm Spray Technol. 2018;27(8):1551–62.

27. Zhao Y, Niu Z, Zhao J, Xue L, Fu X, Long J. Recent Advancements in Photoelectrochemical Water Splitting for Hydrogen Production. Vol. 6, Electrochemical Energy Reviews. Springer Nature Singapore; 2023. 1–46 p.

28. Tan HL, Abdi FF, Ng YH. Heterogeneous photocatalysts: an overview of classic and modern approaches for optical, electronic, and charge dynamics evaluation. Chem Soc Rev. 2019;48(5):1255–71.

29. Zhang J, Tian B, Wang L, Xing M, Lei J. Photocatalysis. Singapore: Springer Singapore; 2018. 409 p. (Lecture Notes in Chemistry; vol. 100).

30. Zelekew OA, Wang Z, Gu Y, Wu Y nan. Recent progress on photoactive heterogeneous photocatalysts for the degradation of Per-and Polyfluoroalkyl Substances (PFAS): Mechanisms, DFT calculations, limitations, and future prospects. J Environ Chem Eng. 2024;12(5):113323.

31. Abdullah AZ, Haider AJ, Jabbar AA. Preparation of TiO2 nano-thin films by pulsed laser deposition: a review. In: AIP Conference Proceedings. 2022. p. 020092.

32. Rahimi N, Pax RA, Gray EMA. Review of functional titanium oxides. I: TiO2 and its modifications. Prog Solid State Chem. 2016;44(3):86–105.

33. Zhang L, Ran J, Qiao S-Z, Jaroniec M. Characterization of semiconductor photocatalysts. Chem Soc Rev. 2019;48(20):5184–206.

34. Jaiswal R, Bharambe J, Patel N, Dashora A, Kothari DC, Miotello A. Copper and Nitrogen co-doped TiO2 photocatalyst with enhanced optical absorption and catalytic activity. Appl Catal B Environ. 2015;168–169:333–41.

35. Coronado JM, Hernández-Alonso MD. The keys of success: TiO2 as a benchmark photocatalyst. Vol. 71, Green Energy and Technology. 2013. 85–101 p.

36. Paul KK, Giri PK. Shape Tailored TiO 2 Nanostructures and Their Hybrids for Advanced Energy and Environmental Applications: a Review. J Nanosci Nanotechnol. 2018;19(1):307–31.

37. Wei Y, Wu Q, Meng H, Zhang Y, Cao C. Recent advances in photocatalytic self-cleaning performances of TiO2-based building materials. RSC Adv. 2023;13(30):20584–97.

38. Di Paola A, Bellardita M, Palmisano L. Brookite, the least known TiO2 photocatalyst. Vol. 3, Catalysts. 2013. 36–73 p.

39. Luttrell T, Halpegamage S, Tao J, Kramer A, Sutter E, Batzill M. Why is anatase a better photocatalyst than rutile? - Model studies on epitaxial TiO2 films. Sci Rep. 2015;4:1–8.

40. Kovačič Ž, Likozar B, Huš M. Electronic properties of rutile and anatase TiO2 and their effect on CO2 adsorption: a comparison of first principle approaches. Fuel. 2022;328(February).

41. Zhu X, Han S, Feng W, Kong Q, Dong Z, Wang C, et al. The effect of heat treatment on the anatase-rutile phase transformation and photocatalytic activity of Sn-doped TiO2 nanomaterials. RSC Adv. 2018;8(26):14249–57.

42. Esch TR, Gadaczek I, Bredow T. Surface structures and thermodynamics of low-index of rutile, brookite and anatase - a comparative DFT study. Appl Surf Sci. 2014;288:275–87.

43. Lee S-Y, Park S-J. TiO2 photocatalyst for water treatment applications. J Ind Eng Chem. 2013 Nov;19(6):1761–9.

44. Nakata K, Fujishima A. TiO2 photocatalysis: Design and applications. J Photochem Photobiol C Photochem Rev. 2012 Sep;13(3):169–89.

45. Melcher J, Feroz S, Bahnemann D. Comparing photocatalytic activities of commercially available iron-doped and iron-undoped aeroxide TiO2 P25 powders. J Mater Sci. 2017;52(11):6341–8.

46. (2025.04.05) Who are the top ten TiO2 manufacturers worldwide? [Internet]. Available from: https://titantio2.com/top-ten-tio2-manufacturers/

47. (2025.04.05) Chemical Free Photo-Catalytic Process [Internet]. Available from: https://www.purifics.com/photo-cat

48. Wood D, Shaw S, Cawte T, Shanen E, Van Heyst B. an overview of photocatalyst immobilization methods for air pollution remediation. Chem Eng J. 2020 Jul;391(November 2019):123490.

49. Shan AY, Ghazi TIM, Rashid SA. Immobilisation of titanium dioxide onto supporting materials in heterogeneous photocatalysis: a review. Appl Catal a Gen. 2010;389(1–2):1–8.

50. Dunnill CWH, Aiken ZA, Pratten J, Wilson M, Morgan DJ, Parkin IP. Enhanced photocatalytic activity under visible light in N-doped TiO2 thin films produced by APCVD preparations using t-butylamine as a nitrogen source and their potential for antibacterial films. J Photochem Photobiol a Chem. 2009;207(2–3):244–53.

51. Nolan MG, Pemble ME, Sheel DW, Yates HM. One step process for chemical vapour deposition of titanium dioxide thin films incorporating controlled structure nanoparticles. Thin Solid Films. 2006;515(4):1956–62.

52. Balbuena J, Carraro G, Cruz M, Gasparotto A, Maccato C, Pastor A, et al. Advances in photocatalytic NOx abatement through the use of Fe2O3/TiO2 nanocomposites. RSC Adv. 2016;6(78):74878–85.

53. Sun L, Yuan G, Gao L, Yang J, Chhowalla M, Gharahcheshmeh MH, et al. Chemical vapour deposition. Nat Rev Methods Prim. 2021;1(1).

54. Navidpour AH, Xu B, Ahmed MB, Zhou JL. Immobilization of TiO2 and ZnO by facile surface engineering methods to improve semiconductor performance in photocatalytic wastewater treatment: a review. Mater Sci Semicond Process. 2024;179(April).

55. Ichou H, Arrousse N, Berdimurodov E, Aliev N. Exploring the Advancements in Physical Vapor Deposition Coating: a Review. J Bio- Tribo-Corrosion. 2024 Mar 15;10(1):3.

56. Lu Y, Guan S, Hao L, Yoshida H. Review on the photocatalyst coatings of TiO 2 : Fabrication by mechanical coating technique and its application. Coatings. 2015;5(3):425–64.

57. Nizard H, Kosinova ML, Fainer NI, Rumyantsev YM, Ayupov BM, Shubin Y V. Deposition of titanium dioxide from TTIP by plasma enhanced and remote plasma enhanced chemical vapor deposition. Surf Coatings Technol. 2008;202(17):4076–85.

58. Moore B, Asadi E, Lewis G. Deposition Methods for Microstructured and Nanostructured Coatings on Metallic Bone Implants: a Review. Adv Mater Sci Eng. 2017;2017:1–9.

59. Schubert M, Hanft D, Nazarenus T, Exner J, Nieke P, Glosse P, et al. Powder aerosol deposition method - novel applications in the field of sensing and energy technology. Funct Mater Lett. 2019;12(5):1–12.

60. Azina C, Eklund P. Effects of temperature and target power on the sputter-deposition of (Ti,Zr)n+1AlCn MAX-phase thin films. Results Mater. 2021;9(November 2020):7–10.

61. Mehta A, Vasudev H. Advancements in ceramic-coated metals: Enhancing thermal spray coatings for improved performance in aerospace applications using surface treatments. Results in Surfaces and Interfaces. 2025 Jan;18(December 2024):100387.

62. Singh L, Chawla V, Grewal JS. A Review on Detonation Gun Sprayed Coatings. J Miner Mater Charact Eng. 2012;11(03):243–65.

63. Smith MF. Comparing cold spray with thermal spray coating technologies. In: the Cold Spray Materials Deposition Process. Elsevier; 2007. p. 43–61.

64. Tejero-Martin D, Rezvani Rad M, McDonald A, Hussain T. Beyond Traditional Coatings: a Review on Thermal-Sprayed Functional and Smart Coatings. Vol. 28, Journal of Thermal

Spray Technology. Springer US; 2019. 598–644 p.

65. Oksa M, Turunen E, Suhonen T, Varis T, Hannula S-P. Optimization and Characterization of High Velocity Oxy-fuel Sprayed Coatings: Techniques, Materials, and Applications. Coatings. 2011 Sep 2;1(1):17–52.

66. Tregenza O, Hutasoit N, Palanisamy S, Hulston C. Air-based cold spray: an advanced additive manufacturing technique for functional and structural applications. Int J Adv Manuf Technol. 2025 Feb 6;136(11–12):4677–714.

67. Gadow R, Killinger A, Rauch J. New results in High Velocity Suspension Flame Spraying (HVSFS). Surf Coatings Technol. 2008 Jun;202(18):4329–36.

68. Sova A, Pervushin D, Smurov I. Development of multimaterial coatings by cold spray and gas detonation spraying. Surf Coatings Technol. 2010 Nov;205(4):1108–14.

69. Dell'Edera M, Lo Porto C, De Pasquale I, Petronella F, Curri ML, Agostiano A, et al. Photocatalytic TiO2-based coatings for environmental applications. Catal Today. 2021;380(April):62–83.

70. Obregón S, Rodríguez-González V. Photocatalytic TiO2 thin films and coatings prepared by sol–gel processing: a brief review. J Sol-Gel Sci Technol. 2022;102(1):125–41.

71. Ayalew AA, Han X, Sakairi M. a critical review of additive material manufacturing through electrochemical deposition techniques. Addit Manuf. 2023 Sep;77(April):103796.

72. Li C, Iqbal M, Lin J, Luo X, Jiang B, Malgras V, et al. Electrochemical Deposition: an Advanced Approach for Templated Synthesis of Nanoporous Metal Architectures. Acc Chem Res. 2018;51(8):1764–73.

73. Lin J, Kilani M, Baharfar M, Wang R, Mao G. Understanding the nanoscale phenomena of nucleation and crystal growth in electrodeposition. Nanoscale. 2024;16(42):19564–88.

74. Salim NT, Yamada M, Nakano H, Fukumoto M. The synthesis of titanium dioxide (TiO2) powder for cold spray process. IOP Conf Ser Mater Sci Eng. 2011;18(SYMPOSIUM 2A).

75. Hassaan MA, El-Nemr MA, Elkatory MR, Ragab S, Niculescu V-C, El Nemr A. Principles of Photocatalysts and Their Different Applications: a Review. Top Curr Chem. 2023 Dec 31;381(6):31.

76. Winnicki M. Advanced Functional Metal-Ceramic and Ceramic Coatings. Coatings. 2021;11(i):1044.

77. Akedo J. Room temperature impact consolidation and application to ceramic coatings: aerosol deposition method. J Ceram Soc Japan. 2020 Mar 1;128(3):101–16.

78. Seremak W, Jasiorski M, Baszczuk A, Winnicki M. Preliminary Study on Low-Pressure Cold Spray Process Parameters: Effect on Mechanical and Photocatalytic Properties of TiO2 Coatings. J Therm Spray Technol. 2023 Oct 15;32(7):1926–39.

79. Hanft D, Exner J, Schubert M, Stöcker T, Fuierer P, Moos R. an overview of the Aerosol Deposition method: Process fundamentals and new trends in materials applications. J Ceram Sci Technol. 2015;6(3):147–81.

80. Viscusi A, Astarita A, Gatta R Della, Rubino F. a perspective review on the bonding mechanisms in cold gas dynamic spray. Surf Eng. 2019 Sep 1;35(9):743–71.

81. Daneshian B, Gaertner F, Assadi H, Hoeche D, Weber W, Klassen T. Size Effects of Brittle Particles in Aerosol Deposition—Molecular Dynamics Simulation. J Therm Spray Technol. 2021;30(3):503–22.

82. Guo D, Kazasidis M, Hawkins A, Fan N, Leclerc Z, MacDonald D, et al. Cold Spray: Over 30 Years of Development Toward a Hot Future. J Therm Spray Technol. 2022;31(4):866–907.

83. Villafuerte J, editor. Modern Cold Spray. Modern Cold Spray. Cham: Springer International Publishing; 2015.

84. Moridi A, Hassani-Gangaraj SM, Guagliano M, Dao M. Cold spray coating: Review of material systems and future perspectives. Surf Eng. 2014;30(6):369–95.

85. Assadi H, Kreye H, Gärtner F, Klassen T. Cold spraying – a materials perspective. Acta Mater. 2016 Sep;116:382–407.

86. Özdemir OÇ. Process parameters and control. In: Victor K. Champagne, Dennis Helfritch MHG, editor. Advances in Cold Spray. Elsevier; 2023. p. 89–134.

87. Pattison J, Celotto S, Khan A, O'Neill W. Standoff distance and bow shock phenomena in the Cold Spray process. Surf Coatings Technol. 2008;202(8):1443–54.

88. Adaan-Nyiak MA, Tiamiyu AA. Recent advances on bonding mechanism in cold spray process: a review of single-particle impact methods. J Mater Res. 2023 Jan 14;38(1):69–95.

89. Grujicic M. Particle/substrate interaction in the cold-spray bonding process. In: the Cold Spray Materials Deposition Process. Elsevier; 2007. p. 148–77.

90. Hussain T, McCartney DG, Shipway PH, Zhang D. Bonding mechanisms in cold spraying: the contributions of metallurgical and mechanical components. J Therm Spray Technol. 2009;18(3):364–79.

91. Papyrin A, Kosarev V, Klinkov S, Alkimov A, Fomin V. Current status of the cold spray process. In: Cold Spray Technology. Elsevier; 2007. p. 248–323.

92. Shinoda K, Gaertner F, Lee C, Dolatabadi A, Johnson S. Kinetic Spraying of Brittle Materials: From Layer Formation to Applications in Aerosol Deposition and Cold Gas Spraying. J Therm Spray Technol. 2021 Feb 14;30(3):471–9.

93. Klinkov SV, Kosarev VF, Rein M. Cold spray deposition: Significance of particle impact phenomena. Aerosp Sci Technol. 2005 Oct;9(7):582–91.

94. Assadi H, Gärtner F, Stoltenhoff T, Kreye H. Bonding mechanism in cold gas spraying. Acta Mater. 2003 Sep;51(15):4379–94.

95. Schmidt T, Assadi H, Gärtner F, Richter H, Stoltenhoff T, Kreye H, et al. From Particle Acceleration to Impact and Bonding in Cold Spraying. J Therm Spray Technol. 2009 Dec 6;18(5–6):794.

96. Grujicic M, Saylor JR, Beasley DE, DeRosset WS, Helfritch D. Computational analysis of the interfacial bonding between feed-powder particles and the substrate in the cold-gas dynamic-spray process. Appl Surf Sci. 2003;219(3–4):211–27.

97. Alkhimov AP, Klinkov S V., Kosarev VF. Experimental study of deformation and attachement of microparticles to an obstacle upon high-rate impact. J Appl Mech Tech Phys. 1999;40(6):1126–32.

98. Akedo J. Room Temperature Impact Consolidation (RTIC) of Fine Ceramic Powder by Aerosol Deposition Method and Applications to Microdevices. J Therm Spray Technol. 2008 Jun 18;17(2):181–98.

99. Yamada M, Isago H, Nakano H, Fukumoto M. Cold spraying of TiO 2 photocatalyst coating with nitrogen process gas. J Therm Spray Technol. 2010;19(6):1218–23.

100. Schmidt K, Buhl S, Davoudi N, Godard C, Merz R, Raid I, et al. Ti surface modification by cold spraying with TiO 2 microparticles. Surf Coatings Technol. 2017 Jan;309:749–58.

101. Kliemann JO, Gutzmann H, Gärtner F, Hübner H, Borchers C, Klassen T. Formation of cold-sprayed ceramic titanium dioxide layers on metal surfaces. J Therm Spray Technol. 2011;20(1–2):292–8.

102. Winnicki M, Łatka L, Jasiorski M, Baszczuk A. Mechanical properties of TiO2 coatings deposited by low pressure cold spraying. Surf Coatings Technol. 2020;126516.

103. Gardon M, Fernández-Rodríguez C, Garzón Sousa D, Doña-Rodríguez JM, Dosta S, Cano IG, et al. Photocatalytic Activity of Nanostructured Anatase Coatings Obtained by Cold Gas Spray. J Therm Spray Technol. 2014 Oct 14;23(7):1135–41.

104. Omar N irinah, Yamada M, Yasui T, Fukumoto M. Bonding Mechanism of Cold-Sprayed TiO2 Coatings on Copper and Aluminum Substrates. Coatings. 2021;11(11):1349.

105. Ichikawa Y, Shinoda K. Current Status and Challenges for Unified Understanding of Bonding Mechanism in Solid Particle Deposition Process. Mater Trans. 2021 Jun 1;62(6):691–702.

106. M.Winnicki, L. Łatka, M. Jasiorski et al. Mechanical properties ofTiO2 coatings deposited by low pressure cold spraying. Surf Coat Technol. 2018;

107. Koivuluoto H, Coleman A, Murray K, Kearns M, Vuoristo P. High Pressure Cold Sprayed (HPCS) and Low Pressure Cold Sprayed (LPCS) Coatings Prepared from OFHC Cu Feedstock: Overview from Powder Characteristics to Coating Properties. J Therm Spray Technol. 2012 Sep 9;21(5):1065–75.

108. Yin S, Cavaliere P, Aldwell B, Jenkins R, Liao H, Li W, et al. Cold spray additive manufacturing and repair: Fundamentals and applications. Addit Manuf. 2018 May;21(August 2017):628–50.

109. Winnicki M, Piwowarczyk T, Małachowska A, Ambroziak A. Effect of gas pressure and temperature on stereometric properties of Al+Al2O3 composite coatings deposited by LPCS method. Arch Metall Mater. 2014;59(3):879–86.

110. Alonso L, Garrido-Maneiro MA, Poza P. a study of the parameters affecting the particle velocity in cold-spray: Theoretical results and comparison with experimental data. Addit Manuf. 2023;67(March):103479.

111. Chun D-M, Choi J-O, Lee CS, Ahn S-H. Effect of stand-off distance for cold gas spraying of fine ceramic particles (<5μm) under low vacuum and room temperature using nano-particle deposition system (NPDS). Surf Coatings Technol. 2012 Jan;206(8–9):2125–32.

112. Goyal T, Walia RS, Sidhu TS. Surface roughness optimization of cold-sprayed coatings using Taguchi method. Int J Adv Manuf Technol. 2012;60(5–8):611–23.

113. Singh S, Raman RKS, Berndt CC, Singh H. Influence of cold spray parameters on bonding mechanisms: a review. Metals (Basel). 2021;11(12).

114. Seraj RA, Abdollah-zadeh A, Dosta S, Canales H, Assadi H, Cano IG. The effect of traverse speed on deposition efficiency of cold sprayed Stellite 21. Surf Coatings Technol. 2019;366(March):24–34.

115. Cai Z, Deng S, Liao H, Zeng C, Montavon G. The effect of spray distance and scanning step on the coating thickness uniformity in cold spray process. J Therm Spray Technol. 2014;23(3):354–62.

116. Lima RS, Kucuk A, Berndt CC, Karthikeyan J, Kay CM, Lindemann J. Deposition efficiency, mechanical properties and coating roughness in cold-sprayed titanium. J Mater Sci Lett. 2002;21(21):1687–9.

117. Moridi A, Hassani Gangaraj SM, Vezzu S, Guagliano M. Number of passes and thickness effect on mechanical characteristics of cold spray coating. Procedia Eng. 2014;74:449–59.

118. Raoelison RN, Xie Y, Sapanathan T, Planche MP, Kromer R, Costil S, et al. Cold gas dynamic spray technology: a comprehensive review of processing conditions for various technological developments till to date. Addit Manuf. 2018 Jan;19:134–59.

119. Brodmann F. Cold spray process parameters. In: the Cold Spray Materials Deposition Process. CRC Press; 2007. p. 105–16.

120. Salim NT, Yamada M, Nakano H, Shima K, Isago H, Fukumoto M. The effect of post-treatments on the powder morphology of titanium dioxide (TiO2) powders synthesized for cold spray. Surf Coatings Technol. 2011;206(2–3):366–71.

121. Toibah AR, Sato M, Yamada M, Fukumoto M. Cold-Sprayed TiO 2 Coatings from Nanostructured Ceramic Agglomerated Powders. Mater Manuf Process. 2016 Aug 17;31(11):1527–34.

122. Winnicki M, Baszczuk A, Jasiorski M, Borak B, Małachowska A. Preliminary studies of TiO2 nanopowder deposition onto metallic substrate by low pressure cold spraying. Surf Coatings Technol. 2019;371:194–202.

123. Gao F, Yang Y, Wang T. Preparation of porous TiO2/Ag heterostructure films with enhanced photocatalytic activity. Chem Eng J. 2015;270:418–27.

124. Liu J, Liu Y, Suo X, Latka L, Małachowski A, Lu D, et al. Cold Spray Construction of Nanostructured Titania Coatings for Photocatalytic Applications. J Therm Spray Technol. 2021;30(4):918–25.

125. Sova A, Papyrin A, Smurov I. Influence of ceramic powder size on process of cermet coating formation by cold spray. J Therm Spray Technol. 2009;18(4):633–41.

126. Borlaf M, Moreno R. Colloidal sol-gel: a powerful low-temperature aqueous synthesis route of nanosized powders and suspensions. Open Ceram. 2021;8(November):100200.

127. Danks AE, Hall SR, Schnepp Z. The evolution of "sol-gel" chemistry as a technique for materials synthesis. Mater Horizons. 2016;3(2):91–112.

128. Ullattil SG, Periyat P. Sol-Gel Synthesis of Titanium Dioxide Chapter 9 Sol-Gel Synthesis of Titanium Dioxide. In: Sol-Gel Materials for Energy, Environment and Electronic Applications. Springer International Publishing; 2017.

129. Niederberger M, Pinna N. Metal Oxide Nanoparticles in Organic Solvents. Antarctic nutrient

cycles and food webs. London: Springer London; 2009. 466–472 p. (Engineering Materials and Processes).

130. Yazid SA, Rosli ZM, Juoi JM. Effect of titanium (IV) isopropoxide molarity on the crystallinity and photocatalytic activity of titanium dioxide thin film deposited via green sol-gel route. J Mater Res Technol. 2019;8(1):1434–9.

131. Brinker CJ, Scherer GW. Sol-Gel Science. Sol-Gel Science: the Physics and Chemistry of Sol-Gel Processing. Elsevier; 1990. 1–908 p.

132. Cushing BL, Kolesnichenko VL, O'Connor CJ. Recent Advances in the Liquid-Phase Syntheses of Inorganic Nanoparticles. Chem Rev. 2004 Sep 1;104(9):3893–946.

133. Livage J, Henry M, Sanchez C. Sol-gel chemistry of transition metal oxides. Prog Solid State Chem. 1988;18(4):259–341.

134. Sakka S. Handbook of sol-gel science and technology: processing, characterization, and applications. Vol. 42, Choice Reviews Online. 2005. 42-5885-42–5885 p.

135. Bischoff BL, Anderson MA. Peptization Process in the Sol-Gel Preparation of Porous Anatase (TiO2). Chem Mater. 1995;7(10):1772–8.

136. Paenurk E, Kaupmees K, Himmel D, Kütt A, Kaljurand I, Koppel IA, et al. a unified view to Brønsted acidity scales: Do we need solvated protons? Chem Sci. 2017;8(10):6964–73.

137. Hu L, Yoko T, Kozuka H, Sakka S. Effects of solvent on properties of sol-gel-derived TiO2 coating films. Thin Solid Films. 1992;219(1–2):18–23.

138. Golobostanfard MR, Abdizadeh H. Effect of mixed solvent on structural, morphological, and optoelectrical properties of spin-coated TiO 2 thin films. Ceram Int. 2012;38(7):5843–51.

139. Lee SE, Heo SY, Go HE, Lee JS, Kwon OH, Hong CK, et al. Effects of alcohol solvents on formation of the hydrated silica gel. J Ceram Process Res. 2018;19(4):321–6.

140. Chang CC, Hong SY, Cheng LP, Yu YY. TiO2 nanoparticles synthesized in an aprotic solvent and applied to prepare high-refractive-index TiO2-polyimide hybrid thin films. J Sol-Gel Sci Technol. 2014;71(1):129–35.

141. Shen ZY, Li LY, Li Y, Wang CC. Fabrication of hydroxyl group modified monodispersed hybrid silica particles and the h-SiO2/TiO2 core/shell microspheres as high performance photocatalyst for dye degradation. J Colloid Interface Sci. 2011;354(1):196–201.

142. Chang C, Rad S, Gan L, Li Z, Dai J, Shahab A. Review of the sol–gel method in preparing nano TiO2 for advanced oxidation process. Nanotechnol Rev. 2023;12(1).

143. Lukong VT, Ukoba KO, Jen TC. Analysis of sol aging effects on self-cleaning properties of TiO2thin film. Mater Res Express. 2021;8(10).

144. ISO 10678:2010(E). Fine ceramics (advanced ceramics, advanced technical ceramics) — Determination of photocatalytic activity of surfaces in an aqueous medium by degradation of methylene blue. International Organization for Standardization. 2010.

145. (2024.03.21) International Organization for Standardization (ISO) [Internet]. Available from: https://www.iso.org/home.html

146. Mills A, Hill C, Robertson PKJ. Overview of the current ISO tests for photocatalytic materials. J Photochem Photobiol a Chem. 2012;237:7–23.

147. Mowry S, Ogren PJ. Kinetics of Methylene Blue Reduction by Ascorbic Acid. J Chem Educ. 1999;76(7):970–4.

148. Tschirch J, Dillert R, Bahnemann D. Photocatalytic degradation of methylene blue on fixed powder layers: Which limitations are to be considered? J Adv Oxid Technol. 2008;11(2):193–8.

149. Mills A. an overview of the methylene blue ISO test for assessing the activities of photocatalytic films. Appl Catal B Environ. 2012;128:144–9.

150. Kaur K, Singh CV. Amorphous TiO2 as a Photocatalyst for Hydrogen Production: a DFT Study of Structural and Electronic Properties. In: Energy Procedia. 2012. p. 291–9.

151. Mills A, Wang J. Photobleaching of methylene blue sensitised by TiO2: an ambiguous system? J Photochem Photobiol a Chem. 1999;127(1–3):123–34.

152. McIntyre HM, Hart ML. Photocatalytic porous silica-based granular media for organic pollutant degradation in industrial waste-streams. Catalysts. 2021;11(2):1–20.

153. Mills A, Hill C, Robertson PKJ. Overview of the current ISO tests for photocatalytic materials. Vol. 237, Journal of Photochemistry and Photobiology A: Chemistry. 2012. p. 7–23.

154. Murzin DY. Heterogeneous photocatalytic kinetics: Beyond the adsorption/desorption equilibrium concept. React Kinet Catal Lett. 2006;89(2):277–84.

155. Tran HD, Nguyen DQ, Do PT, Tran UNP. Kinetics of photocatalytic degradation of organic compounds: a mini-review and new approach. RSC Adv. 2023;13(25):16915–25.

156. Zhang L, Jaroniec M. Fundamentals of adsorption for photocatalysis. Interface Sci Technol. 2020;31:39–62.

157. Sorathiya K, Mishra B, Kalarikkal A, Reddy KP, Gopinath CS, Khushalani D. Enhancement in Rate of Photocatalysis Upon Catalyst Recycling. Sci Rep. 2016;6(June):1–9.

158. Lei P, Wang F, Gao X, Ding Y, Zhang S, Zhao J, et al. Immobilization of TiO 2 nanoparticles in polymeric substrates by chemical bonding for multi-cycle photodegradation of organic pollutants. J Hazard Mater. 2012;227–228:185–94.

159. Nawawi WI, Ain SK, Zaharudin R, Sahid S. Multi-Cycle Photodegradation of Anionic and Cationic Dyes by New TiO_2/DSAT Immobilization System. Appl Mech Mater. 2016 May;835:353–8.

160. Kaewgun S, Lee BI. Deactivation and regeneration of visible light active brookite titania in photocatalytic degradation of organic dye. J Photochem Photobiol a Chem. 2010;210(2–3):162–7.

161. Zhang Y, Yip KL, Kim Y, Chouinard C, Licato J, Kim J-H. Monolithic Ceramic CoTiO 3 /TiO 2 Membrane Balancing Catalytic Efficiency and Durability in Advanced Oxidation Processes. Environ Sci Technol. 2025 Mar 28;

162. Olabarrieta J, Zorita S, Peña I, Rioja N, Monzón O, Benguria P, et al. Aging of photocatalytic coatings under a water flow: Long run performance and TiO 2 nanoparticles release. Appl Catal B Environ. 2012;123–124:182–92.

163. Paul D, Devaprakasam D. a novel approach to enhance performance, stability and longevity of the solar cells by mitigating UV-induced degradation with monolayer – Boosted nano-TiO2 coatings. Sol Energy. 2025 Jan;285(November 2024):113118.

164. D'Agata A, Fasulo S, Dallas LJ, Fisher AS, Maisano M, Readman JW, et al. Enhanced toxicity of "bulk" titanium dioxide compared to "fresh" and "aged" nano-TiO2 in marine mussels (Mytilus galloprovincialis). Nanotoxicology. 2014;8(5):549–58.

165. Štengl V, Bakardjieva S, Murafa N, Šubrt J, Měšťánková H, Jirkovský J. Preparation, characterization and photocatalytic activity of optically transparent titanium dioxide particles. Mater Chem Phys. 2007;105(1):38–46.

166. Guo R, Bao Y, Kang Q, Liu C, Zhang W, Zhu Q. Solvent-controlled synthesis and photocatalytic activity of hollow TiO2 microspheres prepared by the solvothermal method. Colloids Surfaces a Physicochem Eng Asp. 2022;633(P1):127931.

167. Agafonov a V., Redozubov AA, Kozik V V., Kraev AS. Photocatalytic activity of titania nanopowders prepared by a sol-gel process at various pHs. Russ J Inorg Chem. 2015;60(8):906–12.

168. Li W, Assadi H, Gaertner F, Yin S. a Review of Advanced Composite and Nanostructured Coatings by Solid-State Cold Spraying Process. Crit Rev Solid State Mater Sci. 2019;44(2):109–56.

169. Rowe MC, Brewer BJ. AMORPH: a statistical program for characterizing amorphous materials by X-ray diffraction. Comput Geosci. 2018;120(July):21–31.

170. ASTM C633-13(2021). Standard Test Method for Adhesion or Cohesion Strength of Thermal Spray Coatings. ASTM International. 2021.

171. ISO 14916:2017. Thermal spraying — Determination of tensile adhesive strength. International Organization for Standardization. 2017.

172. PN-EN 1071-3. Techniczna ceramika zaawansowana -- Metody badania powłok ceramicznych -- Część 3: Oznaczanie adhezji i innych mechanicznych rodzajów uszkodzeń w próbie zarysowania. Polski Komitet Normalizacyjny. 2005.

173. Tang W, Hu CC, Tsao CC, Chen CS, Roselin LS, Kuo CG, et al. Photocatalytic Activity and Mechanical Performance of O and N Co-doped TiO2 Thin Films. J Electron Mater. 2022;51(11):6145–59.

174. Schipporeit S, Mergel D. Spectral decomposition of Raman spectra of mixed-phase TiO2 thin films on Si and silicate substrates. J Raman Spectrosc. 2018;49(7):1217–29.

175. Behera AK, Mantry S, Roy S, Pati S. Improving bond strength and deposition efficiency of ceramic coatings via low pressure cold spraying: a study on hydroxyapatite coatings with Cu-Zn blends. Surf Coatings Technol. 2024;494(September).

176. Nazeer MA, Yilgor E, Yagci MB, Unal U, Yilgor I. Effect of reaction solvent on hydroxyapatite synthesis in sol–gel process. R Soc Open Sci. 2017 Dec 20;4(12):171098.

177. Angel J Del, Aguilera AF, Galindo IR, Martínez M, Viveros T. Synthesis and Characterization of Alumina-Zirconia Powders Obtained by Sol-Gel Method: Effect of Solvent and Water Addition Rate. Mater Sci Appl. 2012;03(09):650–7.

178. (2024.03.17) Solvent Miscibility Table [Internet]. Ohio State University. Available from: https://research.cbc.osu.edu/turro.1/wp-content/uploads/2017/02/solvent.miscibility.pdf

179. Ruths M. Surface Forces, Surface Tension, and Adhesion. Wang QJ, and Chung Y-W, editors.

Encyclopedia of Tribology. Springer US; 2013. 3435–3443 p.

180. Seremak W, Baszczuk A, Jasiorski M, Gibas A, Winnicki M. Photocatalytic Activity Enhancement of Low-pressure Cold-Sprayed TiO2 Coatings Induced by Long-term Water Vapor Exposure. J Therm Spray Technol. 2021;

181. Seremak W, Jasiorski M, Baszczuk A, Winnicki M. Durability assessment of low-pressure cold-sprayed TiO2 photocatalytic coatings: Photocatalytic and mechanical stability. Surf Coatings Technol. 2025;497(October 2024):131740.

182. Burlacov I, Jirkovský J, Kavan L, Ballhorn R, Heimann RB. Cold gas dynamic spraying (CGDS) of TiO2 (anatase) powders onto poly(sulfone) substrates: Microstructural characterisation and photocatalytic efficiency. J Photochem Photobiol a Chem. 2007 Apr;187(2–3):285–92.

183. Toma FL, Sokolov D, Bertrand G, Klein D, Coddet C, Meunier C. Comparison of the photocatalytic behavior of TiO2 coatings elaborated by different thermal spraying processes. Proc Int Therm Spray Conf. 2006;15(December):576–81.

184. Zhang H, Xia W, Wang G, Yang Y, Zou Y. an integrated investigation approach for coating temperature measurement and control during plasma spraying. J Therm Spray Technol. 2008;17(2):263–74.

185. Kim H, Kim J, Lee JK. Enhancement of the Surface Roughness by Powder Spray Coating on Zirconia Substrate. 2019;19(10):6285–90.

186. Trifa FI, Montavon G, Coddet C. Model-based expert system for design and simulation of APS coatings. J Therm Spray Technol. 2007;16(1):128–39.

187. Pawlowski L. The Science and Engineering of Thermal Spray Coatings: Second Edition. The Science and Engineering of Thermal Spray Coatings: Second Edition. 2008. 1–626 p.

188. Bull SJ. Failure mode maps in the thin film scratch adhesion test. Tribol Int. 1997;30(7):491–8.

189. Poirier D, Legoux J, Drew RAL, Gauvin R. Consolidation of Al 2 O 3 / Al Nanocomposite Powder by Cold Spray. 2011;20(January):275–84.

190. Chen H, Lee SW, Hur BY. Influence of Deposition Parameters on Adhesion/Cohesion of Plasma Sprayed TiO_2 Coatings. Mater Sci Forum. 2006;510–511:62–5.

191. Zawischa M, Makowski S, Kuczyk M, Weihnacht V. Surface & Coatings Technology Comparison of fracture properties of different amorphous carbon coatings using the scratch test and indentation failure method. Surf Coat Technol. 2022;435(February):128247.

192. Lee H, Shin H, Ko K. Effects of gas pressure of cold spray on the formation of Al-based intermetallic compound. J Therm Spray Technol. 2010;19(1–2):102–9.

193. Hajipour H, Abdollah-zadeh A, Assadi H, Taheri-Nassaj E, Jahed H. Effect of Feedstock Powder Morphology on Cold-Sprayed Titanium Dioxide Coatings. J Therm Spray Technol. 2018 Dec 2;27(8):1542–50.

194. Wang X, Zhang D, Xiang Q, Zhong Z, Liao Y. Review of Water-Assisted Crystallization for TiO2 Nanotubes. Vol. 10, Nano-Micro Letters. 2018.

195. Rao BM, Roy SC. Water assisted crystallization, gas sensing and photo-electrochemical properties of electrochemically synthesized TiO2 nanotube arrays. RSC Adv. 2014;4(90):49108–14.

196. Hossain MK, Akhtar US, Koirala AR, Hwang IC, Yoon KB. Steam-assisted synthesis of uniformly mesoporous anatase and its remarkably superior photocatalytic activities. Catal Today. 2015;243(C):228–34.

197. Li N, Zhang Q, Joo JB, Lu Z, Dahl M, Gan Y, et al. Water-assisted crystallization of mesoporous anatase TiO2 nanospheres. Nanoscale. 2016;8(17):9113–7.

198. Mangum JS, Agirseven O, Haggerty JES, Perkins JD, Schelhas LT, Kitchaev DA, et al. Selective brookite polymorph formation related to the amorphous precursor state in TiO2 thin films. J Non Cryst Solids. 2019;505(October 2018):109–14.

199. Komaraiah D, Radha E, Sivakumar J, Ramana Reddy MV, Sayanna R. Structural, optical properties and photocatalytic activity of Fe3+ doped TiO2 thin films deposited by sol-gel spin coating. Surfaces and Interfaces. 2019;17(April):100368.

200. Ghali E. Aluminum and Aluminum Alloys. In: Uhlig's Corrosion Handbook. Wiley; 2011. p. 715–45.

201. Zhu Y, Zhang L, Wang L, Fu Y, Cao L. The preparation and chemical structure of TiO2 film photocatalysts supported on stainless steel substrates via the sol-gel method. J Mater Chem. 2001;11(7):1864–8.

202. Pan JH, Lei Z, Lee WI, Xiong Z, Wang Q, Zhao XS. Mesoporous TiO 2 photocatalytic films on stainless steel for water decontamination. Catal Sci Technol. 2012;2(1):147–55.

203. Duque-Redondo E, Yamada K, Masoero E, Bañuelos Prieto J, Manzano H. Adsorption and migration of Cs and Na ions in geopolymers and zeolites. Mater Today Commun. 2023;36(June).

204. Pan H, Gu B, Zhang Z. Phase-Dependent Photocatalytic Ability of TiO 2 : a First-Principles Study. 2009;3074–8.

205. Ho SJ, Yeh CW, Kumar RV, Chen HS. Self-organized sol-gel TiO2 structures: Particles, rectangle tubes, and flower-like slabs. Mater Des. 2017;115:332–8.

206. Hu W, Li L, Li G, Liu Y, Withers RL. Atomic-scale control of TiO6 octahedra through solution chemistry towards giant dielectric response. Sci Rep. 2014;4:1–9.

207. Von Fraunhofer JA. Adhesion and cohesion. Int J Dent. 2012;2012.

208. Abbas M, Smith GM, Munroe PR. Microstructural investigation of bonding and melting-induced rebound of HVOF sprayed Ni particles on an aluminum substrate. Surf Coatings Technol. 2020;402(July):126353.

209. Drehmann R, Grund T, Lampke T, Wielage B, Manygoats K, Schucknecht T, et al. Interface Characterization and Bonding Mechanisms of Cold Gas-Sprayed Al Coatings on Ceramic Substrates. J Therm Spray Technol. 2014;24(1–2):92–9.

210. Wicks Jr. ZW, Jones FNS, Pappas P, Wicks DA. Adhesion. In: Organic Coatings: Science and Technology. 3rd editio. John Wiley & Sons, Inc; 2007. p. 121–36.

211. Pletincx S, Fockaert LLI, Mol JMC, Hauffman T, Terryn H. Probing the formation and degradation of chemical interactions from model molecule/metal oxide to buried polymer/metal oxide interfaces. npj Mater Degrad. 2019;3(1):1–12.

212. Metroke TL, Parkhill RL, Knobbe ET. Passivation of metal alloys using sol-gel-derived materials - a review. Prog Org Coatings. 2001;41(4):233–8.

213. Guin AK, Nayak SK, Rout TK, Bandyopadhyay N, Sengupta DK. Corrosion behavior of nanohybrid titania-silica composite coating on phosphated steel sheet. J Coatings Technol Res. 2012;9(1):97–106.

214. Niu S, Liu Z, Luo Y, Li X, Zhou T, Si Y, et al. Reinforcement of silica-based ceramic cores based on amorphous and polycrystalline mullite fibers. Ceram Int. 2023;49(19):31378–84.

215. Raoelison RN. Cold spray technology: a perspective of nature-inspired feature processing and biomanufacturing by a heatless additive method using nanopowders. Adv Addit Manuf Artif Intell Nature-Inspired, Biomanufacturing. 2022;129–40.

216. Weldon DG. Why Coatings Work and Why They Fail. Fail Anal Paint Coatings, Revis Ed. 2009;9–37.

217. Runge JM, Weritz J. Metallurgy Basics for Aluminum Surface Treatment. Aluminum Science and Technology. 2018. 555–567 p.

218. Sclafani A, Herrmann JM. Comparison of the photoelectronic and photocatalytic activities of various anatase and rutile forms of titania in pure liquid organic phases and in aqueous solutions. J Phys Chem. 1996;100(32):13655–61.

219. Matějová L, Kočí K, Troppová I, Šihor M, Edelmannová M, Lang J, et al. TiO 2 and Nitrogen Doped TiO 2 Prepared by Different Methods; on the (Micro)structure and Photocatalytic Activity in CO 2 Reduction and N 2 O Decomposition. J Nanosci Nanotechnol. 2017;18(1):688–98.

220. Yoon DH, Biswas MRUD, Sakthisabarimoorthi A. Impact of crystalline core/amorphous shell structured black TiO2 nanoparticles on photoelectrochemical water splitting. Opt Mater (Amst). 2022;133(September):113030.

221. Schneider J, Matsuoka M, Takeuchi M, Zhang J, Horiuchi Y, Anpo M, et al. Understanding TiO2 Photocatalysis: Mechanisms and Materials. Chem Rev. 2014;114(19):9919–9986.

222. Li Q, Jiang L, Li Y, Wang X, Zhao L, Huang P, et al. Enhancement of Visible-Light Photocatalytic Degradation of Tetracycline by Co-Doped TiO2 Templated by Waste Tobacco Stem Silk. Molecules. 2023;28(1).

223. Jafari S, Sillanpää M. Adsorption of dyes onto modified titanium dioxide. Advanced Water Treatment: Adsorption. Elsevier Inc.; 2020. 85–160 p.

224. Luís AM, Neves MC, Mendonça MH, Monteiro OC. Influence of calcination parameters on the TiO2 photocatalytic properties. Mater Chem Phys. 2011;125(1–2):20–5.

225. Torralvo MJ, Sanz J, Sobrados I, Soria J, Garlisi C, Palmisano G, et al. Anatase photocatalyst with supported low crystalline TiO2: the influence of amorphous phase on the activity. Appl Catal B Environ. 2018;221(September 2017):140–51.

226. Nguyen-Le M-T, Lee B-K. High temperature synthesis of interfacial functionalized carboxylate mesoporous TiO2 for effective adsorption of cationic dyes. Chem Eng J. 2015 Dec;281:20–33.

227. Yan X, Li J, Ma C, Tang Y, Kong X, Lu J. Study on the lifetime of photocatalyst by photocatalytic membrane reactors (PMR). Water Sci Technol. 2020;81(1):131–7.

228. Pelaez M, de la Cruz AA, O'Shea K, Falaras P, Dionysiou DD. Effects of water parameters on the degradation of microcystin-LR under visible light-activated TiO2 photocatalyst. Water Res.

2011;45(12):3787–96.

229. Lair A, Ferronato C, Chovelon JM, Herrmann JM. Naphthalene degradation in water by heterogeneous photocatalysis: an investigation of the influence of inorganic anions. J Photochem Photobiol a Chem. 2008;193(2–3):193–203.

230. Solonenko OP, Ando Y, Nishiyama H, Kindole D, Smirnov a V., Golovin AA, et al. Synthesis of thick photocatalytic titania surface layers by solution plasma spraying and subsequent treatment by pulsed laminar plasma jet. Surf Coatings Technol. 2018;333(October 2017):39–51.

231. Allen NS, Mahdjoub N, Vishnyakov V, Kelly PJ, Kriek RJ. The effect of crystalline phase (anatase, brookite and rutile) and size on the photocatalytic activity of calcined polymorphic titanium dioxide (TiO2). Polym Degrad Stab. 2018;150(January):31–6.

232. Forero-Sossa PA, Giraldo-Betancur AL, Poblano-Salas CA, Gutierrez-Pérez AI, Rodríguez-Vigueras EM, Corona-Castuera J, et al. Nozzle Geometry and Particle Size Influence on the Behavior of Low Pressure Cold Sprayed Hydroxyapatite Particles. Coatings. 2022 Nov 29;12(12):1845.

233. Vilardell AM, Cinca N, Cano IG, Concustell A, Dosta S, Guilemany JM, et al. Dense nanostructured calcium phosphate coating on titanium by cold spray. J Eur Ceram Soc. 2017;37(4):1747–55.

234. Prasai B, Cai B, Underwood MK, Lewis JP, Drabold DA. Properties of amorphous and crystalline titanium dioxide from first principles. J Mater Sci. 2012;47(21):7515–21.

235. Kumar A, Singh H, Kant R. Influence of Substrate Roughness and Ceramic Content on Deposition Characteristics of Cold-Sprayed Ti/TiO2 Deposits. Met Mater Int. 2023;29(6):1669–83.

236. Vinay G, Halder S, Kant R, Singh H. Examining the contribution of tamping effect on inter-splat bonding during cold spray. Mater Sci Eng A. 2024;893(January):146112.

237. Bokade R, Müftü S, Özdemir OÇ, Jin X. Thermal imaging based non-destructive testing for fault detection in cold spray additive manufacturing. 2025;134(December 2024):1057–68.

238. Tryba B, Tygielska M, Wróbel R, Żołnierkiewicz G, Guskos N. Influence of pH of sol-gel solution on phase composition and photocatalytic activity of TiO2 under UV and visible light. Mater Res Bull. 2016;

239. Azeez F, Al-hetlani E, Arafa M, Abdelmonem Y, Nazeer AA, Amin MO, et al. The effect of surface charge on photocatalytic degradation of methylene blue dye using chargeable titania nanoparticles. 2018;(April):1–9.

240. Caruso R, Sanctis O de, Macías-García A, Benavidez E, Mintzer SR. Influence of pH value and solvent utilized in the sol–gel synthesis on properties of derived ZrO2 powders. J Mater Process Technol. 2004 Oct;152(3):299–303.

241. Lin H, Huang CP, Li W, Ni C, Shah SI, Tseng YH. Size dependency of nanocrystalline TiO2 on its optical property and photocatalytic reactivity exemplified by 2-chlorophenol. Appl Catal B Environ. 2006;68(1–2):1–11.

242. Behnajady MA, Eskandarloo H, Modirshahla N, Shokri M. Investigation of the effect of sol–gel synthesis variables on structural and photocatalytic properties of TiO2 nanoparticles. Desalination. 2011 Sep;278(1–3):10–7.